Fermilab Library
0 1160 0020099 2

E-605

Inclusive Hadronic Production Cross Sections Measured in 400 GeV Proton-Nucleus Collisions

JAMES ARTHUR CRITTENDEN

Submitted in partial fulfillment of the
requirements for the degree
of Doctor of Philosophy
in the Graduate School of Arts and Sciences

COLUMBIA UNIVERSITY

1986

LIBOFFCE
FERMI
THESIS

FERMILAB
LIBRARY

ABSTRACT

Inclusive Hadronic Production Cross Sections

Measured in 400 GeV Proton-Nucleus Collisions

JAMES ARTHUR CRITTENDEN

This dissertation presents results on the production of hadrons in collisions of 400 GeV/c protons with beryllium, copper, and tungsten nuclei. The data cover the region from 5.2 to 8.0 GeV/c in the transverse momentum of the final state hadron and from 73° to 102° in the production angle θ^*. The restriction of the data to high x_T ($x_T = 2p_T/\sqrt{s}$) enriches the sample with events produced by hard collisions of valence quarks. Asymmetries about $\theta^* = 90°$ reflect the presence of neutrons in the target nuclei. Measurements of the atomic weight dependence parameter α as a function of production angle are also discussed.

Table of Contents

I. Introduction 1

II. Historical Background and Theoretical Context 3

III. Design Considerations in Experiment 605 13

IV. Technical Information on the Apparatus 17

V. Data Acquisition 25

VI. The Data Run 34

VII. The Data Analysis 36

VIII. The Results 51

Acknowledgements 59

Appendix 61

References 67

Table Captions 69

Figure Captions 78

AA58444

CHAPTER I

INTRODUCTION

IN WHICH the times, places, and personages relevant to experiment 605 are generally indicated, in hopes of making the Reader feel a little more at home in a morass of disconcerting detail.

The work described in this dissertation results from the collective effort of an international group of elementary particle physicists. It served the research goals of experiment 605 (E605), which was performed at the Fermi National Accelerator Laboratory (FNAL) in the Meson East beam line. Major contributions to the success of the experiment were made by FNAL, CEN-Saclay in France, CERN in Switzerland, KEK and Kyoto University in Japan, the University of Washington, Columbia University, and the State University of New York at Stony Brook. Roughly forty physicists joined efforts to build and operate the apparata necessary to obtain the physical measurements so eagerly awaited by all. Approval to perform the experiment was received from the FNAL directorate in 1979. The data presented here were recorded during the first running period (officially referred to as a 'test run'), which took place in June, 1982. Experiment 605

has since endured two more running periods, the first extending from January, 1984, until June, 1984, and the second from January, 1985, until September, 1985.

CHAPTER II

HISTORICAL BACKGROUND AND THEORETICAL CONTEXT

IN which the experimental and theoretical developments relevant to the study of hadron production in elementary particle physics from about 1970 to the present are described in general. Included as well is a more detailed description of the current interpretation of experimental results obtained from inelastic hadron-nucleon collisions.

The interpretation of particles emanating from the inelastic collisions of hadrons as products of the hard scattering of elementary constituents began to draw widespread attention in the late 1960's. (The term "hadron" is applied to all particles subject to the strong interactions.) Although evidence for the existence of small hard scattering centers within protons had been found in deeply inelastic electron-proton scattering;[1,2] there remained apparently contradictory evidence in data from hadron-hadron collisions. The principal problem defying a point-like constituent analysis was the strong dependence of hadron production on transverse momentum. Standard Rutherford

scattering, i.e. that of point charges, yields a cross section which is inversely proportional to the transverse momentum of the produced particle to the fourth power, while the observed cross section fell much more steeply. Nevertheless, based on general properties of the scaling of multiplicities with center-of-mass energy in hadronic interactions, Dr. Richard Feynman of the California Institute of Technology proposed a "parton" model of the proton[3].

In 1972 measurements from an experiment (referred to as CCR for CERN-Columbia-Rockefeller, the collaborating institutions) investigating proton-proton collisions at CERN[4] caused the prevalent interpretations of single hadron production to be reassessed. A topical model for inelastic hadron collisions at that time was a "fireball" model[5]. This model envisioned a sort of high energy hadronic plasma formed by the colliding hadrons, from which secondary hadrons "boiled off" with a Boltzmann distribution of energies. This exponential distribution fit data at lower transverse momenta fairly well, but was unambiguously refuted by the measurements of the CCR collaboration. These showed that at higher transverse momenta the inclusive production cross section for neutral π mesons dropped far less steeply, exceeding the exponential extrapolation by five orders of magnitude at a transverse momentum of four Gev/c. The controversies concerning high energy hadron collisions turned away from the existence of partons and toward the nature of these

partons.

Prime candidates for the role were the quarks postulated by Gell-Mann and Zweig in the early 1960's.[6,7] Originally proposed as the generators of an SU(3) group theory which served as a classification scheme for the multitude of particles discovered before 1963, the quark model had gained significance through its appealing simplicity. A mere triad of quark "flavors" accounted for the entire spectrum of observed particulate ground states and, in fact, predicted the existence of a particle with triple strangeness which was subsequently discovered and named the Ω baryon. (The "flavor" of a quark specifies a quantum number which is conserved in its strong interactions. Six flavors are necessary and sufficient to account for the currently observed spectrum of quark bound states. The oxymoronic terminology is intended to emphasize the arbitrary nature of the designation.) However, for almost a decade the credibility of the quark model suffered from a dearth of experimental justification. The lack of any observation of free quarks stimulated skepticism. The very definition of the word 'particle' had to be broadened to include objects which existed only in bound states. The inability to isolate individual quarks rendered useless all standard means of directly determining their quantum numbers. The successes of the static model were irrefutable; yet the lack of evidence for compositeness from hadron dynamics, i.e. their interactions with other particles, was dissatisfying. The deeply

inelastic electron-proton scattering results provided in part the required supporting evidence.

The discovery of the ψ meson in 1974 significantly enhanced the credibility of the quark model. The ψ was found to have a lifetime characteristic of electromagnetic decays, implying that its strong decays were suppressed. It followed that the ψ was composed of constituents carrying a new quantum number (now called "charm") which was conserved in strong interactions. The ψ was soon interpreted as the bound state of a charmed and an anti-charmed quark. The discovery of charm solved another topical theoretical paradox of the time, namely, the suppression of strangeness-changing neutral currents (for example, the extremely low branching ratio for the decay of neutral kaons to muon pairs). Indeed, the charmed quark had been postulated in an attempt to understand this otherwise unaccountable suppression. However, the inability of the electron-proton scattering and hadron collision experiments to specify quantum numbers such as the spin or charge of the partons precluded the identification of quarks with partons. The single hadron production cross section even at the higher transverse momenta fell far too steeply to allow its interpretation as the scattering of point-like particles.

One candidate for a parton was a bound state of two quarks. The Constituent Interchange Model proposed that the fundamental scattering occur between a single quark and a diquark bound state[8]. The attractiveness of this model was that it implied that the hadron production cross section vary inversely with the eighth power of the transverse momentum, as was observed. This model, however, also implied that in collisions of positive pions with protons, the production of positive pions at transverse momenta greater than two Gev/c would exceed the production of negative pions by a factor of at least three. This prediction was not borne out by subsequent experimental results[9]. Eventually theoretical prejudice became slanted in favor of a model involving the scattering of point-like particles.

The Model of Field, Feynman, and Fox

During the late 1970's a collaboration of efforts by Field, Feynman, and Fox at the California Institute of Technology led to a variety of successes in explaining the dependence of inclusive single hadron cross sections on transverse momentum and center-of-mass energy. The hypotheses of this model which survived experimental tests during several years of deliberation yielded the concept illustrated in figure 1. One fundamental constituent from each of the colliding hadrons participates in a hard

collision, the dynamics of the scattering given by a fundamental interaction $d\hat{\sigma}/d\hat{t}$. Afterwards, the scattered constituents independently combine with materialized energy quanta from the vacuum to form the final state hadrons. The disintegration of the colliding hadrons, the interaction of the fundamental constituents and the formation of the final state hadrons are all considered to occur independently.

$$E \frac{d^3\sigma}{dp^3}(AB \to C+X, s, p_t, \theta_{cm}) =$$

$$\int \frac{dx_a}{\pi} \int \frac{dx_b}{z_c} G_{A\to a}(x_a) G_{B\to b}(x_b) D_{c\to C}(z_c) \frac{d\hat{\sigma}}{d\hat{t}}(ab \to cd, \hat{s}, \hat{t}, \hat{u})$$

where
$$\hat{s} = x_a x_b s$$
$$\hat{t} = \frac{-1}{2} x_a s x_T \tan(\tfrac{1}{2}\theta_{cm})$$
$$\hat{u} = \frac{-1}{2} x_b s x_T \cot(\tfrac{1}{2}\theta_{cm})$$

and a sum over all permutations of the constituents a,b,c,d is implied.[10]

Since the disintegration and formation of hadrons are governed by processes which involve transverse momenta of the order of 300 Mev/c, any final state hadron with a transverse momentum much larger than 300 Mev/c is considered to result from a hard collision of hadron constituents.

An early approach[10] to the evaluation of this model involved using quark distribution functions from deeply inelastic e-p and μ-p scattering and fragmentation functions obtained from ν-p scattering to attempt to evaluate the dynamics of the fundamental scattering $d\hat{\sigma}/d\hat{t}$. However, other successes of the theory of quantum chromodynamics (QCD) stimulated an attempt to predict single hadron inclusive cross sections using the premises of QCD[11]. From this point of view the cross section $d\hat{\sigma}/d\hat{t}$ was postulated specifically to be that derived from the scattering of quarks and gluons. Variable parameters in this model were the gluon fragmentation functions, which had not been measured, and the intrinsic transverse momentum distribution of quarks within a hadron. The latter contribution turned out to be crucial in vitiating the direct correspondence between the transverse momentum dependences of $d\hat{\sigma}/d\hat{t}$ and $Ed^3\sigma/dp^3$, which would have forced the prediction of a p_t^{-4} dependence for $Ed^3\sigma/dp^3$. It was found instead that the assumption of a gaussian distribution of quark transverse momenta with a standard deviation of 500 Mev/c, combined with the scale-breaking Q^2 dependence of distribution and fragmentation functions imposed by QCD, resulted in the prediction of a p_t^{-8} dependence of the invariant cross section, and thus good agreement with experimental data.

Several experiments performed subsequently in proton collisions at the Intersecting Storage Rings (ISR) at CERN were able to explore the transverse momentum dependence of the cross

section for the inclusive production of neutral pions up to transverse momenta of 16 GeV/c. In that region the effects of the intrinsic quark transverse momentum are relatively slight and the QCD model predicts a dependence on transverse momentum of p_T^{-n} with n approaching 4 at higher transverse momenta. Indeed the predictions of the model were corroborated by experimental results[12] which indicated that for $7.5<p_T<14$ GeV/c n is equal to 5.1±.4.

Another recent triumph of the QCD model is the successful prediction of the angular dependence in the production of pairs of hadron jets in the collisions of proton with anti-protons at $\sqrt{s}=540$ GeV.[13] The data strongly favor the scattering of vector gluons (the fields which mediate the strong interaction) as the fundamental subprocess, excluding the possibility of scalar gluons.

Atomic Weight Dependence

In 1975 an experiment at Fermilab[14] performed by a collaboration of physicists from the University of Chicago and Princeton University published unexpected results on the atomic weight (A) dependence of the inclusive production of hadrons near 90°. The invariant cross section $Ed^3\sigma/dp^3$ was found to scale with a power of A as expected, but for hadrons with transverse momenta

greater than two GeV/c, the power (α) was measured to be significantly greater than one. This apparent coherent interaction with several nucleons was surprizing in view of the large momentum transfers implied by the large transverse momenta of the final state hadron. The effect was large enough to be easily measured and exhibited a strong dependence on the type of hadron produced. For example, near transverse momenta of six GeV/c, the invariant cross section per nucleon for pion production on tungsten was shown to be fifty percent larger than on beryllium and for proton production the cross section was measured to be more than twice as large as on beryllium.

These measurements have since been confirmed and extended to hadron pair production[15] where such an effect was observed for the production of asymmetric hadron pairs, though α was measured to be consistent with one for symmetrically produced hadron pairs.

The more successful models of this atomic weight dependence in the inclusive production of hadrons at high transverse momenta are those which hypothesize multiple scatters within the nucleus of the parton which is eventually dressed to form the observed final state hadron.[16] It is generally assumed that the formation of the hadron occurs outside the nucleus. Since at least one (and probably all but one) of the scatters is of relatively low momentum transfer, perturbative QCD calculations are excluded and

these models remain disturbingly phenomenological. Furthermore, though the models qualitatively account for values of α greater than one, their predictions for the shape of the dependence of α on p_T do not show particularly good agreement with the measured shape, and the observed dependence on particle type requires further complication.

In 1983 measurements of muon inelastic scattering[17] from nuclear targets at the Conseil Europeen de Recherche Nucleaire (CERN) in Switzerland demonstrated an atomic weight dependence of the structure functions of nucleons. Further measurements at the Stanford Linear Accelerator (SLAC) in California extended the measurements to a large number of nuclei for deeply inelastic electron scattering[18] as well. The ensuing flurry of theoretical interpretations included the hypothesis that quarks are more loosely bound in nuclear matter[19] and the consideration of more conventional nuclear effects involving interactions with the pion clouds surrounding nucleons in nuclei.[20] The magnitude of the effect (10-20% differences between the nucleon structure function in deuterium and that in a nucleus as heavy as tungsten) is slight compared to that observed in the production of hadrons with high transverse momenta. Its effect on the latter process has been calculated and compared to experimental measurements, producing a slight decrease in the expected value of α with transverse momentum above four GeV/c.[21]

CHAPTER III

DESIGN CONSIDERATIONS IN EXPERIMENT 605

IN WHICH the Writer attempts to provide a general list of the principal experimental tricks employed in 605 to improve on previous experiments,a list of the stratagems which originally excited the participants and impressed the review committees.

Experiment 605 proposed to study the inclusive production of charged particles in kinematic regions near the limits imposed by the laws of conservation of energy and momentum. This goal implies two major experimental challenges. First, since the cross sections in this region are very small, an apparatus capable of withstanding the effluvia of a very intense incident beam of protons is required. Second, since the region of acceptance in the production angles and the transverse momenta of these secondary particles is limited to the area covered by the apparatus in the plane perpendicular to the beam direction, a way to limit the size of the apparatus to the level of practicality

and maintain wide angular acceptance must be found. The key to experiment 605 is that the magnet-dump configuration of SM12 (see figure 2) solves these problems, while maintaining an open geometry. Both the suppression of low energy backgrounds and the region of acceptance are enhanced by high magnetic field strength. With the SM12 magnet capable of deflecting a particle of 9 Gev/c transverse momentum into the magnetic spectrometer and a dump subtending an angle at the target in the bend view of ±45 milliradians, the acceptance in transverse momentum extends beyond the kinematic limit and beam intensities of 10^{10} protons/sec were feasible. Thus in a few days of running time the measurements of inclusive single hadron production cross sections smaller than any previously measured at FNAL were completed. Furthermore, the large transverse momentum kick and open geometry allows the apparatus to have good momentum and mass resolution. When effects such as target size, magnetic field measurement error, and wire chamber spatial resolution are reduced to reasonable levels, a momentum resolution of .2% and a mass resolution of .5% are easily obtained.

The opportunity to achieve good mass resolution and high luminosity prompted an emphasis on the detection of pairs of charged particles and the measurement of virtual mass distributions. By making the geometrical acceptance symmetric for positive and negative particles, the detection efficiency for a symmetric pair resulting from the decay of a short-lived heavy

parent particle was optimized. Figure 3 shows the simple case of a short-lived particle of mass M decaying into two oppositely charged particles, each of transverse momentum Mc/2. The trajectories shown occur when the daughter particles exit the interaction point at 90° with respect to the beam direction and the transverse momentum kick of SM12 is equal to Mc/2.

Knowledge of the interaction point and the measurement of the position and angle of a track downstream of SM12 allow one to determine the production momentum vector of a particle originating in the target. These measurements are afforded by the two stations of drift chambers with good spatial resolution. A second magnet, SM3, with a transverse momentum kick of 1 Gev/c, and a station of proportional chambers with high rate capability are added to provide a measurement of the production point. Thus station 1 and SM3 are used only to ascertain with relatively poor resolution if the particle originated in the target. The best resolution is obtained by assuming the interaction point to be in the center of the target and using the positions and angles of the track in stations 2 and 3.

Full particle identification is obtained with high efficiency by the sequence of a ring-imaging Cherenkov counter, a calorimeter, and the proportional tubes behind the calorimeter. The calorimeter is segmented such as to allow the separation of electromagnetic and hadronic showers, thus distinguishing

electrons from hadrons. The Cherenkov counter provides the exclusive identification of pions, kaons, and protons. Finally, after additional hadron absorber, a muon detector completes the ability to identify all charged particles.

CHAPTER IV

TECHNICAL INFORMATION ON THE APPARATUS

IN WHICH the Reader is apprised of enough information to build his own E605.

The following description of the apparatus will refer to a right-handed coordinate system (see figure 4). As one faces the apparatus from the upstream end of the SM12 magnet, $\hat{z}$ points straight ahead, $\hat{x}$ points left, and $\hat{y}$ points up. The origin $(x,y,z)=(0,0,0)$ is at the center of the SM12 aperture in the x and y dimensions and at the upstream pole face of SM12 in the z dimension. This point was surveyed to be 748′ 1" above sea level.

Beam

The beam used in the Spring of 1982 was produced by diffractive scattering of the primary 400 Gev/c proton beam arriving from the main ring accelerator. Beam transport programs

used to simulate the beam for the purpose of designing the beam line indicated the beam had an angular divergence of .15 ± .05 milliradians (RMS) in the x dimension and of .25 ± .05 millradians (RMS) in the y dimension. Measurements made by scanning the 1 millimeter wide targets through the beam indicated the beam was .4 ± .1 millimeters (RMS) wide in the y dimension. Track reconstruction analysis measured the beam size to be 5.0 ± 1.5 millimeters wide in the x dimension. Due to the incomplete construction of the beam line during the test run, the beam was struck the target at an angle of 11 mrad with respect to the spectrometer axis in the x direction and at an angle of 3.4 mrad in the y direction.

The beam arrived in spikes (called buckets) less than one nanosecond wide and 18.9 nanoseconds apart during a period of one second (called a spill) every 10 seconds. The intensity was about 5×10^9 protons/spill.

Targets

Targets of beryllium, copper, and tungsten were used in the 1982 run. See table I for their dimensions. An horizontal scan target was added to the target holder for measurement of the horizontal size of the beam. (This measurement yielded a width

consistent with the result quoted above from the track reconstruction analysis.) Figure 5 shows the target holder with targets. The target lengths were determined such that roughly ten percent of the incident beam particles would undergo inelastic nuclear collisions. Thus an average of ten interactions occurred per bucket, an interaction rate of 500 MHz.

Targeting Monitors

A four-fold coincidence counter constructed as a lead-scintillator sandwich was set up at the z position of the target perpendicular to the beam. The rate in this counter was monitored on a spill-by-spill basis and served to measure the number of protons interacting in the target each spill. It was calibrated by comparing its counting rate to the activation of aluminum and copper foils placed in the incident beam during a dedicated run.

The SM12 Magnet

The SM12 dipole magnet coils and yoke were engineered and assembled at FNAL. Two thousand tons of steel from the Nevis Laboratories cyclotron were used in the fabrication of the yoke.

It was installed in the Meson Lab during December, 1981 and January, 1982. Figure 2 shows the aperture and yoke configuration of the magnet. The trajectories of charged particles are bent in the y-z plane. The aperture in the x direction increases with z to accomodate all particles produced with an x angle less than 30 milliradians. This results in the field shape shown in figure 6 a). This shape had the added advantage of causing the low momentum charged backgrounds to interact in the upstream end of the open aperture, furthest from the wire chambers. The total transverse momentum kick of the SM12 magnet was .52 GeV/c. The size of the upstream end of the beam dump was determined by compromising the acceptance with background rate considerations. During background studies before the data run the y dimension of the dump nose was increased from ±7 centimeters to ±8.9 centimeters. The improvement in background rates was attributed primarily to the degradation of the neutral particle flux produced at small angles in the y-z plane.

Another substantial improvement in the background rates was afforded by the addition of lead brick baffles along the edges of the SM12 aperture.

The SM3 Magnet

The SM3 magnet coils were built in Japan. The four hundred tons of steel for the yoke (also from the Nevis Laboratories cyclotron) were assembled at FNAL and the magnet was installed during February of 1982. The open aperture was about 130 cm x 170 cm over its 320 cm length, with a slight taper, the x dimension increasing slightly with z. The field shape is shown in figure 6 b). The total transverse momentum kick of this magnet was .7178 GeV/c.

Hodoscopes

Six planes of hodoscope counters graced the E605 apparatus. Table II gives their various parameters. All counters were made from NE110 scintillator, the light signal from which was amplified by Hamamatsu R329 phototubes. Clip lines installed on the signal cables at the phototube end enabled time resolution for the hodoscopes to be less than the time between buckets, that is, the hodoscope counter dead-time was under 19 nanoseconds.

Wire Chambers

Table III gives detailed information on the twenty-plane wire chamber system. The six planes of proportional chambers used in station 1 had previously served experiment 494[15] at FNAL and the same amplifier-discriminators were also used for those chambers. The six pairs of drift chamber planes in stations 2 and 3 were built in a collaborative effort by Nevis Laboratories and FNAL. The readout electronics was designed and built by Nevis Laboratories.

Two planes of proportional tubes built by the University of Washington were placed behind the calorimeter for muon detection. Amplifier-discriminators of the type installed in station 1 were used in these counters.

Calorimeter

The calorimeter was divided longitudinally into an electromagnetic shower detector and a hadron shower detector. The former consisted of four longitudinal segments and the latter of two. Specifications of the calorimeter are shown in table IV. Its design was based on tests of a prototype in a test beam-line at FNAL[22]. For details of the construction and operation of the

calorimeter, see the doctoral dissertation of Dr. Yoshihide Sakai[23].

Ring-Imaging Cherenkov Apparatus

The radiator vessel for the Cherenkov detector was an aluminum box which measured 3 meters by 3 meters by 15 meters. Helium was chosen as the radiator gas and a helium purification system which circulated about one volume of helium every ten hours limited the oxygen contamination to less than .2 ppm[24]. A multi-step avalanche chamber[25] detected the Cherenkov photons. The design of the detector included two such chambers, but only one was available for the 1982 run. As a result the array of eight spherical mirrors at the downstream end of the radiator vessel was installed so as to focus all photons to the eastern detector port only. Furthermore, these eight mirrors covered only half the aperture in the x direction. (The full complement of sixteen mirrors and two detectors was installed for the subsequent data run in the winter of 1983-84.)

The multi-step avalanche chamber was isolated from the radiator gas by calcium-fluoride windows to optimize the transmission of ultra-violet photons. The chamber gas consisted of a 97% helium - 3% tri-ethylamine mixture. The helium served

as the drift and avalanche propagation medium; the tri-ethylamine served as the photon conversion medium. The pulse height on cathode wires 45 degrees relative to the anode wires were digitized, as were the anode pulse heights. Two-dimensional reconstruction of the avalanche sites permitted the resolution of individual photons in multi-photon events.

CHAPTER V

DATA ACQUISITION

IN WHICH the conversion of the analog electronic outputs of the machines described above to a digital format comprehensible to the PDP-11/45 computer is considered.

During a typical one-second spill five billion protons were incident on the metal target, each producing several secondary particles. Most of these secondaries were absorbed in the beam dump. Nevertheless the magnetic spectrometer downstream of SM12 was required to operate in a high rate environment. Each hodoscope plane counted about ten million hits per spill. The requirement of at least three of the four hodoscope planes X1,Y2,X3,Y3, to be in coincidence was satisfied three million times during the spill. (Clearly the singles rates in these planes were highly correlated.) The data acquisition system was capable of recording about one thousand events per spill. Hence the challenge presented to the fast trigger logic was to provide

a large rejection factor while remaining efficient for events which contained hadron tracks from the target.

Trigger

In order for an event to be written to magnetic tape, two levels of requirements on the information from the apparatus had to be satisfied. The first level will be referred to as the TFI (Trigger Fan In), and the second will be known as the TGO (Trigger Generator Output). See figures 7 a) and b) for diagrams of the trigger logic. The TFI signals were generated at a rate of about ten kiloherz. The logical OR of these signals was used to strobe two sixteen channel busses, each channel carrying some trigger information which had been stored prior to the TFI strobe. Trigger cards on the strobed busses (DC logic busses) defined logical functions of the sixteen channels available to them, forming the TGO signals. The logical OR of the TGO signals was the condition used to generate the readout of an event to magnetic tape.

The hodoscope signals from the phototubes were shipped to Lecroy 4416 discriminator via RG-58 cables of lengths such that they arrived at the discriminators synchronized to within ten nanoseconds for all possible trajectories. (An exception was the

Y1 hodoscope bank, which arrived ten nanoseconds late and was not used in the trigger at the TFI level.) After discrimination the hodoscope signals were strobed by the accelerator RF pulse which times the arrival of the buckets. This was done in the Pulse Stretcher circuits designed and built by the University of Washington. The timing diagram for the circuitry producing synchronized hodoscope signals is shown in figure 8. The outputs of the Pulse Stretchers were sent to data latches (see Coincidence Registers below) to be later read out to magnetic tape. They were also used to strobe the Trigger Matrix (designed by the State University of New York at Stony Brook), which was a set of memories in which were stored the hodoscope counter patterns corresponding to single particles passing through the open aperture of the apparatus. The sixteen channel flat cables, each carrying the signals from half a bank of hodoscopes, were terminated in modules (Matrix Terminators) which also provided the logical OR of the signals as an output.

Fast calorimeter trigger signals were also available. These were discriminated analog sums from the right and left halves of the calorimeter separately (HL,HR). The TFI signals for hadron data were found from these and the Matrix Terminator signals:

3/4 HL = HL·(At least three of(X1L,Y2L,X3L,Y3L))

3/4 HR = HR·(At least three of(X1R,Y2R,X3R,Y3R))

The DC logic bus bits included the outputs of the Trigger Matrix and calorimeter sums discriminated at different levels (HLO,HHI,CH). The Trigger Matrix produced four types of allowed combinations:

1. all allowed combinations of Y1,Y2,and Y3 hodoscope counters for particles produced in the target and traversing the open aperture of the apparatus above (YUL and YUR) or below (YDL and YDR) the dump in SM12,

2. all allowed combinations of X1 and X3 counters for particles from the target on the left (XL) or right (XR) side of the apparatus,

3. all allowed combinations of X1 and X3 counters for particles from the target which passed through the Cherenkov detector mirrors on the left (CXL) or right (CXR),

4. all allowed combinations of Y3 and Y4 counters for particles from the target which passed through the open aperture above (MUUP) or below (MUDN) the dump in SM12.

Single hadron TGO requirements were

$$TY \cdot HHI = HHI \cdot (YUL \cdot XL + YDL \cdot XL + YUR \cdot XR + YDR \cdot XR)$$

$$HCL = HL \cdot (YUL \cdot CXL + YDL \cdot CXL)$$

$$HCR = HR \cdot (YUR \cdot CXR + YDR \cdot CXR)$$

where · denotes a logical ´and´ operation and + denotes a logical ´or´ operation.

These trigger requirements, which were tuned by varying the calorimeter thresholds, resulted in a TGO rate of a few hundred per spill, an acceptable rate to write to magnetic tape. Upon receipt of a TFI signal, about 130 nanoseconds were required to make a TGO decision. Thus the fast trigger logic introduced a dead-time of less than .2%.

Event Storage

The data from the rest of the apparatus was stored on transmission cables while trigger decisions were being made. After trigger conditions were established gates were sent to the various readout systems to latch the event pending readout to a buffer memory. These readout systems are described below.

Coincidence Registers

The coincidence registers were simple 32-channel data latches originally designed and built by Nevis Laboratories in the early 1970's. They were used in E605 to latch 5056 channels of proportional chamber information, 286 channels of proportional tube information, and 262 channels of hodoscope information. The proportional chamber signals from Y1A,U1A, and V1A arrived earlier than the TGO decision could be made, so these signals were gated with the TFI conditions, then reset if there was no subsequent TGO. The gate width for the hodoscopes was thirty nanoseconds wide, so two buckets contributed to the data for one event written to tape, though the hodoscope trigger itself had single bucket resolution.

The coincidence register cards in one crate (a maximum of 23) were read out through encoder cards to the Nevis Laboratories Data Transport System (see below.) The encoders' output consisted of an encoded sixteen-bit word for each bit set in the concidence registers and a final word containing the word count.

Time-to-Digital Converters (TDC's)

The drift chambers of stations 2 and 3 were read out to 1984 channnels of TDC's. The TDC readout system was developed for the experiment by the Nevis Laboratories electronics group. The TDC's latched Gray-coded time information for thirty-two channels apiece. Modules referred to as Segmenters encoded channel numbers for each hit and sent the data in sixteen-bit words to the Data Transport System.

The station 2 chamber signals were gated on the TGI condition and reset in the case of no TGO. Station 3 information was gated on the condition of TGO. The two gates were 150 nanoseconds and 270 nanoseconds long respectively.

Analog-to-Digital Converters (ADC's)

The calorimeter phototube signals were sent to an ADC system designed and built by Daniel M. Kaplan at Nevis Laboratories. Passive current splitters divided the signal between the ADC inputs and the summing circuitry for the trigger logic. The Nevis ADC's had bin widths which varied quadratically with bin number to allow a large dynamic range. They were read out with Segmenter modules similar to those for the TDC's.

The Cherenkov detector's multi-step avalanche chamber signals were converted to digital information by Lecroy ADC's (2280). These ADC's were read out with CAMAC standards. As a result, events which contained Cherenkov information took several milliseconds (as opposed to tens of microseconds for events without Cherenkov information) to read out. The rate of these events was limited by raising the calorimeter threshold requirement in the trigger in order to reduce the total readout dead-time.

The Nevis Data Transport System

The Nevis Laboratories Data Transport System is a general purpose, flexible data handling system under development since 1977 and used in a number of experiments in which Columbia University has participated since then. Its organization and performance in this experiment are described extensively in reference 26. Its primary purpose was to receive the eight data streams from the readout subsystems, add an identification word to each, and format a data stream to be written to a buffer during the beam spill. Running at a clock rate of two hundred nanoseconds per sixteen-bit word transfer, the Transport System was capable of transmitting one thousand events of two hundred and fifty words each with a dead-time of less than 5%.

The Megamemory

The Megamemory was a buffer developed by the University of Washington with a capacity of a million bytes of information. An interface to the Transport System enabled it to accept data at the rate of two hundred nanoseconds per 16-bit word. (A typical event consisted of about three hundred of these words.) The Megamemory was addressed directly by the PDP-11/45 via Unibus link. Its contents were read out by the PDP-11/45 and written to magnetic tape during the nine seconds between beam spills.

CHAPTER VI

The Data Run

IN WHICH the chronological sequence of events during the all-too-few months between magnet construction in the Meson Hall and the end of this data run finds itself. In this CHAPTER a thoroughly dishonest but sincere attempt is made by the Writer to ascribe orderliness and logic to a time remembered (and depicted by the logbooks) as utter chaos.

The apparatus employed in experiment 605 was installed in the Meson Lab during the period of time between January and March of 1982. During the month of April the data acquisition system was installed and the electronic link of information transfer from the detectors to the PDP-11/45 was established. Protons of 400 Gev/c momentum were transported down the Meson East beam line for the first time in May. Fine tuning of that beam continued throughout the month of May. Major efforts in May included synchronizing the trigger elements and various detectors to the same bucket of incident protons and modifying the configuration of absorbers in the SM12 magnet to minimize the rate of low

energy background particles incident on the detectors. Important results were the addition of the lead brick baffles evident in figure 2 and the size of the dump nose shown in figure 9. (The asymmetry in its shape was dictated by mechanical constraints rather than background rate considerations.) The first data used in the present physics analysis were recorded on June 10, 1982.

CHAPTER VII

THE DATA ANALYSIS

IN WHICH a time-honored means of extracting cross sections from data rates using Monte Carlo computational techniques is described. Neither historical nor technological, this CHAPTER deals primarily in integrals.

The Extraction of a Cross Section from a Raw Data Distribution

In this chapter we will consider means of calculating the single particle inclusive invariant cross section $Ed^3\sigma/dp^3$ given the raw data distribution and the luminosity. The yield of single particles produced in a given time interval is

$$\frac{d^3N}{dp^3} = L\,\frac{d^3\sigma}{dp^3}$$

where L is the luminosity integrated over that time interval. The distribution recorded by the apparatus is

$$\frac{d^3N}{dp^3} = L\,\varepsilon(\vec{p})\,\frac{d^3\sigma}{dp^3} \qquad 0\leq\varepsilon(\vec{p})\leq 1$$

where $\varepsilon(\vec{p})$ is a complicated function including the acceptances and efficiencies of the apparatus. The analysis presented here evaluated $\varepsilon(\vec{p})$ by means of the Monte Carlo method of numerical integration. In general terms, a hypothetical cross section and a software simulation of the apparatus are used to produce an emulation of a raw data tape. The simulation of the apparatus included all multiple-scattering and energy-loss effects, as well as an accurate geometrical survey of the apparatus and efficiency algorithms for all the detectors. If the hypothetical cross section is similar to the actual cross section, then subjecting the Monte Carlo data to the analysis used for the raw data will yield a determination of $\varepsilon(\vec{p})$. A more detailed description follows.

Consider first the simple case of perfect experimental resolution. In this case the measured variable is identical to the momentum vector with which the particle was generated, and we can write simply

$$\varepsilon(\vec{p}) = \frac{d^3N^{Anal}/dp^3}{d^3N^{Gen}/dp^3}$$

where d^3N^{Anal}/dp^3 is the distribution of Monte Carlo events written to tape and surviving the analysis cuts. D^3N^{Gen}/dp^3 is the Monte Carlo input distribution, generated according to the hypothetical cross section.

In the case of finite resolution one must consider a function which relates the distribution as a function of measured quantities $\vec{p}\,'$ to the distribution as a function of the quantities $\vec{p}$ with which the particle was actually produced.

$$\frac{d^3N^{Anal}}{dp'^3} = \int F(\vec{p},\vec{p}\,') \frac{d^3N^{Gen}}{dp^3} dp^3$$

The Monte Carlo method allows us to determine on a statistical basis the $\vec{p}\,'$ measured for a particle produced with momentum $\vec{p}$.

Absorbing $\varepsilon(\vec{p})$ into this function and averaging over the distribution of generated variables we may create the correction function $C(\vec{p}\,')$ such that

$$\frac{d^3N^{Raw}}{dp'^3} = L\ C(\vec{p}\,') \frac{d^3\sigma}{dp^3}$$

This correction function may be calculated from the analysis of Monte Carlo data.

$$C(\vec{p}\,') = \int \frac{d^3N^{Anal}/dp'^3}{d^3N^{Gen}/dp^3} dp^3 \Big/ \int dp^3$$

It should be noticed that the Monte Carlo method provides $C(\vec{p}\,')$ averaged over a finite volume dp^3. It is therefore important that the shape of the hypothetical input cross section emulate that of the actual cross section.

This definition of the correction function implies that the raw data distribution d^3N^{Raw}/dp'^3 will be proportional to the analyzed Monte Carlo data d^3N^{Anal}/dp'^3 if and only if the measured cross section $d^3\sigma^{meas}/dp^3$ is proportional to the hypothetical cross section assumed in the Monte Carlo generation $d^3\sigma^{hyp}/dp^3$. That is

$$\frac{d^3N^{Raw}}{dp'^3} \propto \frac{d^3N^{Anal}}{dp'^3} \iff \frac{d^3\sigma^{meas}}{dp^3} \propto \frac{d^3\sigma^{hyp}}{dp^3}$$

For the purposes of this analysis we will consider the invariant cross section as a function of three variables defined in figure 10: transverse momentum (p_t), production angle in the proton-nucleon center-of-momentum system (θ^*), and azimuthal angle (ϕ). Assuming the absence of spin polarization of either the beam or the target we will assume the invariant cross section is independent of ϕ and calculate it as a function of p_t and θ^*:

$$E\frac{d^3\sigma}{dp^3} = \frac{1}{L}\frac{\sin^2\theta^*}{p_t}[C(\vec{p})]^{-1}\frac{d^2N}{dp_t d(\cos\theta^*)}$$

where L is the integrated luminosity,

$C(\vec{p})$ is the correction function defined above averaged over ϕ, and

$d^2N/dp_t d(\cos\theta^*)$ is the number of raw data events in the interval defined by $dp_t d(\cos\theta^*)$, divided by the area of the interval.

We thus obtain the invariant cross section by dividing the raw data in a given p_t and $\cos\theta^*$ interval by a correction factor for that interval obtained via the Monte Carlo computation. This correction function may yield questionable results if the resolution-smearing correction moves a substantial number of events across bin boundaries. This can happen if the bin sizes are comparable to or smaller than the resolution and the problem is aggravated by steeply falling distributions. For example, events which are resolution-smeared into kinematical regions where the cross section is very small may appear to yield a measurement of the cross section when in fact the integrated luminosity is inadequate to allow such a measurement. In the analysis described here bin sizes at least six times the resolution were used in order to yield a reasonable statistical error in each bin. A worst-case estimate of the error induced by

the finite resolution may be obtained by considering the smeared, steeply falling, transverse momentum distribution. Let us calculate the deviation of the smeared, measured distribution $D'(p_t)$ from the generated, unsmeared, distribution in the case of an exponentially falling distribution $D(p_t)=e^{-\alpha p_t}$ and experimental resolution σ.

$$D'(p_t') = \int D(p_t) \frac{e^{-(p_t-p_t')^2/2\sigma^2}}{\sqrt{2\pi}\,\sigma} dp_t$$

$$= e^{-\alpha(p_t'+\alpha\sigma^2/2)}$$

The resolution in transverse momentum is not worse than .036 Gev/c in any region of phase space and the shape of the most steeply falling distribution is a good approximation to $e^{-\alpha p_t}$ where α=2.75. These numbers yield

$$\frac{D'(p_t)}{D(p_t)} = e^{\alpha^2\sigma^2/2} = 1.0039$$

Hence, due to the good resolution, we find that this uncertainty is far smaller than the statistical and normalization uncertainties, which are about 10 %.

Cuts Imposed on the Raw Data

Stringent requirements on the raw data are desirable in order to ensure that all particles pass cleanly within the confines imposed by the geometrical acceptance. Further cuts were imposed to restrict events to regions where all detectors and the trigger are highly efficient. Following is a descriptive list of all cuts.

1. Tracking

   At least one track must have been reconstructed in the magnetic spectrometer. The tracking subroutines required at least four of the six chambers in station 1 to have fired, and at least three of the six chambers in each of stations 2 and 3.

2. Calorimeter Hadron Identification

   The track was required to point at a cluster of charge deposition in the calorimeter. The energy deposited was also required to match the SM3 magnet momentum determination to within three standard deviations of the calorimeter energy resolution.

3. SM12 Geometrical Aperture Cuts

The algorithm which reconstructed the particle trajectory through the SM12 aperture used the momentum as measured by the SM3 magnet to roughly determine the particle position at the z coordinate of the target. The trajectory was then constrained to originate in the center of the target and a new trajectory (and another momentum) was determined. Aperture cuts were made on the y position of the trajectory at the most stringent aperture points. Table VII shows the surveyed positions and the cuts imposed at the three aperture points in SM12. The cuts were made 2σ wider than the surveyed position of the absorber, where σ is the spatial resolution of the traceback algorithm at the z position of the aperture point. The analysis was repeated with 5σ cuts to ascertain that these cuts affected the final determination of the cross sections only at the level of a few percent.

4. X Angle Limits

The angle of any particle trajectory in the y-z plane was subject to the requirement $.003 < |\theta_x| < .026$. This cut excluded regions of uncertain efficiency due to the construction of the calorimeter, which had a vertical gap around x=0 about 5 centimeters wide.

5. Hodoscope Aperture Requirement

Particle trajectories which passed within 5 centimeters of any edge of the five hodoscope banks upstream of the calorimeter were cut from the final data sample. This cut, combined with the SM12 aperture cuts and the x angle cuts, defined the geometrical acceptance of the apparatus.

6. Trigger Matrix Requirement

Further cuts on individual trajectories ensured that the trajectory considered indeed satisfied the hardware trigger requirements. One such requirement was the trigger matrix, which allowed only specific combinations of the three Y hodoscope bank counters. All trajectories not passing through an allowed combination of these counters were cut. Also, all five hodoscope counters along the trajectory were required to have fired.

7. Calorimeter Trigger Efficiency

The other hardware trigger requirement was that the charge from the calorimeter exceed a specific threshold. Given the track position at the calorimeter and the charge deposited in each module of the calorimeter, one can calculate the trigger efficiency (see Appendix) for

any given hadron trigger (HHI,HL,HR,PSR,PSL). Extensive studies of various calorimeter efficiency cuts determined that this cut had an effect on the cross section which was much smaller than the statistical uncertainties. For the results shown here the minimum hadron trigger efficiency allowed is .50.

Weights Applied to the Raw Data

1. Tracking Efficiency

   The tracking efficiency was calculated for each run using the wire chamber efficiencies and the tracking program requirements (see figure 11). Each track entered into the final raw data sample is weighted by the multiplicative inverse of the tracking efficiency for the corresponding run.

2. Nuclear Absorption in the Apparatus

   There were three principal contributions to the absorption of hadrons upstream of the calorimeter. These were the absorption in the target, the absorption in the Cherenkov counter mirrors (1.8% probability), and the absorption in all the rest of the apparatus upstream

of the Cherenkov mirrors (1.2% probability). (It was assumed that any inelastic collision in the Cherenkov mirrors results in the production of several particles at small angles, ruining the track reconstruction in the station 3 drift chambers.) The largest of these contributions was the absorption in the target. For each track an interaction vertex was generated by Monte Carlo method using the beam parameters. See figure 12 for a picture of the beam size and angle compared to the beryllium target. Given the reconstructed production angle a path length in the target and an absorption probability was computed and used to weight that hadron's contribution to the data sample. Figure 13 shows the absorption probability distribution for the entire raw data sample for the beryllium target.

3. Multi-particle Event Correction

For events in which more than one hadron track from the target is reconstructed (less than .5% of the total data sample), a weight is applied to each track. This weight is equal to the calorimeter trigger efficiency for that track divided by the calorimeter trigger efficiency for the entire event. This weight factor reconciles the raw data sample with the Monte Carlo sample, for which no multi-particle events are generated.

The Monte Carlo Computations

The E605 Monte Carlo analysis program used the CERN software package GEANT[27] to emulate the apparatus and the particle trajectories. Simulation of the development of hadron showers in the calorimeter employed an algorithm used by the UA1 experiment at CERN[28]. The goal of this analysis program was to produce as exact an emulation of a raw data tape as possible. This tape of Monte Carlo-generated events was then analyzed by routines identical to those used in the analysis of the raw data and the results compared as a thorough check of the analysis software.

Acceptance and Resolution

The geometrical acceptance as a function of the generated kinematical variables for positive and negative particles is shown in figures 14-19. Also shown are these acceptances with the calorimeter trigger HHI efficiency folded in. Due to the non-uniformity of gain calibration in the calorimeter and the angle of the beam in the y-z plane, the detection efficiency of the TY.HHI trigger for positive particles is substantially greater than that for negative particles.

The resolution in the measurement of these variables by the apparatus and analysis program for the three targets is shown in figures 20-22. The dependence of the measurement resolution on each kinematical variable varies with the target, due to the different multiple scattering contributions and different sizes of the three targets. The data from the beryllium target suffer primarily from the uncertainty of the vertex position, while the tungsten target data were smeared most significantly by the multiple scattering of the secondary particle in the target material.

A number of evaluations of the systematic errors induced by the Monte Carlo were carried out. Due to the large effect of the HHI trigger efficiency, successful emulation of the spatial distribution of tracks in the x and y dimensions at the calorimeter was essential. Figures 23 and 24 exhibit the degree of likeness of the Monte Carlo and raw data distributions.

The Correction Function

The correction function as defined above is essentially the detection efficiency corrected for resolution smearing effects. The Monte Carlo computation absorbs the Jacobian factor into this correction function such that the raw data distribution divided

by this correction function and by the integrated luminosity yields the invariant cross section directly. Figure 25 shows the correction function for positive hadrons from the beryllium target. The ratios of the beryllium target correction function to those for the copper and tunsten targets are shown in figures 26 and 27. Figures 28-30 show the correction function and ratios for negative hadrons. The uncertainties indicate the statistical limitations imposed by the finite number of events generated for each target.

Normalization

The raw data from the beryllium target were normalized by a calibration of the targetting monitor described in chapter IV via the activation of copper and aluminum foils. The targetting monitor was then calibrated for the other two targets by comparing its counting rate to that of a secondary emission monitor placed in the beam. Due to uncertainties in this cross-calibration, the normalization uncertainties (limit of error) for the copper and tungsten target data are 15% and 12% respectively, while the normalization uncertainty for the beryllium target data is 8%. The uncertainty in the beryllium target data is dominated by the uncertainty in the targetting fraction at the time the foils were irradiated.

Table VI shows the integrated luminosities on each target. The foil calibration provides us with the total number of protons incident on the target (P.O.T.) per targetting monitor count. The integrated luminosity, corrected for the attenuation of the beam in the target, is then obtained via

$$\int L\, dt = (P.O.T.)\ \rho\ L_{eff}\ N_A$$

where the effective target length L_{eff} is calculated from the total inelastic p-N cross section σ_{pN}^{in}.

CHAPTER VIII

THE RESULTS

IN WHICH the physical measurements obtained by this research effort are enumerated and placed in the context of our present understanding of hadronic interactions in general.

The Transverse Momentum Dependence of the Invariant Cross Section

The transverse momentum dependence of single hadron production in proton-nucleus collisions has been well measured previously,[14,15] albeit with poorer resolution and a narrower angular coverage. A typical parameterization[10] for this dependence at a fixed production angle is

$$E \frac{d^3\sigma}{dp^3} = A\, p_T^{-n}\, (1-x_T)^b .$$

Since the measurements described in this dissertation were all taken at a fixed center-of-mass energy, it is impossible to

distinguish the x_T dependence from the p_T dependence. We therefore choose to fix b at a value measured by other experiments[14] (namely b=8.0) and fit the data with the above parameterization. It should be borne in mind as one interprets the fit results that the parameters b and n are highly correlated. Thus a change in b would result in a similar change in n.

The steep dependence on p_T observed by previous experiments is confirmed by these data. We also present the dependence of n, as a measure of the steepness of the cross section, on the production angle θ^*. Table VII shows the values of A and n for the different angular regions covered and for each target. Figures 31-36 show the corresponding cross sections. The vertical error bars indicate statistical errors only. There are global normalization errors of 8%, 15%, and 12% for the beryllium, copper, and tungsten cross sections respectively. The horizontal error bars are simply the bin size divided by $\sqrt{12}$.

A standard parameterization of the atomic weight (A-) dependence of these cross sections is

$$\frac{d^3\sigma_A}{dp^3} = A^{\alpha} \frac{d^3\sigma_o}{dp^3}$$

where α and $d^3\sigma_0/dp^3$ are variable parameters. The data presented here confirm the power law dependence of the cross sections on A, as well as the values of α greater than 1 determined by previous experiments and consistent with constituent multiple scattering models (see chapter II). Figures 37 and 38 exhibit the dependence of α on transverse momentum. The error bars indicate statistical errors. Due to the relative uncertainties in the normalization for the three targets, there is a global uncertainty of .03 in all measurements of α.

The Angular Dependence of the Invariant Cross Section

The angular dependence of the invariant cross section is a convolution of kinematical constraints (that is, the x dependence of the nucleon structure functions) and the angular dependencies of the constituent scattering cross sections. The relevant structure functions in the region the data cover fall with x. Therefore we can expect them to contribute a drop in the cross section as the production angle deviates from 90° at fixed transverse momentum, since the average x of the constituents increases as we approach the kinematic limit. Lloyd-Owen et al have reported that measurements at low x_T ($x_T \leq .1$);[29] indicate that a drop of a factor of two becomes evident at $|\theta^* - 90°| \approx 70°$, far outside the range of acceptance for experiment 605. The authors, however, also show that their results are inconsistent with the

kinematical constraints alone and must include a significant contribution from the angular dependence of the constituent subprocess. If the effects of the structure functions in this kinematical region are significant, then at higher x_T one can expect the drop to occur at angles closer to 90°, since the measurements are made in a region closer to the kinematic limit (see references 30 and 31.) Indeed, our measurement of the inclusive production of positive hadrons (see figure 39) does show such an effect, as a drop of nearly a factor of two is evident already at $|\theta^*-90°|\approx 20°$. The effect is not so clearly evident in the negative hadron data (see figure 40), which cover a smaller angular range and suffer from poorer statistical precision.

The angular dependence of the inclusive h^+ cross section also exhibits an asymmetry about 90°. Two sources of asymmetry will be discussed here. First, at high x_T, where the dominant contributions are from quark-quark and quark-gluon scattering,[30] the constituent scattering cross sections favor forward angles. Furthermore, the structure function for the proton in the x region these data cover is dominated by u quarks while that for the neutron is dominated by d quarks. These considerations lead to the deduction that while proton-proton scattering should yield no asymmetries about 90°, proton-neutron scattering should show an enhancement of positive hadrons in the proton direction and an enhancement of negative hadrons in the neutron direction. Thus

in proton-nucleus interactions we might expect an enhancement of positive hadrons in the forward direction ($\theta^* < 90°$) and an enhancement of negative hadrons in the backward direction ($\theta^* > 90°$).

Another source of asymmetry may arise from the atomic weight dependent effect mentioned at the end of chapter II. Since nucleon constituents in nuclei appear to carry smaller fractions of the nucleon momentum than constituents in a free nucleon, the constituent center-of-momentum frame will appear to be moving in the beam direction as observed in the nucleon center-of-momentum frame (which is the frame in which we calculate the production angle.) Thus the production of all particles will be biased toward production angles smaller than 90°. The magnitude of previously observed effect is comparable to the statistical precision of these data ($\approx$10%), however, and hence we can expect only a marginal measurement of the effect. Its principal identifying characteristic would be an enhancement with atomic weight, that is, α rising at forward angles. Figure 41 shows the dependence of α on production angle. While the data are consistent with such an effect, the statistical precision is such as to preclude an unambiguous confirmation.

Summary of Conclusions

In this chapter a number of physical processes have been described and our measurements compared to the expected manifestations of these processes. In the interest of clarity, let us briefly summarize:

1. The dependence of the inclusive hadronic production cross section on transverse momentum

   Our measurements corroborate the earlier observations of a steep drop ($\sim p_T^{-8}$) of the cross section. The result is consistent with a quantum chromodynamical model, but the agreement requires the inclusion of large effects due to the intrinsic transverse momentum of the nucleon constituents, which must be installed in the model in a rather ad-hoc fashion.

2. The dependence of the inclusive hadronic production cross section on production angle

   A comparison of our results with measurements at lower x_T indicate that effects due to the proximity of the kinematic limit are appreciable. The difference in the

relative shapes of the positive and negative hadron dependencies reflect the presence of neutrons in the target materials, showing that the quark flavor flow in the fundamental constituent scattering is observed. The production of positive hadrons is biased forward, as expected from a simple QCD model, but the production of negative hadrons also shows a slight forward bias, contradicting naive QCD expectations.

3. The atomic weight dependence of the inclusive hadronic production cross section

The primary observation here is the measurement of $\alpha \approx 1.15$ fairly independent of transverse momentum in the kinematic region covered by the data. This result is qualitatively consistent with constituent multiple scattering models, but better measurements and more detailed models are needed before a quantitative understanding of the process can be achieved. The atomic weight dependence measurements presented here further show marginal evidence for the softening of nucleon constituent structure functions in nuclear matter observed in deeply inelastic lepton-nucleus scattering. This effect adds to the forward angular bias in the production of positive hadrons expected from

quark flavor flow in the constituent subprocess, and subtracts from the backward angular bias expected for the production of negative hadrons.

In general, the results obtained from this analysis serve primarily to whet one's appetite for better data. A major improvement would be to have taken data at several beam energies allowing the separation of the p_T and x_T dependencies. A more useful comparison of the production of positive and negative hadrons would be afforded by an acceptance symmetric in the hadron charge and last, but not least, greater statistical precision is desirable, since the systematic errors are small due to the good resolution. All of these improvements were effected in subsequent data runs of experiment 605 and many of the issues described above will be resolved by analysis of the more recent data.

ACKNOWLEDGEMENTS

During the first week of May, 1985 the Symposium on Particle Physics in the 1950's took place at Fermilab. Never before had I been so in awe of name tags. The mere idea that those people dared to wear name tags with those names on them flabbergasted me. Among the many fascinating talks given during the course of the symposium were sprinkled the reminiscences of some of the physicists who had participated in the early experiments at Brookhaven and Berkeley, those who pioneered elementary particle physics research at accelerator laboratories in the United States. It is to this class of individuals that I wish to address a note of gratitude. As an undergraduate student I once had the occasion to attempt particle physics research with little institutional support. At every turn I encountered baffling obstacles. The retail electronics stores in Portland, Oregon simply did not sell transistors of the bandwidth capability I needed to read out my homemade proportional chambers. And how could I possibly measure a cross section without a phototube? According to the catalogue two phototubes cost the equivalent of a year's tuition. This ineffectual attempt at particle physics research, though it was fun, was also dissatisfying and frustrating. As soon as I left college I sought major

institutional support. And I found it, because, as it turned out, thousands of people had devoted more than two decades of effort to create an institutionalized support system for such research. To those physicists who, with relatively little support, demonstrated by virtue of their scientific ingenuity the fruitfulness of experimentation in the field of elementary particle physics and still had the energy to negotiate a research industry with the American people via its federal government, I extend a belated expression of gratitude.

I would also like to acknowledge the efforts of my colleagues on experiment 605. I cannot pretend to fathom their private motivations; I know only that the depth of their commitment to our common goal continually amazed me.

I would also like to emphasize the contributions of the technical staffs of Fermilab and Nevis Laboratories. I admire primarily the professional competence of their work, but on a more personal note I wish to thank them for making our collaboration pleasant as well as successful.

APPENDIX

Calorimeter Trigger Efficiency

The hadron requirement of all five hadron triggers consisted of the summed outputs of the 148 calorimeter phototubes. The sum served as input to a Lecroy 325 rise-time-compensated discriminator, one for each of the five triggers. A logic and timing diagram exhibiting the operation of this discriminator is shown in figure 42. A low threshold was used to determine the timing of the output pulse, which was also contingent upon a higher level threshold imposed a time T_{Delay} after the timing threshold was satisfied. T_{Delay} was set to 15 nanoseconds for all five discriminators.

The charge from each calorimeter phototube passed through a resistive splitter which sent a fixed fraction of the charge to the Nevis ADC system as well as to the linear fan-in used to sum them for the trigger requirement. By setting the pre-scaled hadron trigger levels (PSR and PSL) low enough that they were fully efficient for the higher level triggers(HR,HL,HHI) the

efficiencies of these three triggers could be measured as a function of the charge stored in the ADC's. However, the charge stored in the ADC's was integrated during a 150 nanosecond long gate. If the pulse shape was constant, then one could assume that the pulse height use for the trigger was proportional to the charge stored in the ADC. Furthermore, if the cluster of charge deposits in the calorimeter (A single hadron deposited charge in six to eight counters typically.) was associated with a reconstructed track in the spectrometer, one could be certain that the charge triggering the discriminator was proportional to the ADC charge, because it was coincident in time. (Though the hadron triggers had one-bucket resolution, the ADC charge obviously did not.) Due to the relative duration of T_{Delay} and the ADC gate, only ten percent of the time-random charge in the ADC's could contaminate the charge used by the trigger discriminator.

This means of triggering introduces two strong biases in the momentum selection of the hadrons. Since there was about a forty percent attenuation of the light transmitted through the entire length of a calorimeter scintillator paddle (see figure 43), hadrons of lower momenta satisfied the trigger near the phototubes. The relationship between charge and momentum could be measured directly on an event-by-event basis by comparing the momentum measured in the magnetic spectrometer to the charge deposited in the ADC's.

The second bias in the hadron trigger resulted from the propagation delay of the light through the scintillator paddle. The transit time for the light to travel from one end of a calorimeter scintillator paddle to the other was about seven nanoseconds. The light pulse arriving at the phototube consisted of a direct component, followed by the light reflected off the end of the paddle near the center of the calorimeter. Figure 44 shows how, for an energy deposit near the phototube, the late, reflected, light pulse does not contribute to the pulse height which determines the trigger decision. Since deposits near the center of the calorimeter deliver pulses where the direct and reflected contributions are coincident in time, the trigger efficiency is higher for hadrons near x=0. The dependence of the effective trigger threshold on x position is shown in figure 45.

For the analysis of the calorimeter trigger efficiencies it was assumed that the relationship between the ADC charge and the contribution to the pulse height at the trigger discriminator varied from phototube to phototube. This complicated the determination of the trigger efficiencies, due to the sharing of charge among several phototubes for each hadronic energy deposition. For each counter, the trigger efficiency was modeled as an error function:

$$\varepsilon_i(Q_{ADC},x) = \mathrm{erf}(Q_{ADC}-Th_i(x),\sigma)$$

$$= \frac{1}{\sqrt{2\pi}} \int e^{(y-Th_i(x))^2/\sigma^2}\, dy$$

where Q_{ADC} is the charge recorded by the ADC's, $Th_i(x)$ is the trigger threshold to be determined by analysis of the pre-scaled triggers, and σ is the jitter in that threshold, arising from the ADC resolution (≈2%) and pulse-to-pulse shape variations. The measurement of thresholds as a function of x position (figure 45) indicated that the x dependence of the threshold was linear and similar for all counters:

$$Th_i(x) = Th_i^o + \alpha x$$

where α=.162 pC/cm. The jitter σ was measured to be about 2 pC independent of counter number. The measurement of Th_i^o using the lower threshold hadron triggers was carried out by weighting the calculation of efficiencies for a single counter by the charge contribution of that counter to the sum. That is, for each event weighted contributions to the efficiency calculations of several counters were made. In order to obtain sufficient statistical accuracy the Th_i^o were longitudinally averaged, e.g. the charge from counters 1 of E1,E2,E3,E4,H1, and H2 were all summed to determine Th_1^o . Hence the range of i was from 1 to 26. Table VIII lists the thresholds Th_i^o calculated for each counter for the HL, HR, and HHI triggers.

Given the threshold for each 'counter' (where 'counter' refers to a longitudinal average of six counters) the trigger efficiency for any event was determined in the following manner. We assumed a linear relationship between the charge in an ADC channel and the pulse height contribution to the trigger, where the constant of proportionality depends on the x position of the track and varies from counter to counter:

$$Q_i = K_i(x) \cdot PH_i \qquad 1 \leq i \leq 26$$

$K_i(x)$ has dimensions of volts/coulomb. The efficiency is a function simply of the total pulse height at the discriminator

$$\varepsilon(\Sigma Q_i/K_i(x)) = \mathrm{erf}(\Sigma Q_i/K_i(x) - T, \sigma)$$

where T is the discriminator threshold in volts and σ is the jitter described above. It is not necessary to know the actual value of T , since the error function may be rewritten

$$\mathrm{erf}(\Sigma Q_i/TK_i(x) - 1, \sigma/T)$$

The charge thresholds $Th_i(x)$ are related to the $K_i(x)$ in a simple manner

$$Th_i(x) = T\ K_i(x)$$

The efficiency curve for the pre-scaled hadron events for the HHI trigger threshold in table V is shown in figure 46. The mean value of $\Sigma Q_i/TK_i(x)-1$ is $-.001\pm.002$ and σ/T is $.039\pm.002$. This corresponds to a jitter similar to that measured for a narrow x-slice of a single counter, indicating that this calculation of efficiency handles the x dependence and the counter-to-counter variation correctly.

REFERENCES

1. M. Breidenbach et al., Phys. Rev. Lett. 23 , 935 (1969)

2. J.D.Bjorken, Phys. Rev. 179 , 1547 (1969)

3. R.P.Feynman, Phys. Rev. Lett., 23 , 1415 (1969)

4. F.W.Busser et al., Phys. Lett. 46B , 471 (1973)

5. S.D.Ellis, 7th International Conference on High Energy Physics, London, England, V-23 (1974)

6. M.Gell-Mann, Phys. Lett. 8 , 214 (1964)

7. G.Zweig, CERN report 8182/TH., 401 (1964)

8. R.Blankenbecler,S.J.Brodsky,J.F.Gunion, Phys. Lett. 39B , 649 (1972)

9. H.J.Frisch et al., Phys. Rev. Lett. 44 ,511 (1980)

10. R.D.Field and R.P.Feynman, Phys. Rev. D15 ,2590 (1977)

11. R.P.Feynman, R.D.Field, and G.C.Fox, Phys. Rev. D18 , 3320 (1978)

12. A.L.S. Angelis et al., Phys. Lett. 79B , 505 (1978)

13. G.Arnison et al., Phys. Lett. 136B , 294 (1984)

14. J.W.Cronin et al., Phys. Rev. D11 , 3105 (1975)

15. R.L.McCarthy et al., Phys. Rev. Lett., 40 , 213 (1978)

    H.Jostlein et al., Phys. Rev. D20 , 53 (1979)

16. M.J.Longo, Nucl. Phys., B134 , 82 (1978)

    A.Kryzwicki et al., Phys. Lett. 85B , 407 (1079)

    M.Lev and B.Petersson, Z. fur Phys. C21 , 155 (1983)

17. J.J.Aubert et al., Phys. Lett. 123B , 275 (1983)

18. A.Bodek et al., Phys. Rev. Lett., 50 , 1431; 51 (1983)

19. R.L.Jaffe, Phys. Rev. Lett. 50 , 228 (1983)

H.Faissner and B.R.Kim, Phys. Lett. 130B , 321 (1983)

20. E.L.Berger, Argonne report ANL-HEP-PR-85-70 (1985)

21. T.Ochiai et al., Rikkyo University preprint, RUP-85-4 (1985)

22. Y.Sakai et al, IEEE Trans. Nucl. Sci. Vol. NS-28, 528 (1981)

23. Y.Sakai, Ph.D. Thesis, Kyoto University (1984)

24. M.Adams et al, Nucl. Instr. and Meth. 217 , 237 (1983)

H.D.Glass, Ph.D. Thesis, State University of New York at Stony Brook (1985)

25. R.Bouclier et al, Nucl. Instr. & Meth. 205, 403 (1983)

Ph.Mangeot et al, Nucl. Instr. & Meth. 216, 79 (1983)

26. J.A.Crittenden et al, IEEE Trans. Nucl. Sci. NS-31, 1028 (1984)

27. R.Brun et al, CERN document DD/US/86, revised (1982)

28. M.Della Negra, Physical Scripta, Vol. 23, 469 (1981)

P.K.Bock et al, Nucl. Instr. & Meth. 186, 533 (1981)

29. D.Lloyd-Owen et al., Phys. Rev. Lett. 45 , 89 (1980)

30. R.D.Field, Phys. Rev. D27 , 546 (1983)

31. N.Giokaris, Ph.D. Thesis, University of Chicago (1981)

TABLE CAPTIONS

I. Parameters of the targets

II. Specifications of the hodoscopes

III. Specifications of the chambers

IV. Specifications of the calorimeter

V. Surveyed positions and software cut values for aperture cuts

VI. The integrated luminosities used to normalize the data from each target

VII. The values of the fit parameters A and n for the invariant cross sections per nucleon for positive and negative hadrons from each target. The functional form of the fit is $f(p_T) = A\, p_T^{-n}\, (1-x_T)^8/(p_0^{-n}\, (1-x_0)^8)$, where p_0=6.15 GeV/c and $x_0=2p_0/\sqrt{s}$, so that A is the value of the fit to the cross section evaluated at p_T=6.15 GeV/c

VIII. Calorimeter counter thresholds (Th_i^0) for the HHI trigger

TABLE I

Target Parameters

	Be	Cu	W
Horizontal width (mm)	38.3	38.1	38.1
Vertical thickness (mm)	.996	.914	1.059
Length (mm)	101.8	25.8	13.1
Nuclear weight A	9.01	63.54	183.85
Number of nucleons in unit area ($\times 10^{25}/cm^2$)	1.13	1.39	1.52
Density (g/cm^3)	1.848	8.96	19.3

TABLE II

Specifications of the Hodoscopes

	Hodoscope planes					
	Y1	X1	Y2	X3	Y3	Y4
Z location (m)	21.01	21.04	28.32	46.66	46.92	51.87
Aperture Hor. (cm)	121.9	121.9	162.6	264.2	264.2	294.6
Vert. (cm)	152.4	152.4	172.7	233.7	233.7	254.0
Segmentation Hor. x Vert.	2 x 12	12 x 2	2 x 17	13 x 2	2 x 13	2 x 14
Counter element						
Width (cm)	12.7	10.16	10.16	22.50 (11.03)*	17.78 (19.05)*	17.78 (20.32)*
Length (cm)	60.96	76.20	81.28	116.84	132.08	147.32
Thickness (mm)	4.76	4.76	3.715	6.35	6.35	6.35

*) counters of both ends

TABLE III

Specifications of the Wire Chambers

		Z (m)	Aperture X (cm)	Aperture Y (cm)	Wire space (mm)	Number of wires
Station 1	Y1A	18.91	128.3	149.6	2.0	736
	U1A	19.17	128.3	152.4	1.94	896
(MWPC)	V1A	19.42	128.3	152.4	1.94	896
	Y1B	20.11	128.3	149.6	2.0	736
	U1B	20.36	128.3	152.4	1.94	896
	V1B	20.62	128.3	152.4	1.96	896
Station 2	YY'	27.55	167.6	178.8	10.0	176
(DC)	UU'	27.80	167.6	182.9	9.7	208
	VV'	28.06	167.6	182.9	9.7	208
Station 3	YY'	45.79	269.2	233.3	20.0	112
(DC)	UU'	46.04	269.2	242.6	19.4	144
	VV'	46.30	269.2	242.6	19.4	144
Station 4	PTX	54.81	363.8	315.0	25.4	144
(Prop. Tube)	PTY	55.85	363.2	375.9	25.4	142

TABLE IV

Specifications of the Calorimeter

	Modules					
	E1	E2	E3	E4	H1	H2
Absorber	Pb (3 mm)				Fe(25mm)	Fe(50mm)
Scintillator	Kyowa SCAS1101 (20cm x 148cm x 6mm)				Kyowa SCAS1101 (20cm x 155cm x 6mm)	
Light collection	Acrylic block				WLS (Altulor 1290) + twisted light guide	
Photo tube	R1565 3"ϕ, 6 st.	R1476 (Hamamatsu TV) 5"ϕ, 6 stage			R1565 (Hamamatsu TV) 3"ϕ, 6 stage	
Number of layers	4	9	9	10	12	20
Radiation length	2.41	5.43	5.43	6.03	17.53	58.58
Integral*				21.58	39.11	97.19
Absorption length	0.13	0.28	0.28	0.31	1.90	6.13
Integral*				1.08	2.98	9.11

*) Including X3 and Y3 hodoscopes and Pb sheet (12 mm, 2.27 r.l.) in front of the calorimeter

TABLE V

SM12 Aperture Cuts

Aperture Point	Z Position		Y Position	Cut Position
Dump Nose	173cm	Upper	7.54cm	7.87cm
		Lower	-10.34cm	-10.54cm
SM12 Exit (Outer Limits)	1135cm	Upper	51.38cm	53.59cm
		Lower	-53.72cm	53.34cm
SM12 Exit (Inner Limits)	1179cm	Upper	12.40cm	12.83cm
		Lower	-16.81cm	-17.27cm

TABLE VI

Integrated Luminosities

Target	P.O.T.	L_{eff}	$\int L\,dt$
Beryllium	$(2.26\pm.18)\times10^{13}$	8.84cm	$(2.17\pm.17)\times10^{38}cm^{-2}$
Copper	$(2.42\pm.36)\times10^{13}$	2.34cm	$(3.13\pm.47)\times10^{38}cm^{-2}$
Tungsten	$(1.47\pm.18)\times10^{13}$	1.19cm	$(2.08\pm.25)\times10^{38}cm^{-2}$

TABLE VII

The Cross-section Fit Parameters Λ and n

			Beryllium	Copper	Tungsten
$-.2<\cos\theta^*<-.1$	h^+	Λ	$(6.07\pm.66)\times10^{-36}$	$(7.71\pm.62)\times10^{-36}$	$(7.21\pm.60)\times10^{-36}\,cm^2/(GeV^2/c^3)$
		n	7.21±1.6	9.07±1.1	7.14±1.0
	h^-	Λ	$(4.26\pm.49)\times10^{-36}$	$(4.55\pm.40)\times10^{-36}$	$(4.94\pm.45)\times10^{-36}$
		n	6.47±1.3	8.58±1.0	4.54±1.0
$-.1<\cos\theta^*<.0$	h^+	Λ	$(6.97\pm.41)\times10^{-36}$	$(9.18\pm.39)\times10^{-36}$	$(1.14\pm.05)\times10^{-35}$
		n	8.31±.79	8.03±.52	8.35±.53
	h^-	Λ	$(4.70\pm.39)\times10^{-36}$	$(5.12\pm.33)\times10^{-36}$	$(5.86\pm.35)\times10^{-36}$
		n	8.63±.79	9.31±.69	8.14±.62
$.0<\cos\theta^*<.1$	h^+	Λ	$(1.00\pm.04)\times10^{-35}$	$(1.21\pm.04)\times10^{-35}$	$(1.33\pm.04)\times10^{-35}$
		n	7.63±.42	7.55±.34	8.55±.34
	h^-	Λ	$(4.30\pm.35)\times10^{-36}$	$(5.71\pm.30)\times10^{-36}$	$(6.88\pm.37)\times10^{-36}$
		n	9.79±.94	7.81±.63	9.83±.63
$.1<\cos\theta^*<.2$	h^+	Λ	$(1.07\pm.04)\times10^{-35}$	$(1.31\pm.03)\times10^{-35}$	$(1.52\pm.04)\times10^{-35}$
		n	8.57±.35	8.52±.27	8.65±.28
$.2<\cos\theta^*<.3$	h^+	Λ	$(1.02\pm.04)\times10^{-35}$	$(1.25\pm.04)\times10^{-35}$	$(1.45\pm.04)\times10^{-35}$
		n	8.94±.43	8.95±.33	8.23±.32

TABLE VIII

Calorimeter Counter Trigger Thresholds

Counter	Th_i^o (pC) (Left Side)	(Right Side)
1	47.5	59.4
2	52.1	60.7
3	55.0	59.4
4	51.4	53.6
5	51.2	60.3
6	51.4	60.0
7	50.9	55.1
8	52.2	57.2
9	54.7	56.3
10	50.6	54.5
11	50.2	56.2
12	50.7	57.2
13	52.0	60.2

FIGURE CAPTIONS

1. A schematic depiction of the scattering of two partons from colliding parent nucleons and their subsequent fragmentation into a single hadron and anything else.

2. The magnet-dump configuration of SM12.

3. An illustration of the trajectories of two oppositely-charged particles resulting from the symmetric decay of a heavy, short-lived, neutral parent.

4. A schematic diagram of the E605 apparatus.

5. A diagram of the target holder with the metal targets.

6. The z position dependence of the x components of the SM12 and SM3 magnetic fields.

7. Diagrams of the trigger logic.

8. A timing diagram for the pulse stretcher coincidence logic.

9. A detailed diagram of the dump-nose configuration.

10. A diagram of the kinematical variables used in the data analysis, represented in the E605 coordinate system.

11. The track reconstruction efficiency as a function of run number for the data used in this analysis.

12. The beam size and angle shown relative to the beryllium target.

13. The distribution of absorption probabilities in the beryllium data sample.

14. The acceptance in transverse momentum, both geometrical and with the calorimeter trigger requirement folded in, for positive hadrons produced in the beryllium target. All six plots are shown in arbitrary, but identical, units.

15. The acceptance in the production angle θ^*, both geometrical and with the calorimeter trigger requirement folded in, for positive hadrons produced in the beryllium target. All six plots are shown in arbitrary, but identical, units.

16. The acceptance in the azimuthal angle ϕ, both geometrical and with the calorimeter trigger requirement folded in, for positive hadrons produced in the beryllium target. All six plots are shown in arbitrary, but identical, units.

17. The acceptance in transverse momentum, both geometrical and with the calorimeter trigger requirement folded in, for negative hadrons produced in the beryllium target. All six plots are shown in arbitrary, but identical, units.

18. The acceptance in the production angle θ^*, both geometrical and with the calorimeter trigger requirement folded in, for negative hadrons produced in the beryllium target. All six plots are shown in arbitrary, but identical, units.

19. The acceptance in the azimuthal angle ϕ, both geometrical and with the calorimeter trigger requirement folded in, for negative hadrons produced in the beryllium target. All six plots are shown in arbitrary, but identical, units.

20. The resolution in the measurement of momentum for the three targets.

21. The resolution in the measurement of transverse momentum for the three targets.

22. The resolution in the measurement of production angle for the three targets.

23. The comparison of x and y position distributions for the Monte Carlo computation and the raw data. These distributions are for the positive hadrons produced in the beryllium target.

24. The comparison of x and y position distributions for the Monte Carlo computation and the raw data. These distributions are for the negative hadrons produced in the beryllium target.

25. The correction function for positive hadrons produced in the beryllium target in units of GeV^{-1}.

26. The ratio of the correction function for positive hadrons from the beryllium target to that for positive hadrons from the copper target.

27. The ratio of the correction function for positive

hadrons from the beryllium target to that for positive hadrons from the tungsten target.

28. The correction function for negative hadrons produced in the beryllium target in units of GeV^{-1}.

29. The ratio of the correction function for negative hadrons from the beryllium target to that for negative hadrons from the copper target.

30. The ratio of the correction function for negative hadrons from the beryllium target to that for negative hadrons from the tungsten target.

31. The inclusive invariant cross section per nucleon as a function of transverse momentum for positive hadrons produced in the beryllium target.

32. The inclusive invariant cross section per nucleon as a function of transverse momentum for positive hadrons produced in the copper target.

33. The inclusive invariant cross section per nucleon as a function of transverse momentum for positive hadrons produced in the tungsten target.

34. The inclusive invariant cross section per nucleon as a function of transverse momentum for negative hadrons produced in the beryllium target.

35. The inclusive invariant cross section per nucleon as a function of transverse momentum for negative hadrons produced in the copper target.

36. The inclusive invariant cross section per nucleon as a function of transverse momentum for negative hadrons produced in the tungsten target.

37. The atomic weight dependence parameter α as a function of transverse momentum for positive hadrons.

38. The atomic weight dependence parameter α as a function of transverse momentum for negative hadrons.

39. The inclusive invariant cross section per nucleon as a function of production angle for positive hadrons produced in each target.

40. The inclusive invariant cross section per nucleon as a function of production angle for negative hadrons produced in each target.

41. The atomic weight dependence parameter α as a function of production angle for positive and negative hadrons.

42. The operation of the calorimeter threshold trigger discriminator (Lecroy 325).

43. The x position dependence of the ratio of the charge deposited in the calorimeter by a hadron to its momentum.

44. An illustration of the pulse shape arriving at the calorimeter threshold trigger discriminator.

45. The x position dependence of the calorimeter trigger threshold.

46. The trigger efficiency curve for the HHI trigger.

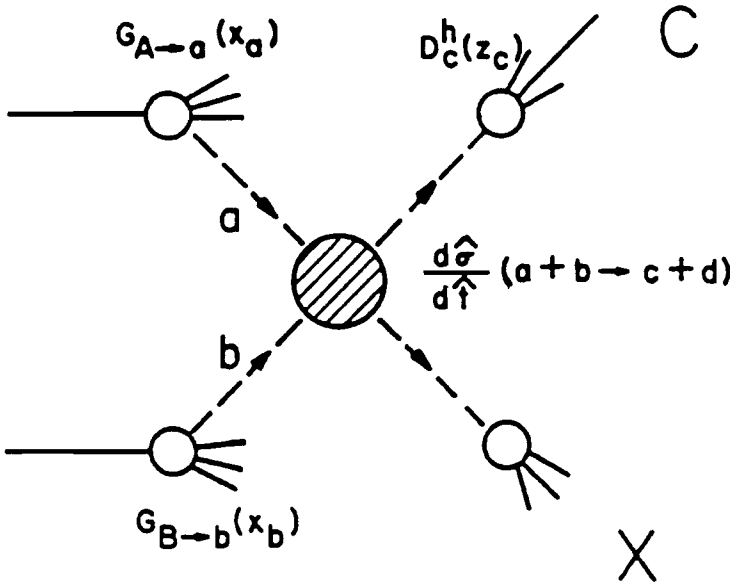

Figure 1

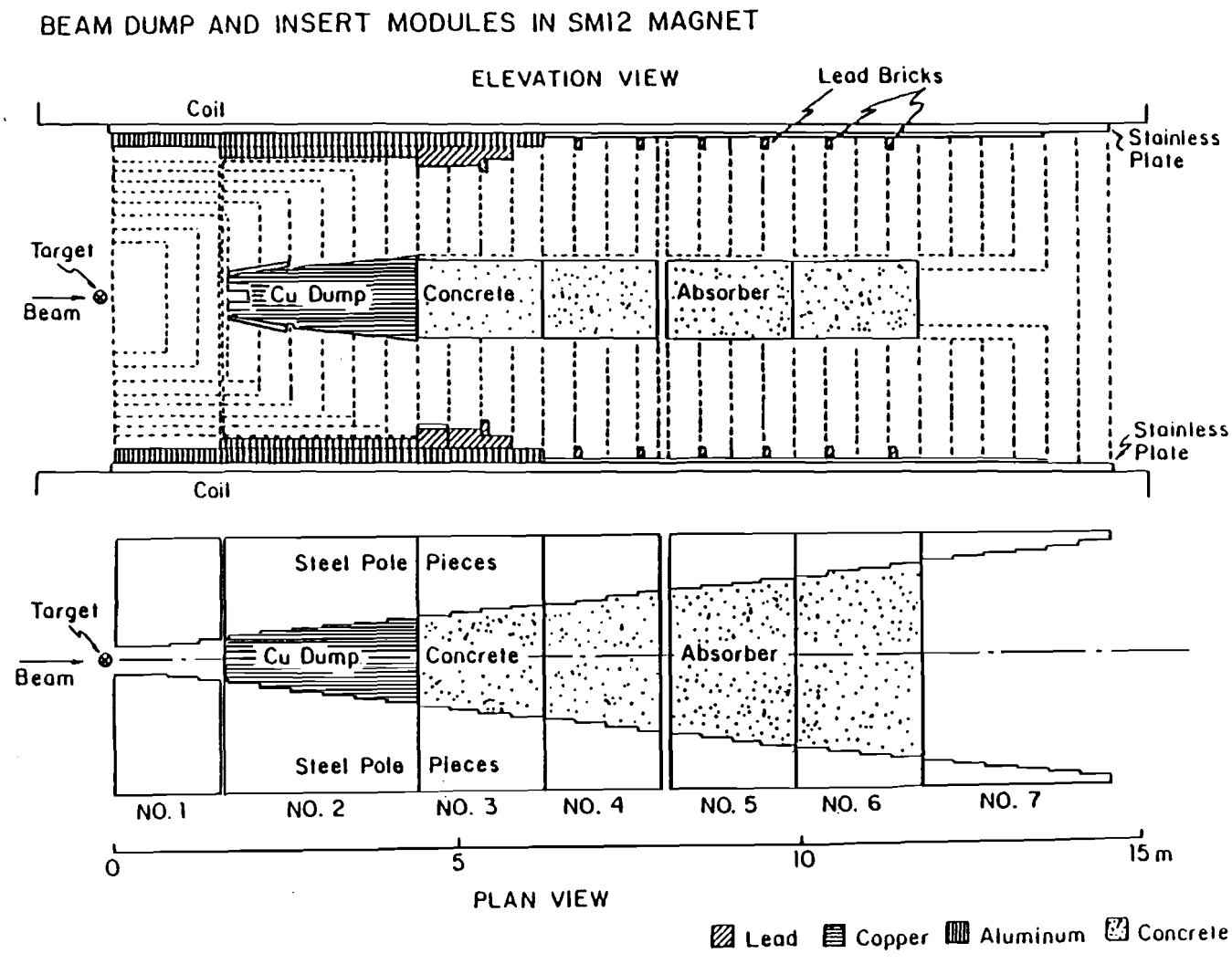
BEAM DUMP AND INSERT MODULES IN SM12 MAGNET
ELEVATION VIEW
Lead Bricks
Coil
Stainless Plate
Target
Beam
Cu Dump
Concrete
Absorber
Stainless Plate
Coil
Steel Pole
Pieces
Target
Beam
Cu Dump
Concrete
Absorber
Steel Pole
Pieces
NO. 1
NO. 2
NO. 3
NO. 4
NO. 5
NO. 6
NO. 7
0
5
10
15 m
PLAN VIEW
Lead
Copper
Aluminum
Concrete

Figure 2

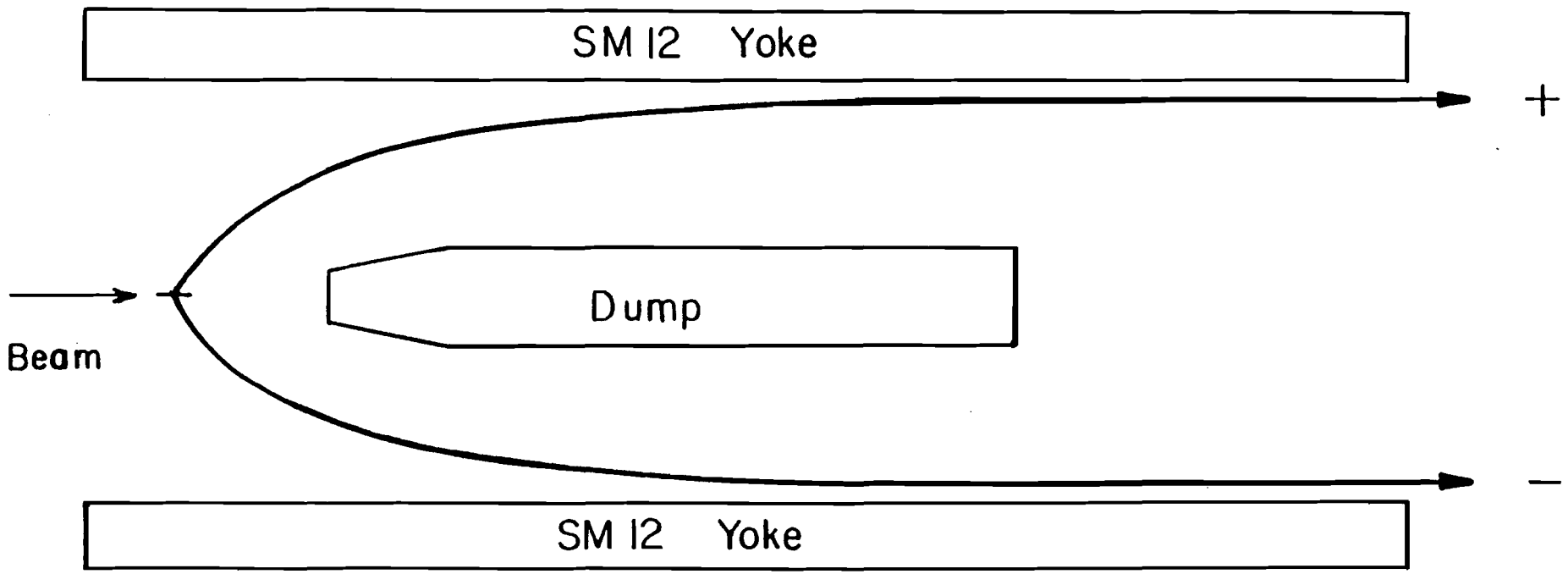

Figure 3

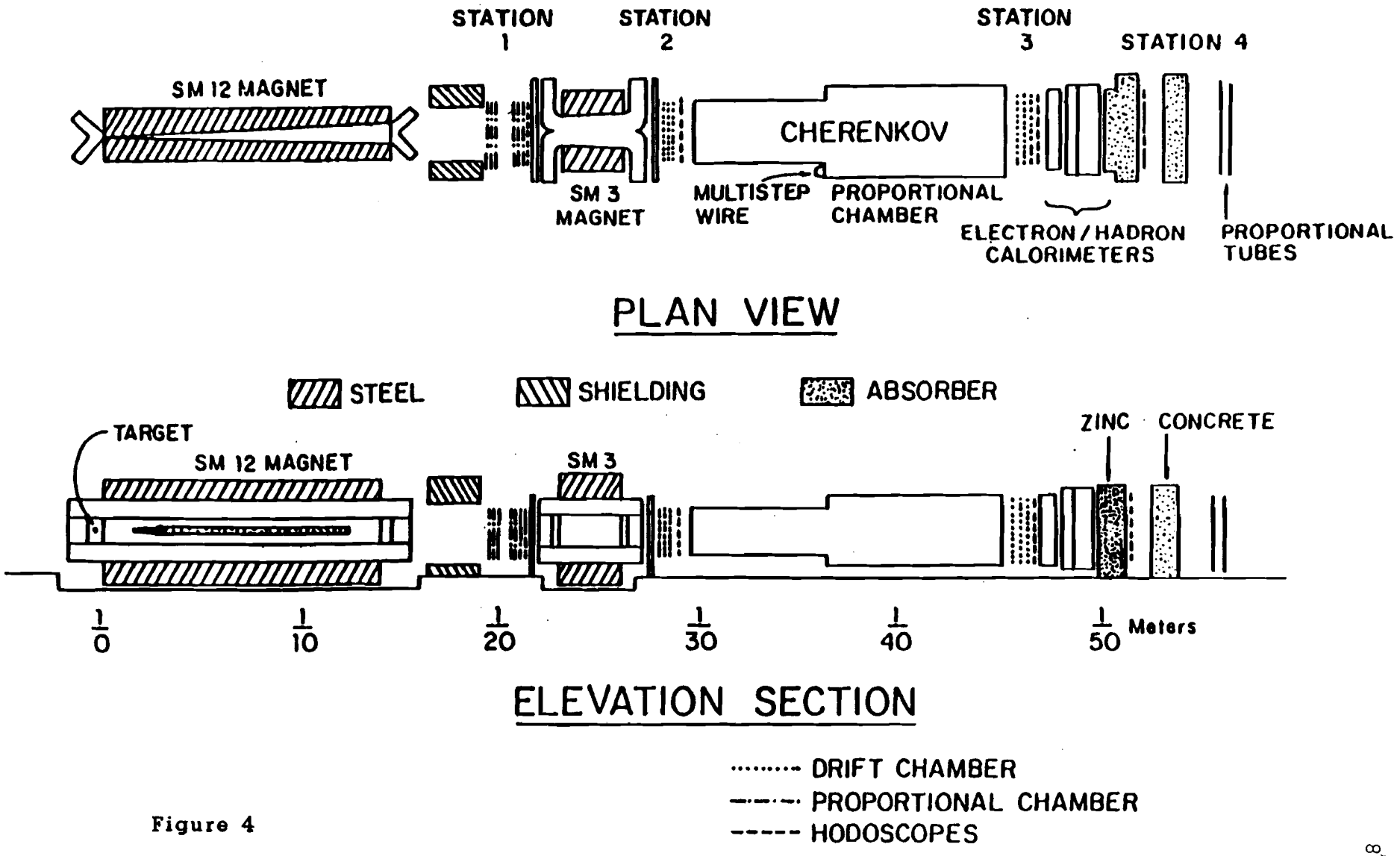
STATION 1
STATION 2
STATION 3
STATION 4
SM 12 MAGNET
CHERENKOV
SM 3 MAGNET
MULTISTEP WIRE
PROPORTIONAL CHAMBER
ELECTRON / HADRON CALORIMETERS
PROPORTIONAL TUBES
PLAN VIEW
STEEL
SHIELDING
ABSORBER
TARGET
SM 12 MAGNET
SM 3
ZINC
CONCRETE
0
10
20
30
40
50
Meters
ELEVATION SECTION
DRIFT CHAMBER
PROPORTIONAL CHAMBER
HODOSCOPES

Figure 4

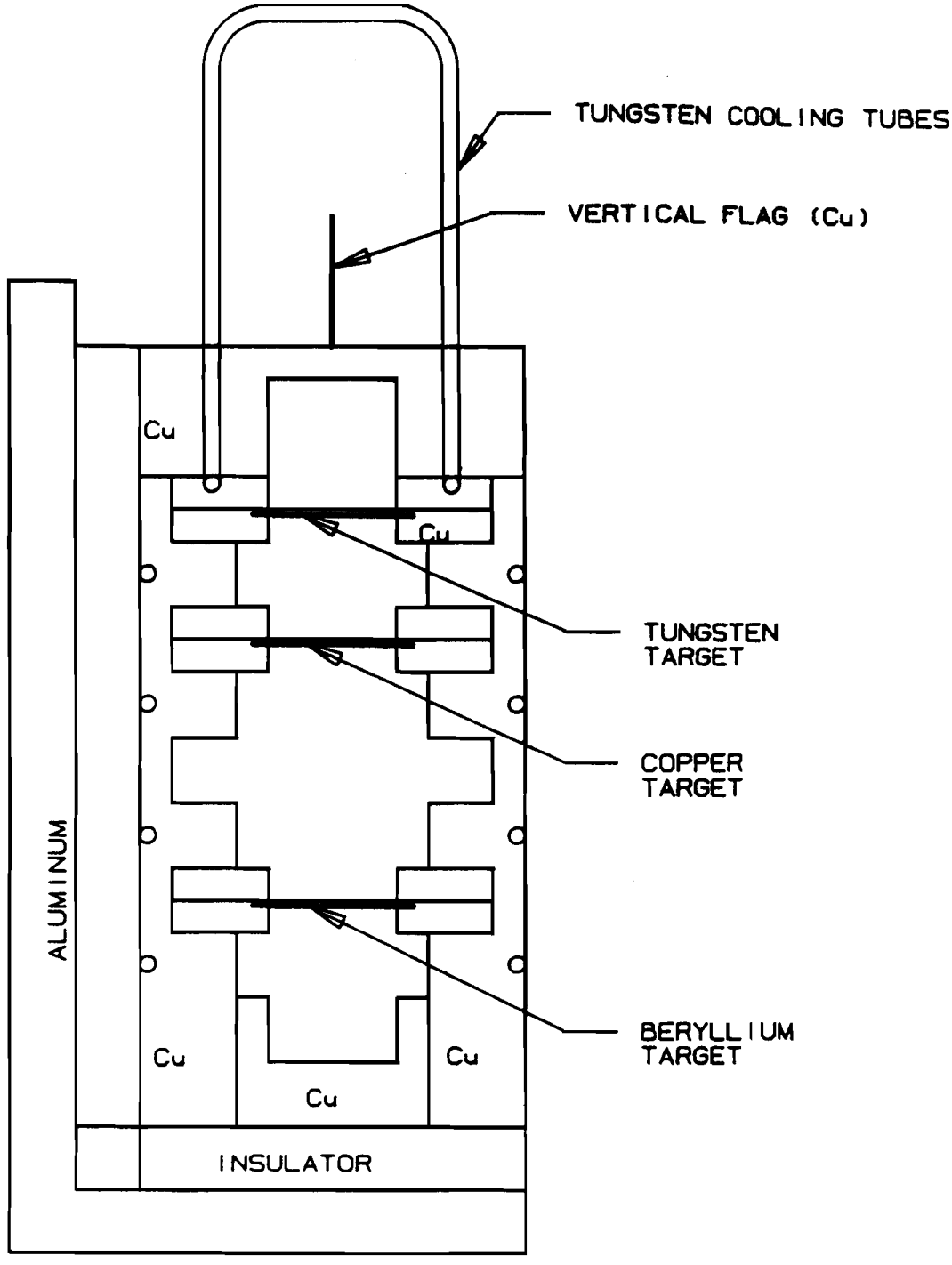
TUNGSTEN COOLING TUBES
VERTICAL FLAG (Cu)
Cu
Cu
TUNGSTEN TARGET
COPPER TARGET
BERYLLIUM TARGET
ALUMINUM
Cu
Cu
Cu
INSULATOR

Figure 5

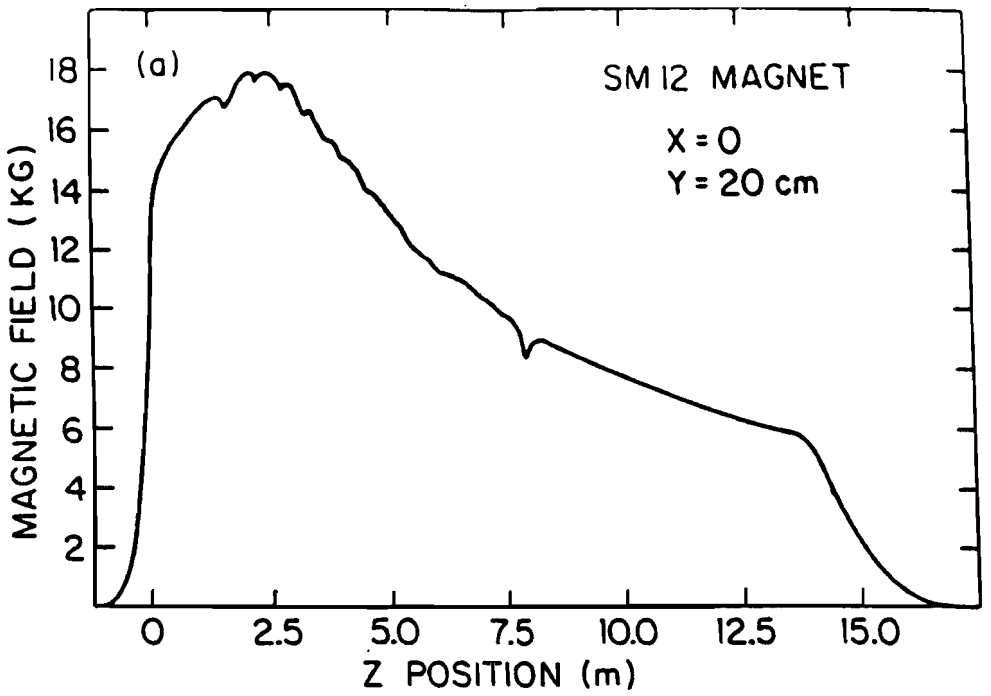
(a)
SM 12 MAGNET
X = 0
Y = 20 cm
MAGNETIC FIELD (KG)
18
16
14
12
10
8
6
4
2
0
2.5
5.0
7.5
10.0
12.5
15.0
Z POSITION (m)

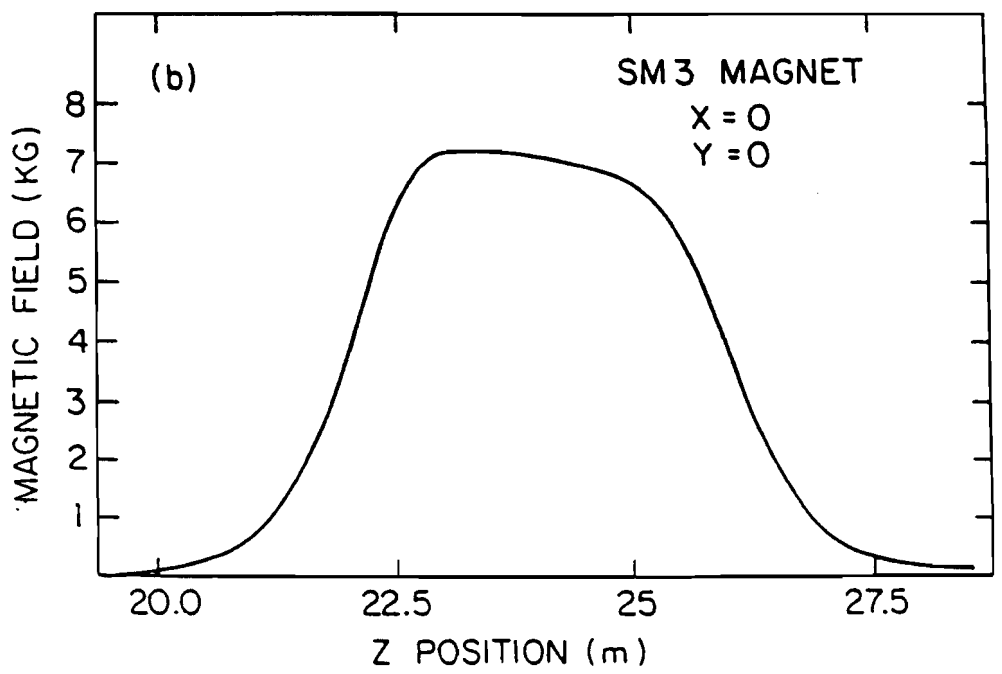
(b)
SM 3 MAGNET
X = 0
Y = 0
MAGNETIC FIELD (KG)
8
7
6
5
4
3
2
1
20.0
22.5
25
27.5
Z POSITION (m)

Figure 6

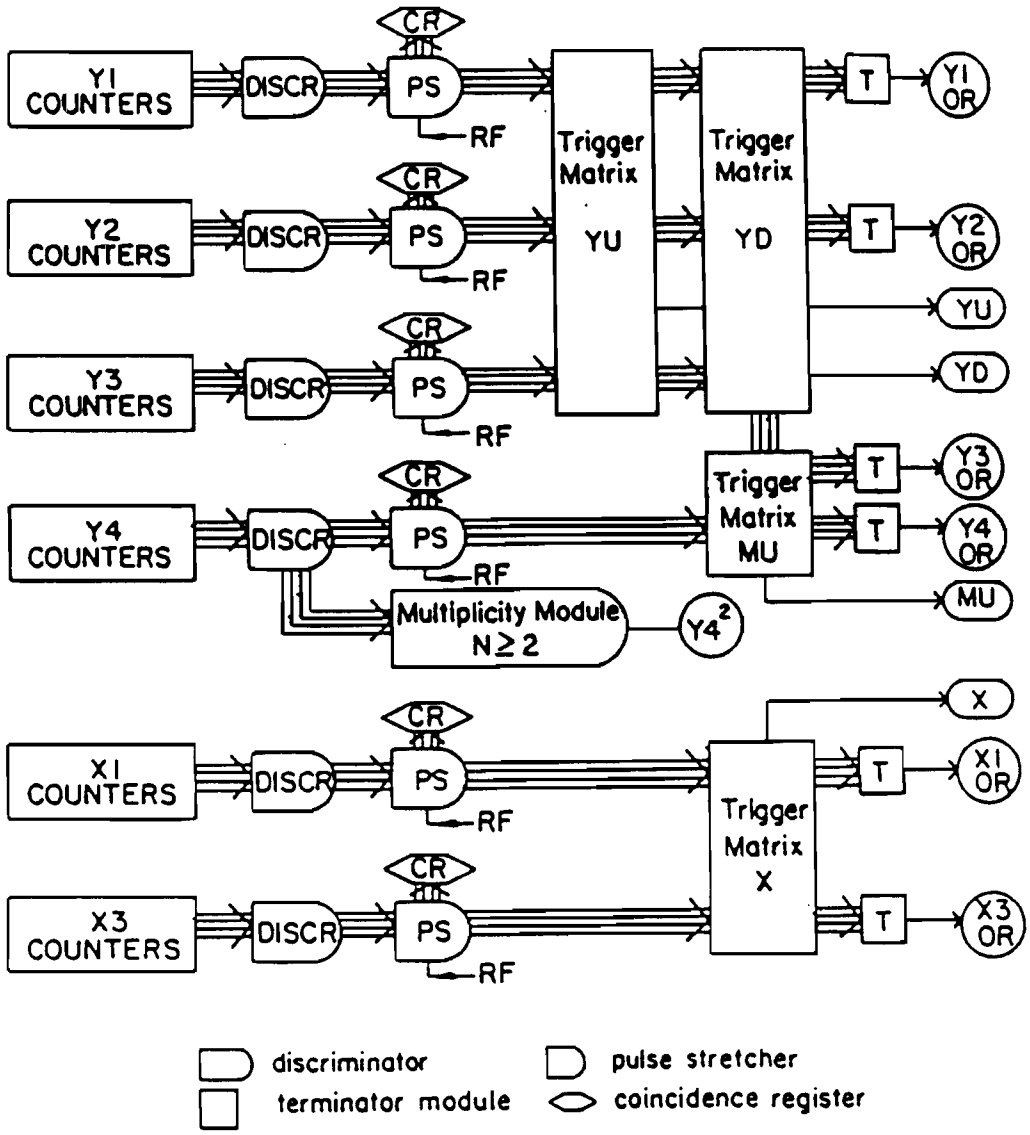
Y1 COUNTERS
Y2 COUNTERS
Y3 COUNTERS
Y4 COUNTERS
X1 COUNTERS
X3 COUNTERS
DISCR
CR
PS
RF
Trigger Matrix YU
Trigger Matrix YD
Trigger Matrix MU
Trigger Matrix X
T
Y1 OR
Y2 OR
Y3 OR
Y4 OR
X1 OR
X3 OR
YU
YD
MU
X
Multiplicity Module N≥2
Y4²
discriminator
terminator module
pulse stretcher
coincidence register

Figure 7 a)

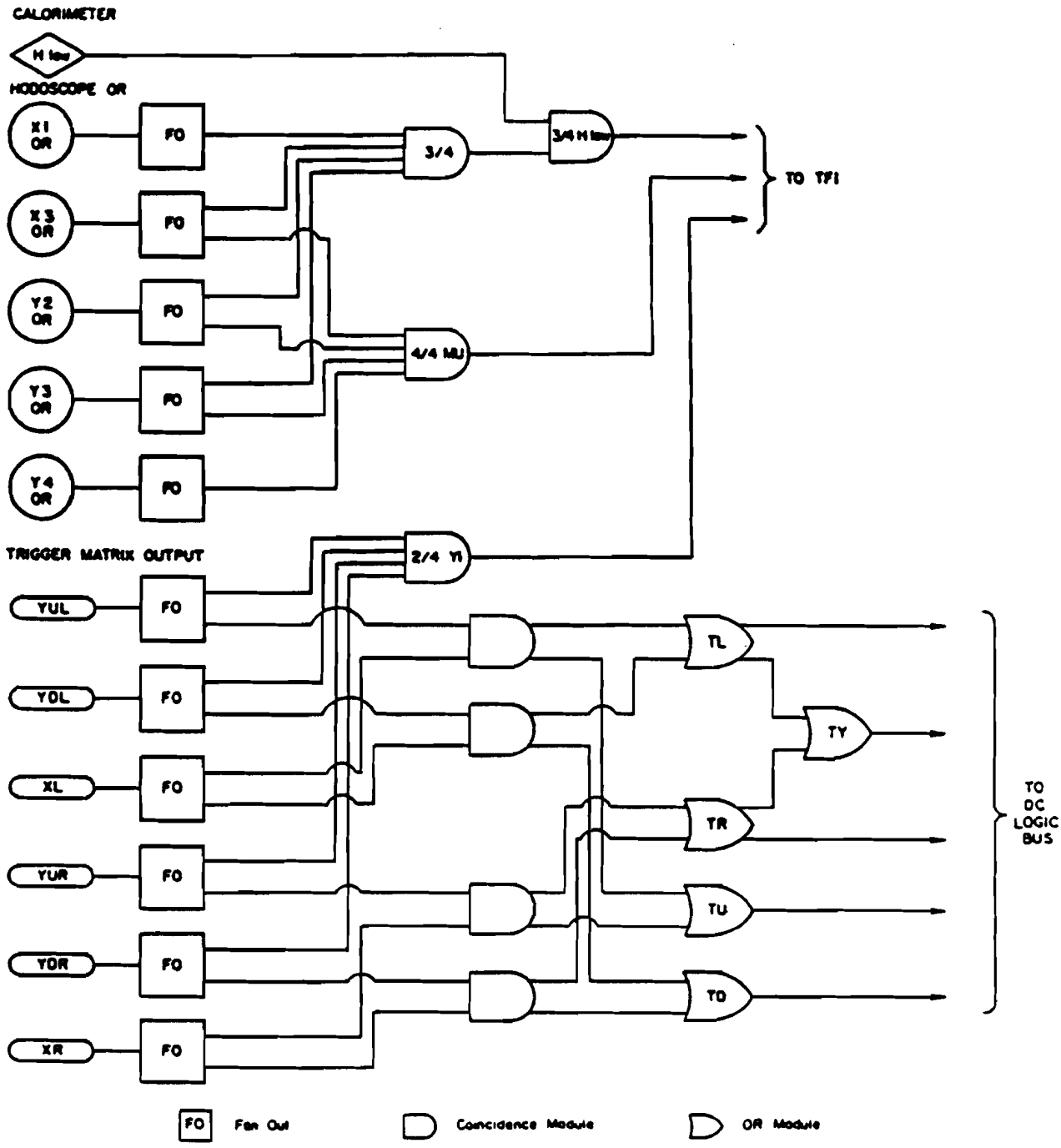
CALORIMETER
H low
HODOSCOPE OR
X1 OR
X3 OR
Y2 OR
Y3 OR
Y4 OR
FO
3/4
3/4 H low
4/4 MU
TO TFI
TRIGGER MATRIX OUTPUT
2/4 Y1
YUL
YOL
XL
YUR
YOR
XR
TL
TY
TR
TU
TD
TO DC LOGIC BUS
FO Fan Out
Coincidence Module
OR Module

Figure 7 b)

Pulse Stretcher Timing Diagram

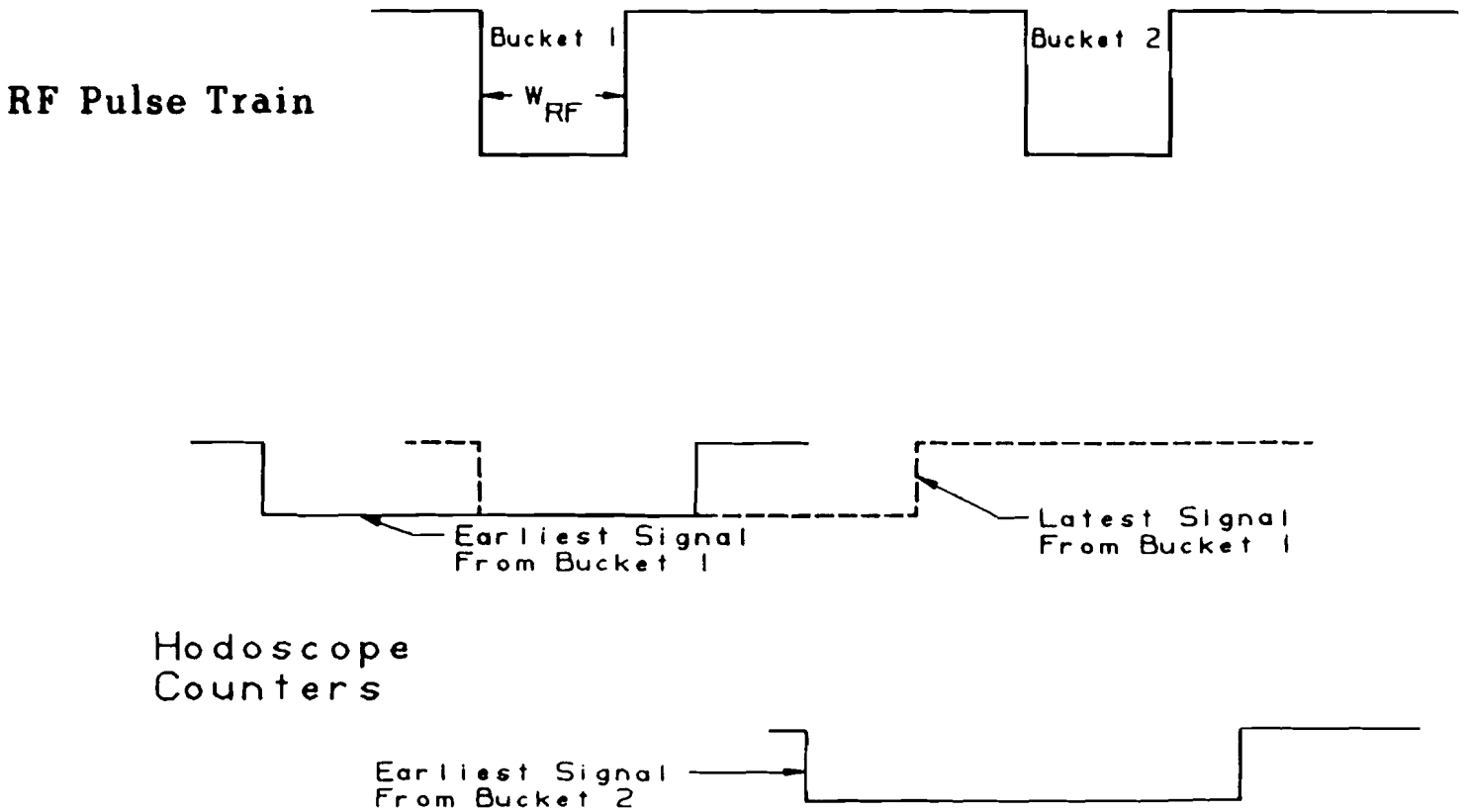

Figure 8

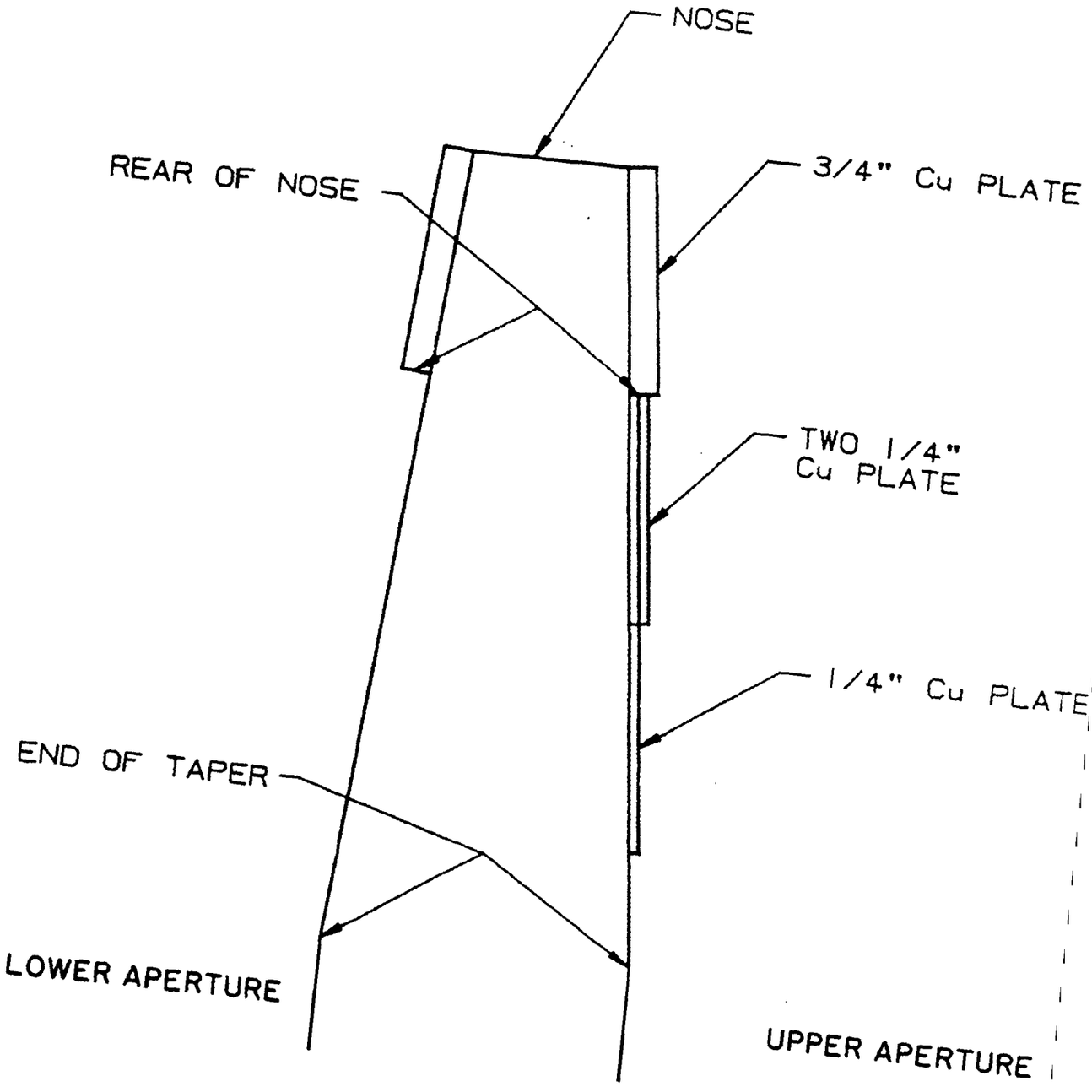
NOSE
REAR OF NOSE
3/4" Cu PLATE
TWO 1/4"
Cu PLATE
1/4" Cu PLATE
END OF TAPER
LOWER APERTURE
UPPER APERTURE

Figure 9

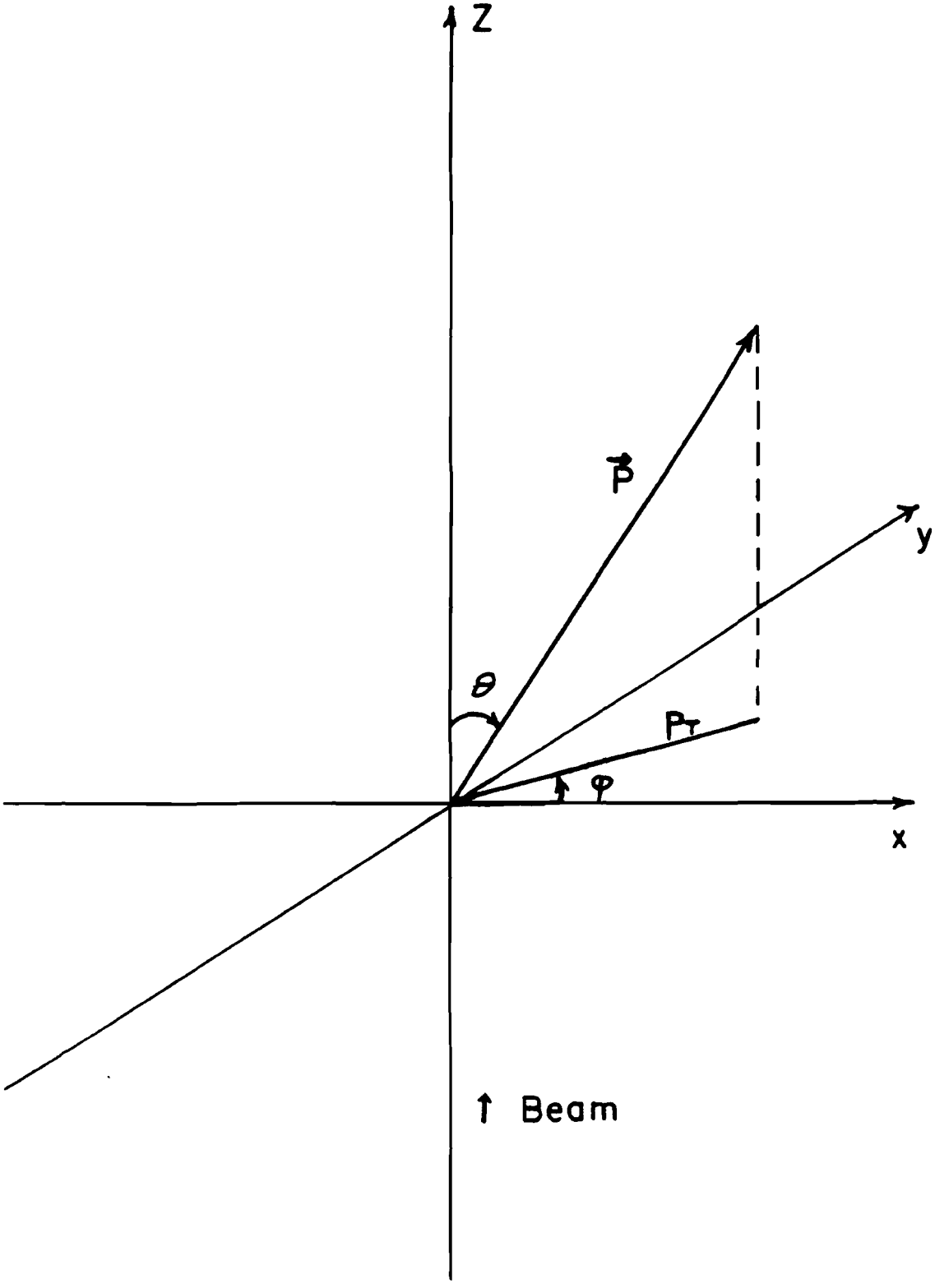

Figure 10

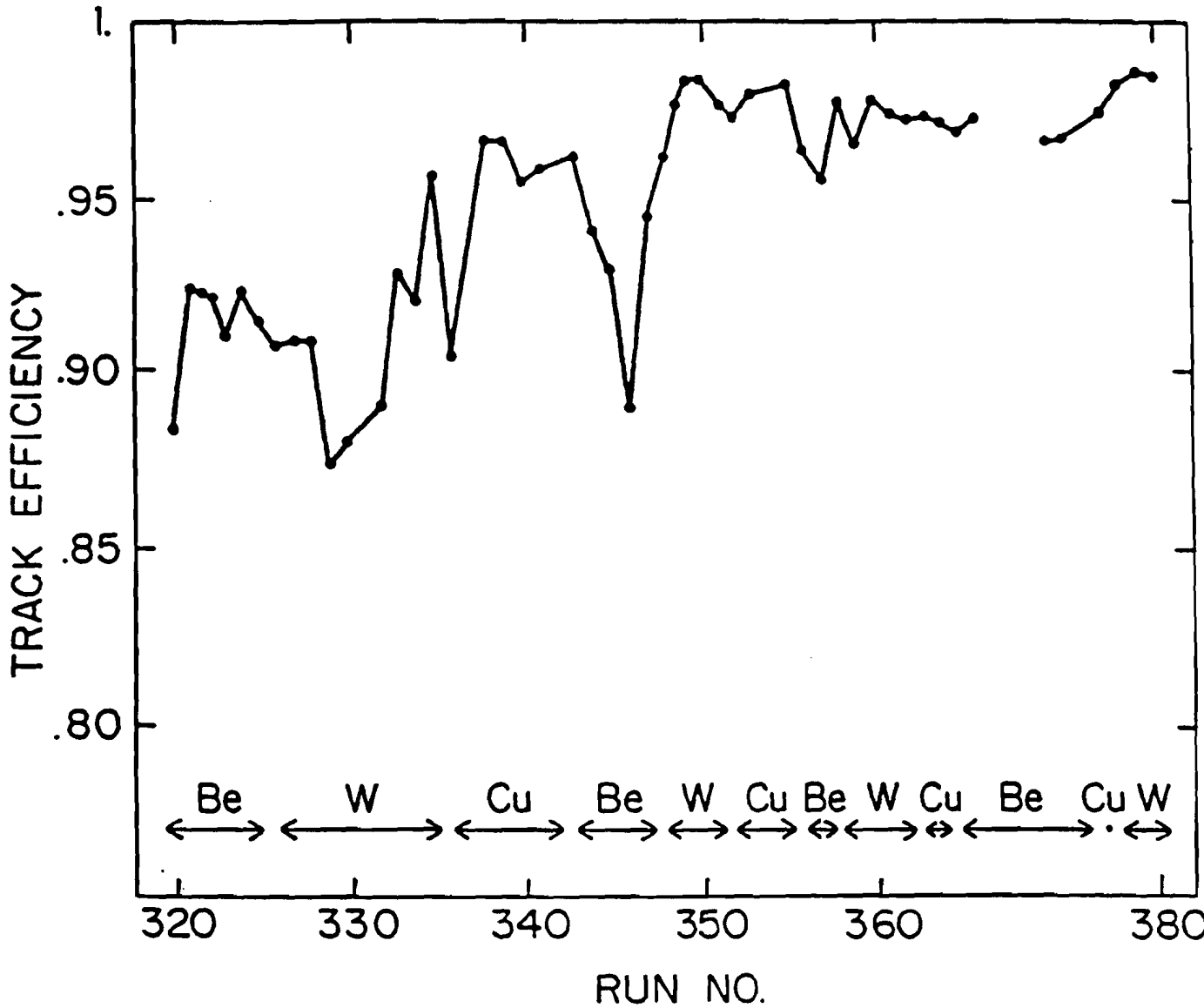
1.
.95
.90
.85
.80
TRACK EFFICIENCY
Be
W
Cu
Be
W
Cu
Be
W
Cu
Be
Cu
W
320
330
340
350
360
380
RUN NO.

Figure 11

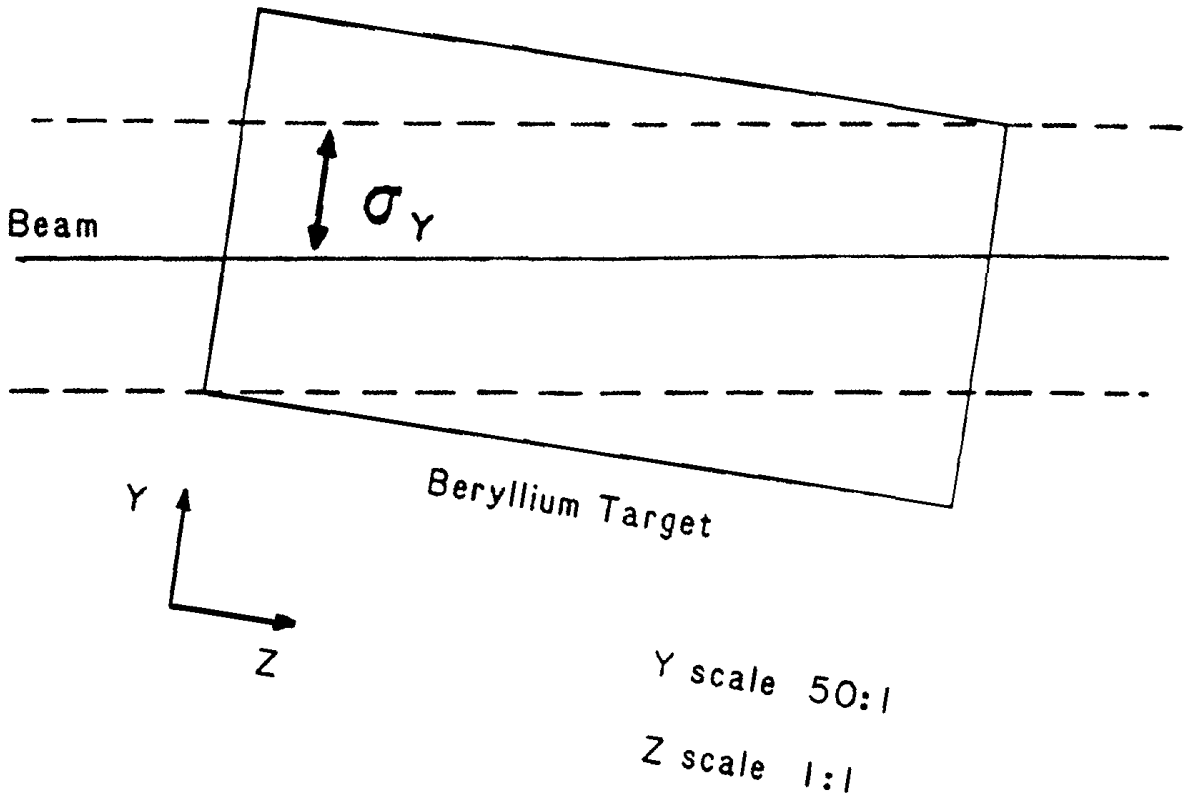

Figure 12

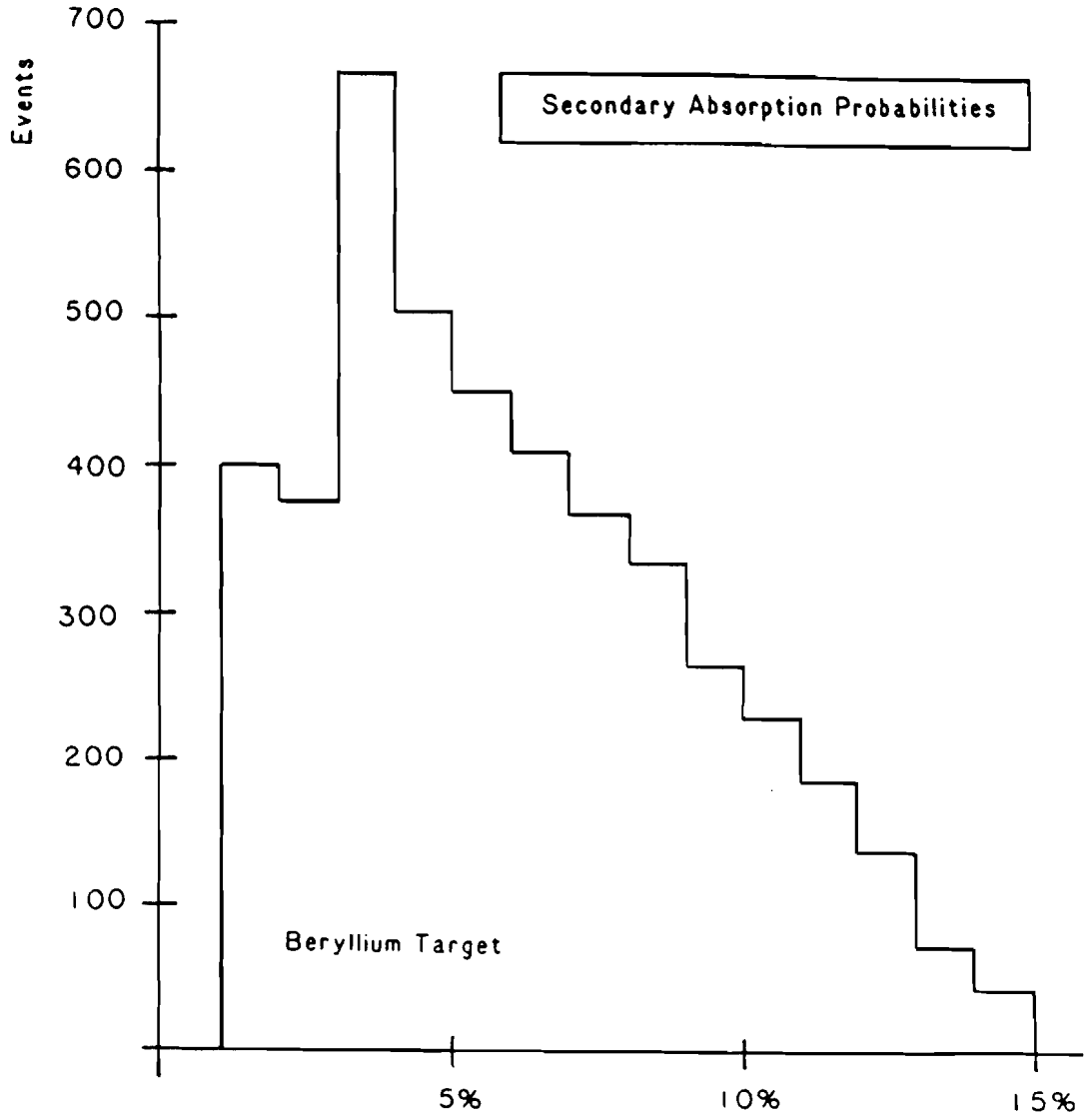
Secondary Absorption Probabilities
Events
700
600
500
400
300
200
100
Beryllium Target
5%
10%
15%

Figure 13

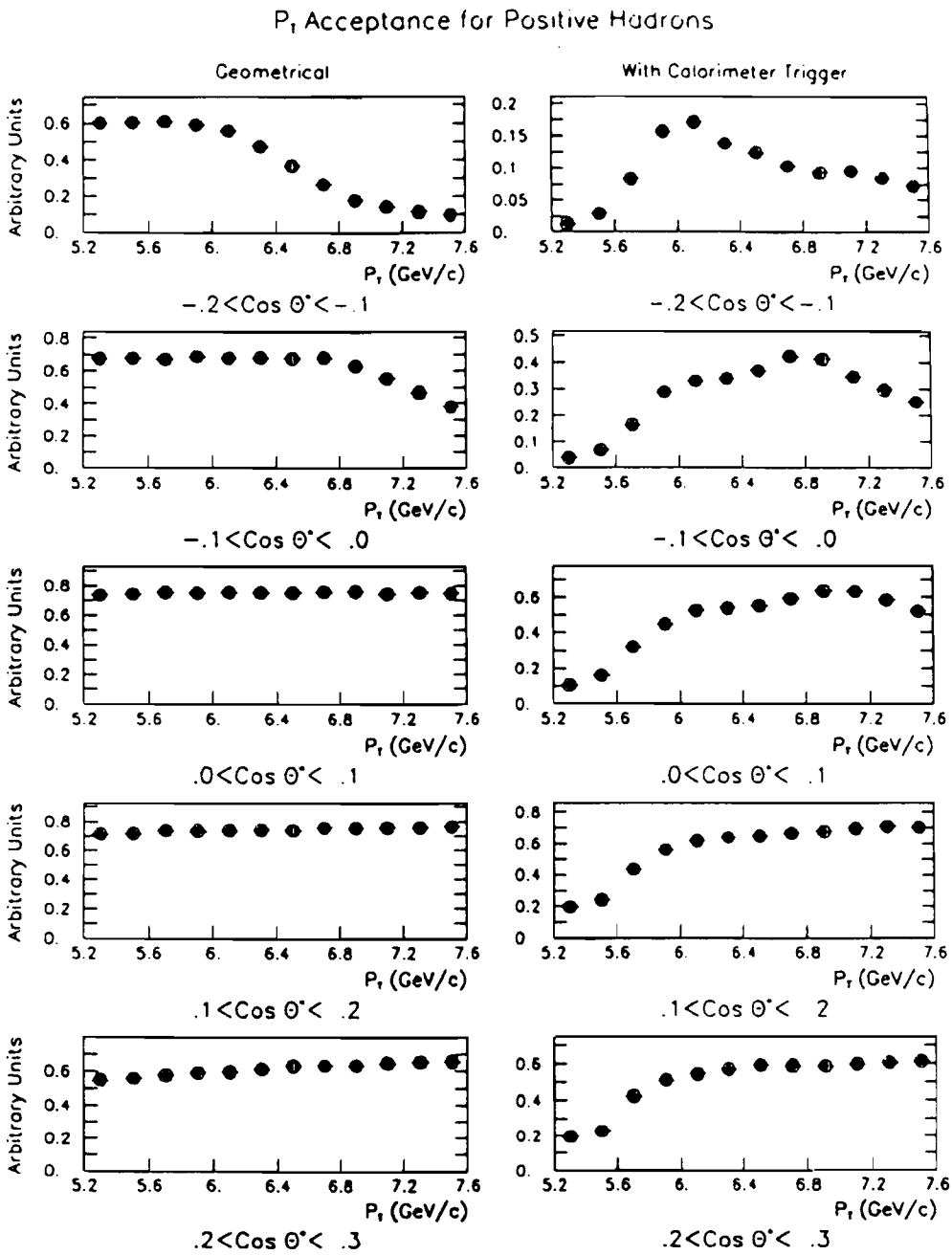
P_T Acceptance for Positive Hadrons
Geometrical
With Calorimeter Trigger
Arbitrary Units
P_T (GeV/c)
-.2<Cos Θ*<-.1
-.1<Cos Θ*< .0
.0<Cos Θ*< .1
.1<Cos Θ*< .2
.2<Cos Θ*< .3

Figure 14

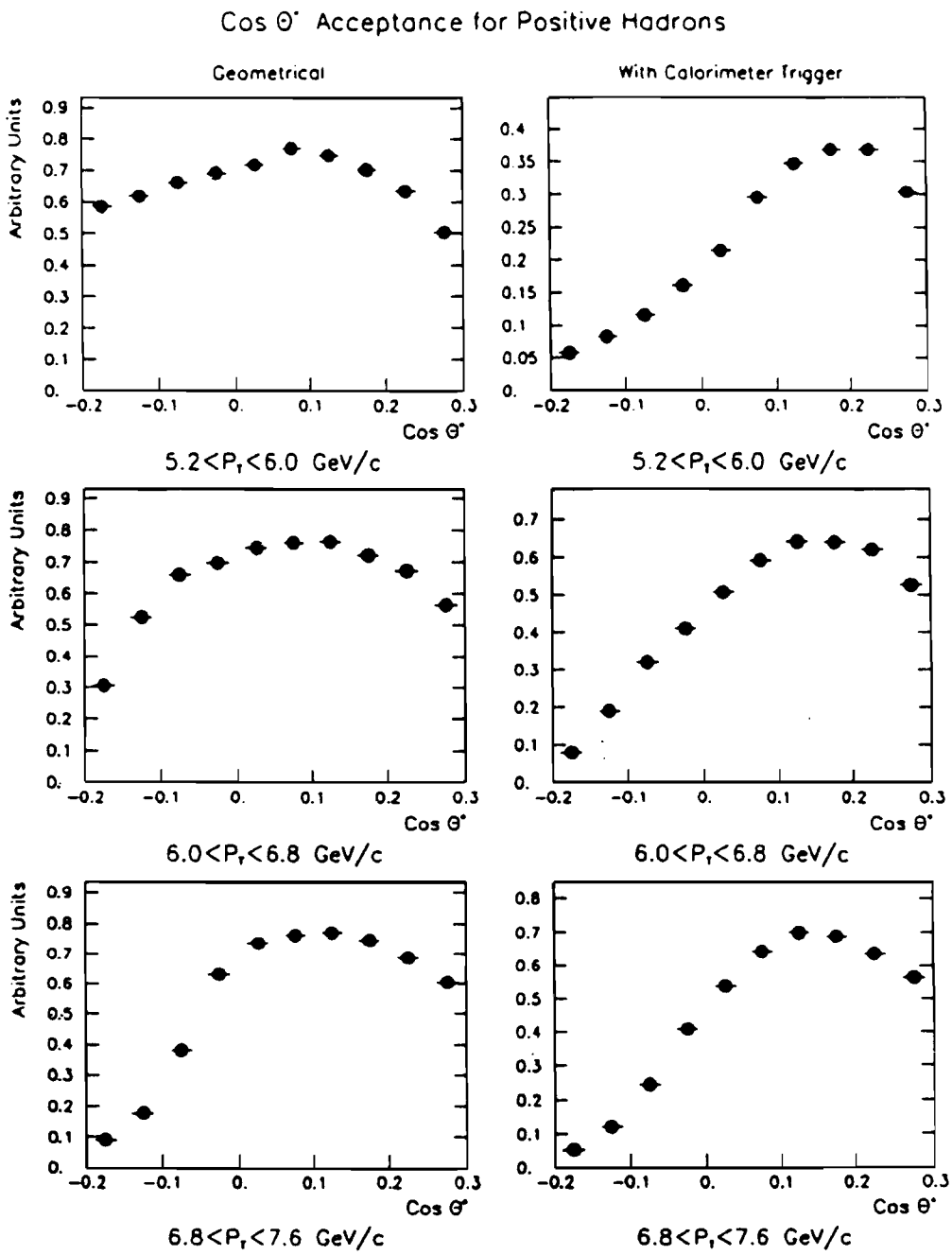
Cos Θ* Acceptance for Positive Hadrons
Geometrical
With Calorimeter Trigger
Arbitrary Units
Cos Θ*
5.2<P_T<6.0 GeV/c
6.0<P_T<6.8 GeV/c
6.8<P_T<7.6 GeV/c

Figure 15

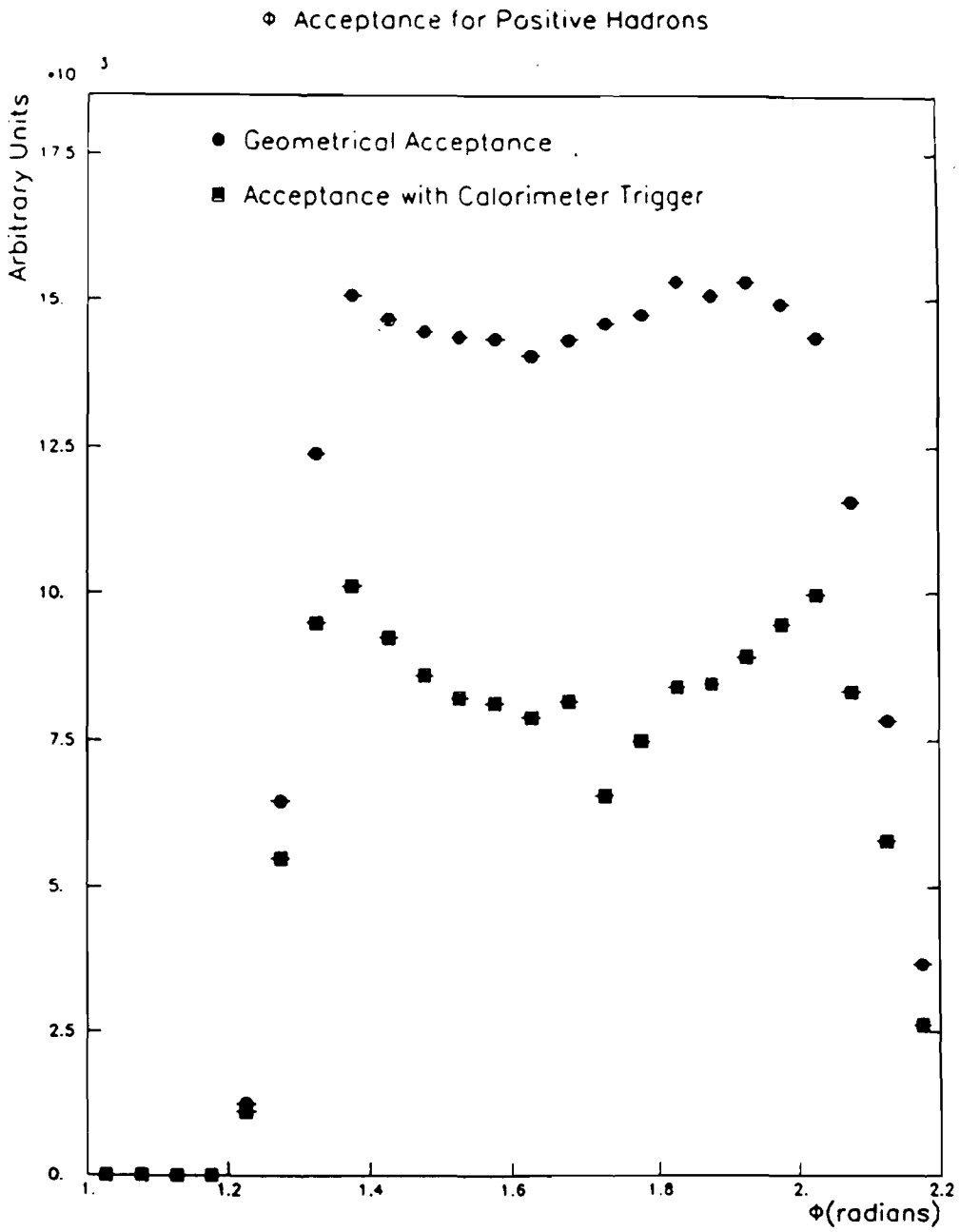
Φ Acceptance for Positive Hadrons
Geometrical Acceptance
Acceptance with Calorimeter Trigger
Arbitrary Units
•10 3
17.5
15.
12.5
10.
7.5
5.
2.5
0.
1.
1.2
1.4
1.6
1.8
2.
2.2
Φ(radians)

Figure 16

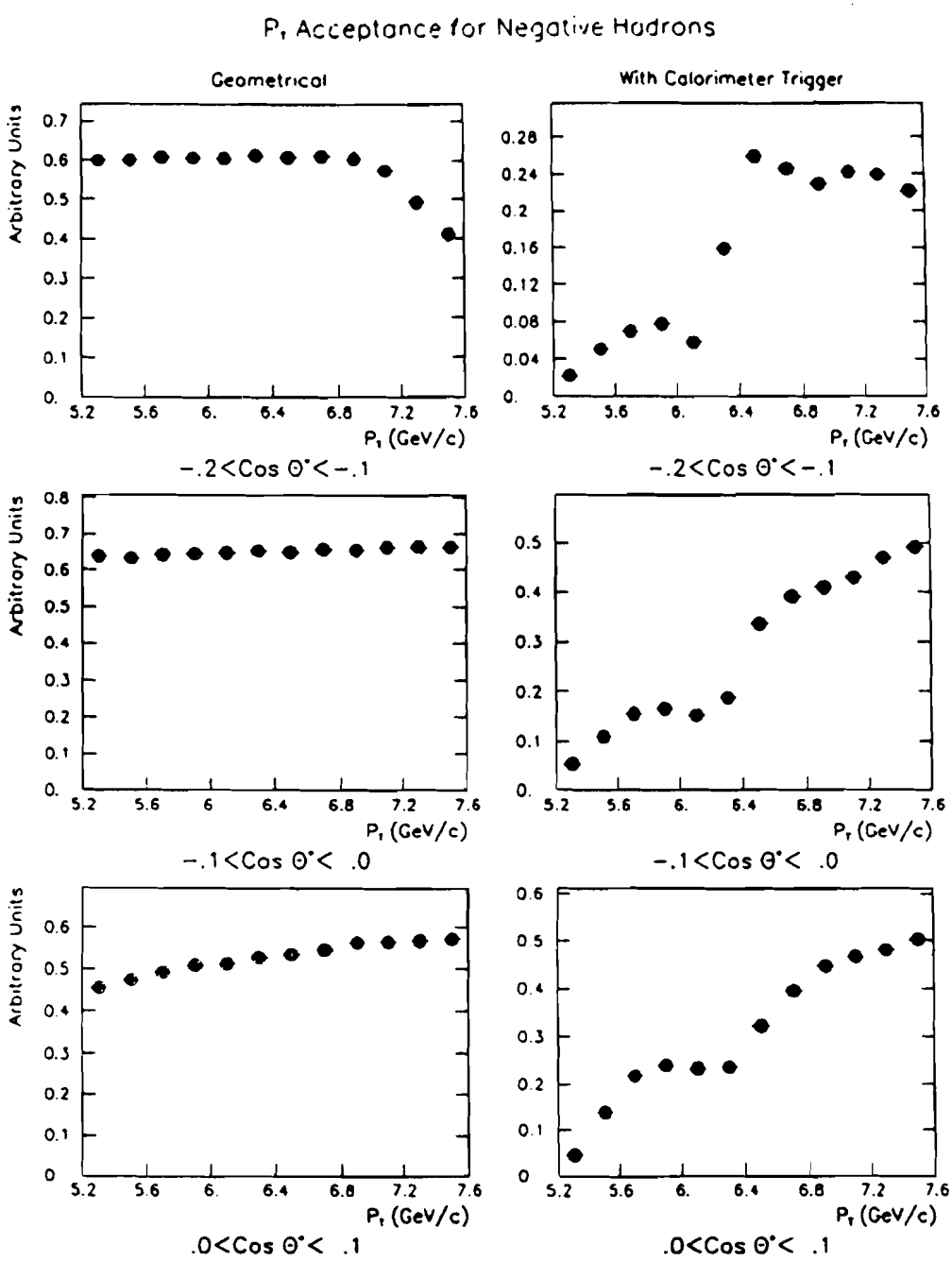
P_T Acceptance for Negative Hadrons
Geometrical
With Calorimeter Trigger
Arbitrary Units
P_T (GeV/c)
−.2<Cos Θ*<−.1
−.1<Cos Θ*< .0
.0<Cos Θ*< .1

Figure 17

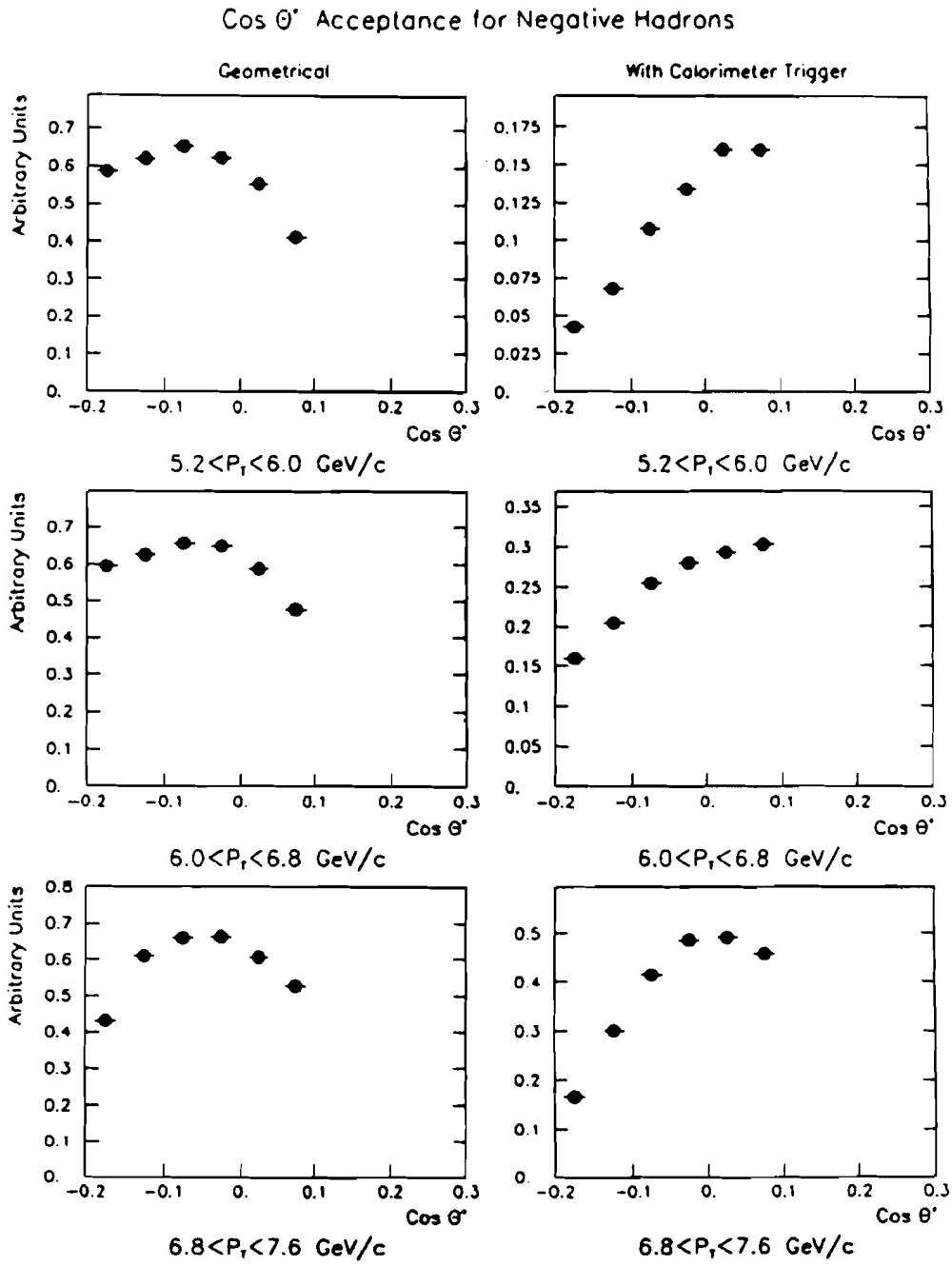
Cos Θ* Acceptance for Negative Hadrons
Geometrical
With Calorimeter Trigger
Arbitrary Units
Cos Θ*
5.2<P_T<6.0 GeV/c
5.2<P_T<6.0 GeV/c
6.0<P_T<6.8 GeV/c
6.0<P_T<6.8 GeV/c
6.8<P_T<7.6 GeV/c
6.8<P_T<7.6 GeV/c

Figure 18

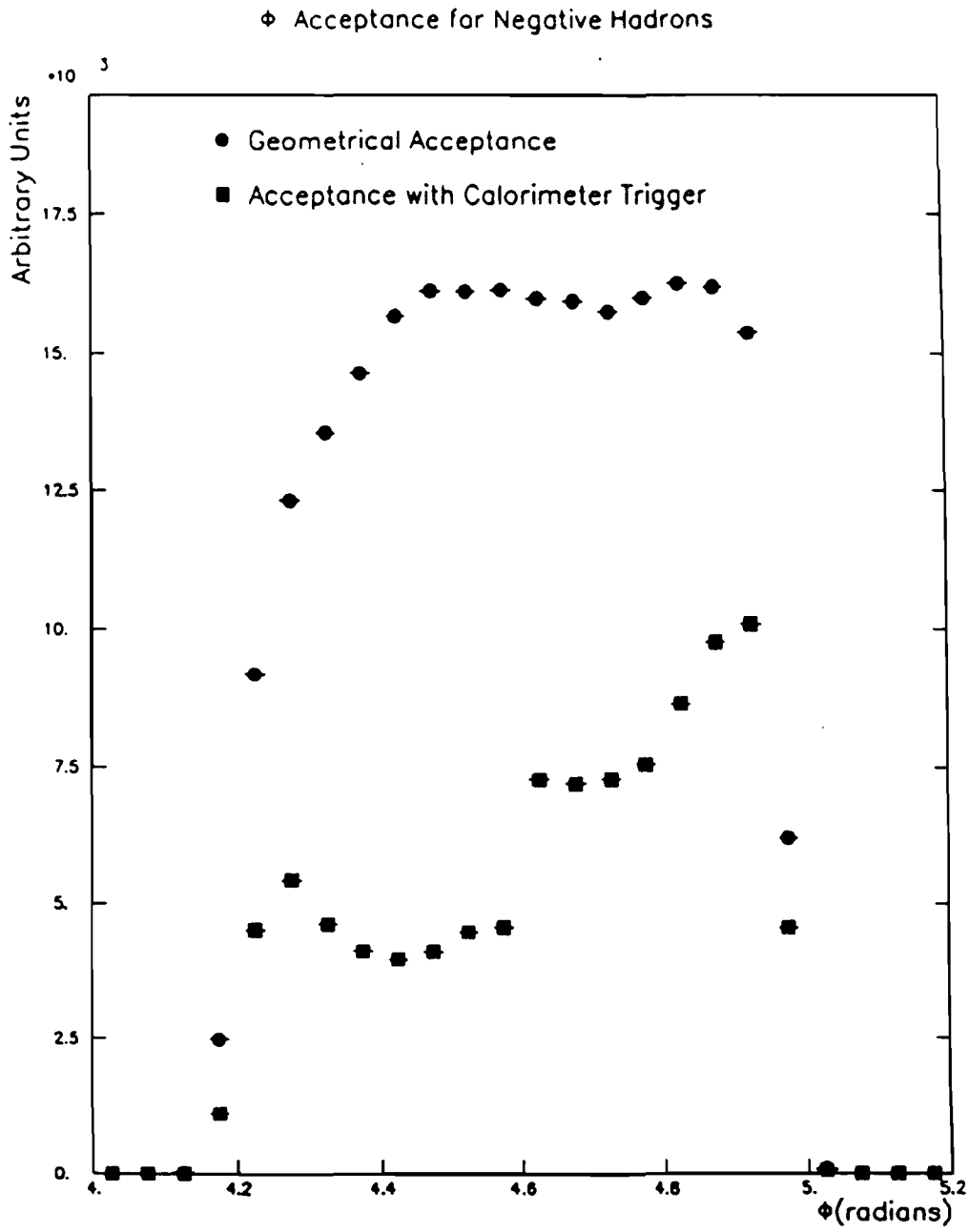
Φ Acceptance for Negative Hadrons
Geometrical Acceptance
Acceptance with Calorimeter Trigger
Arbitrary Units
•10 3
17.5
15.
12.5
10.
7.5
5.
2.5
0.
4.
4.2
4.4
4.6
4.8
5.
5.2
Φ(radians)

Figure 19

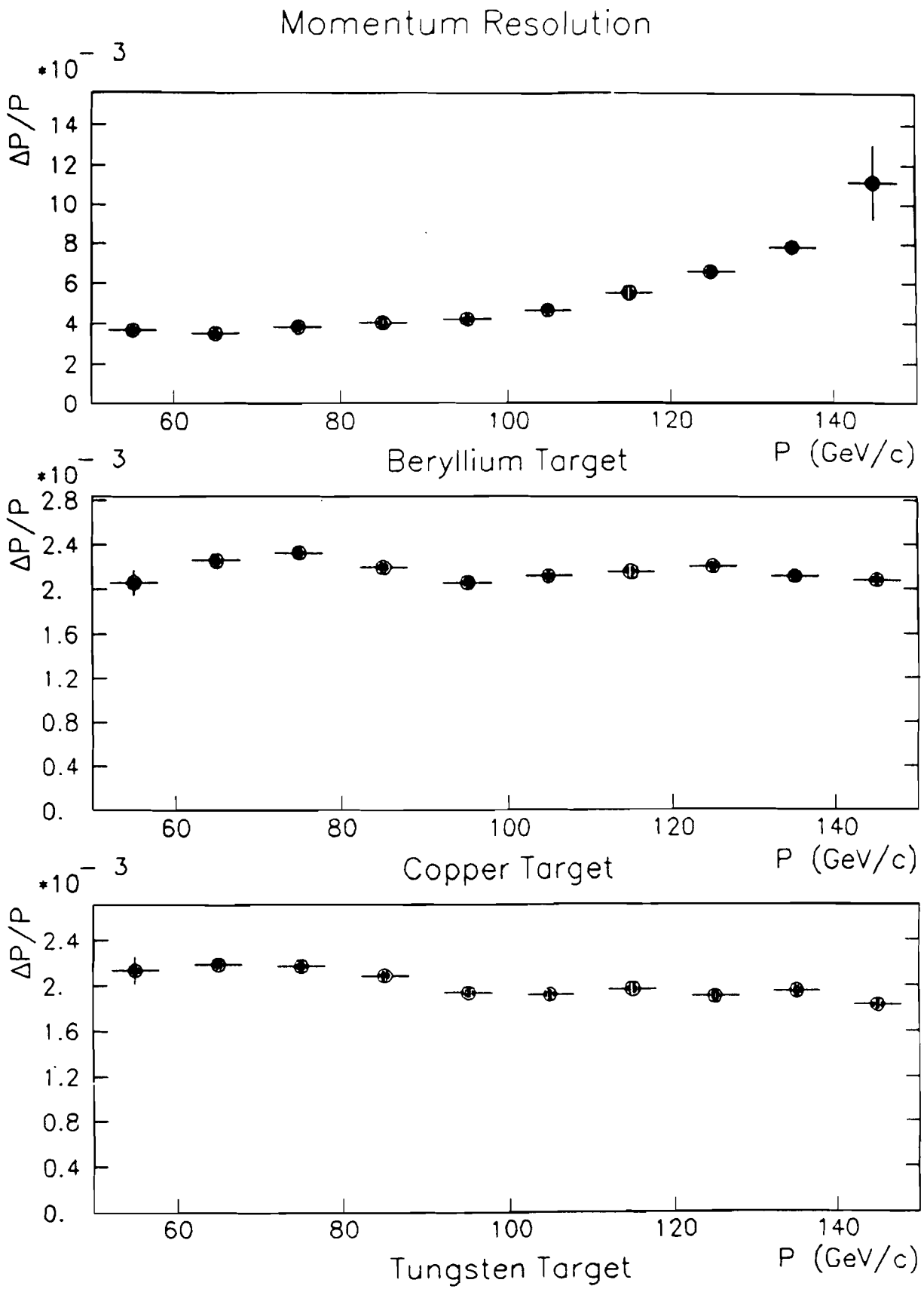
Momentum Resolution
*10^-3
ΔP/P
14
12
10
8
6
4
2
0
60
80
100
120
140
Beryllium Target
P (GeV/c)
*10^-3
ΔP/P
2.8
2.4
2.
1.6
1.2
0.8
0.4
0.
60
80
100
120
140
Copper Target
P (GeV/c)
*10^-3
ΔP/P
2.4
2.
1.6
1.2
0.8
0.4
0.
60
80
100
120
140
Tungsten Target
P (GeV/c)

Figure 20

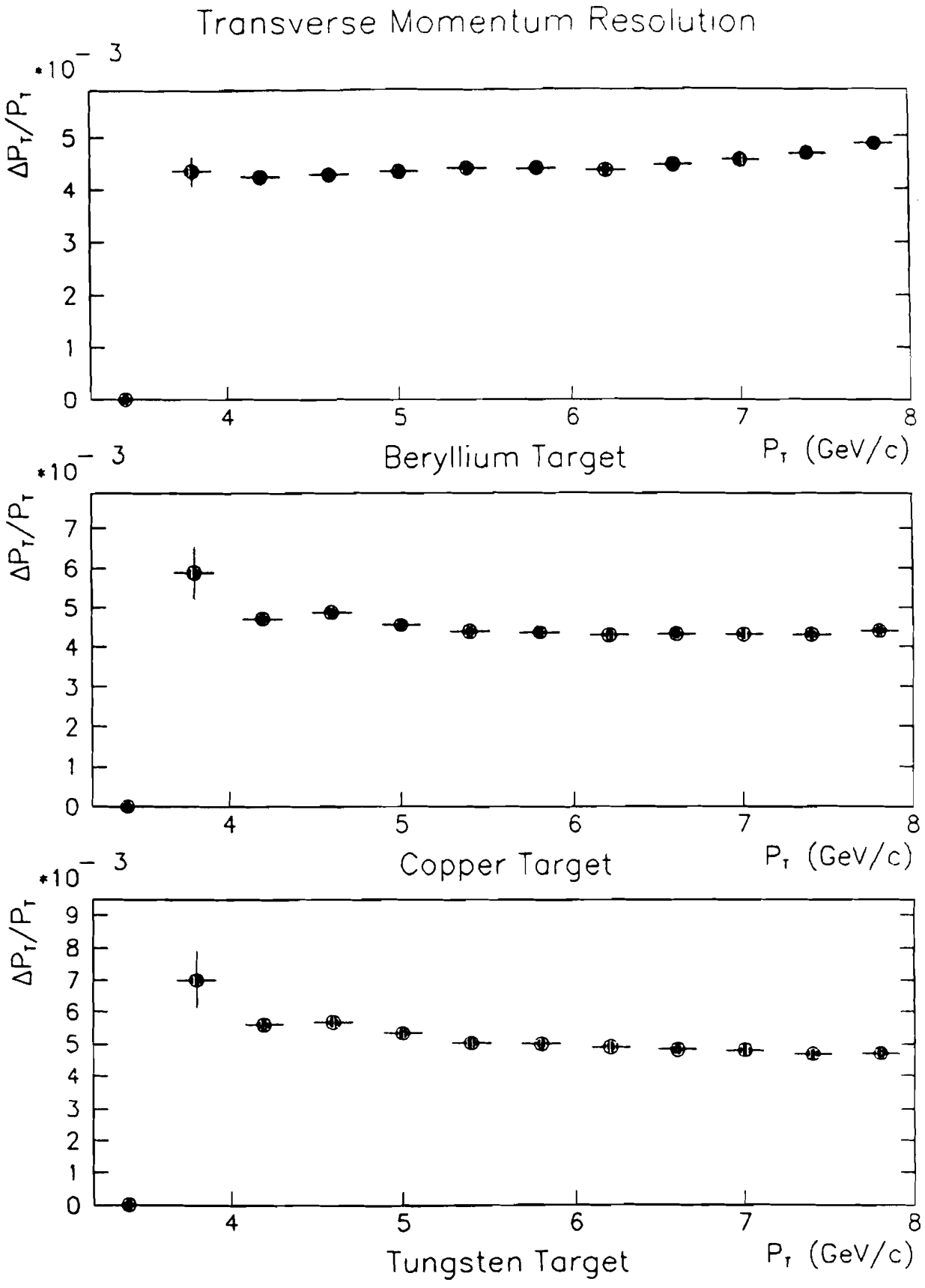
Transverse Momentum Resolution
$\Delta P_T/P_T$
$*10^{-3}$
Beryllium Target
P_T (GeV/c)
Copper Target
Tungsten Target

Figure 21

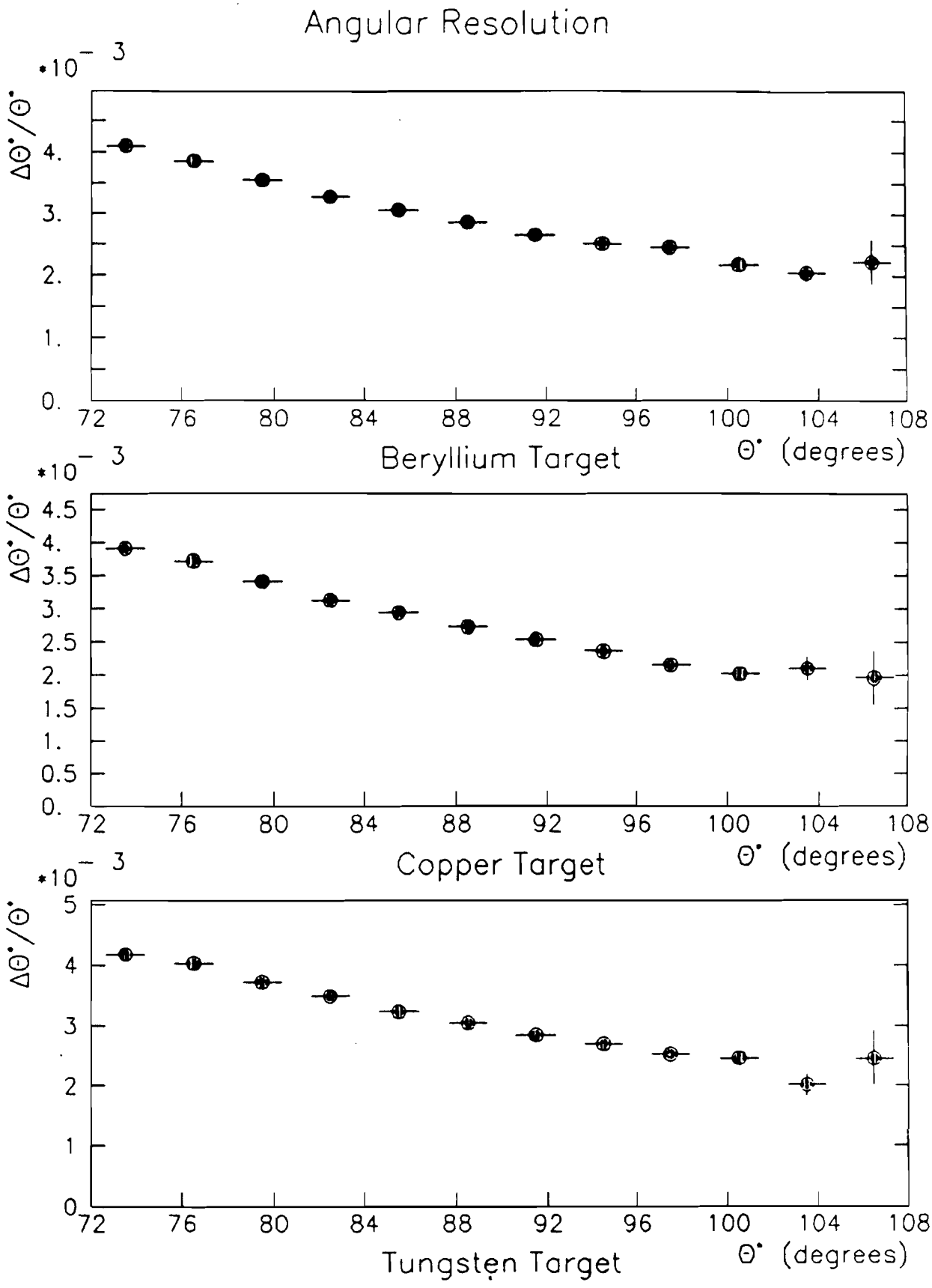
Angular Resolution
*10^-3
ΔΘ*/Θ*
4.
3.
2.
1.
0.
72
76
80
84
88
92
96
100
104
108
Beryllium Target
Θ* (degrees)
*10^-3
ΔΘ*/Θ*
4.5
4.
3.5
3.
2.5
2.
1.5
1.
0.5
0.
Copper Target
Θ* (degrees)
*10^-3
ΔΘ*/Θ*
5
4
3
2
1
0
Tungsten Target
Θ* (degrees)

Figure 22

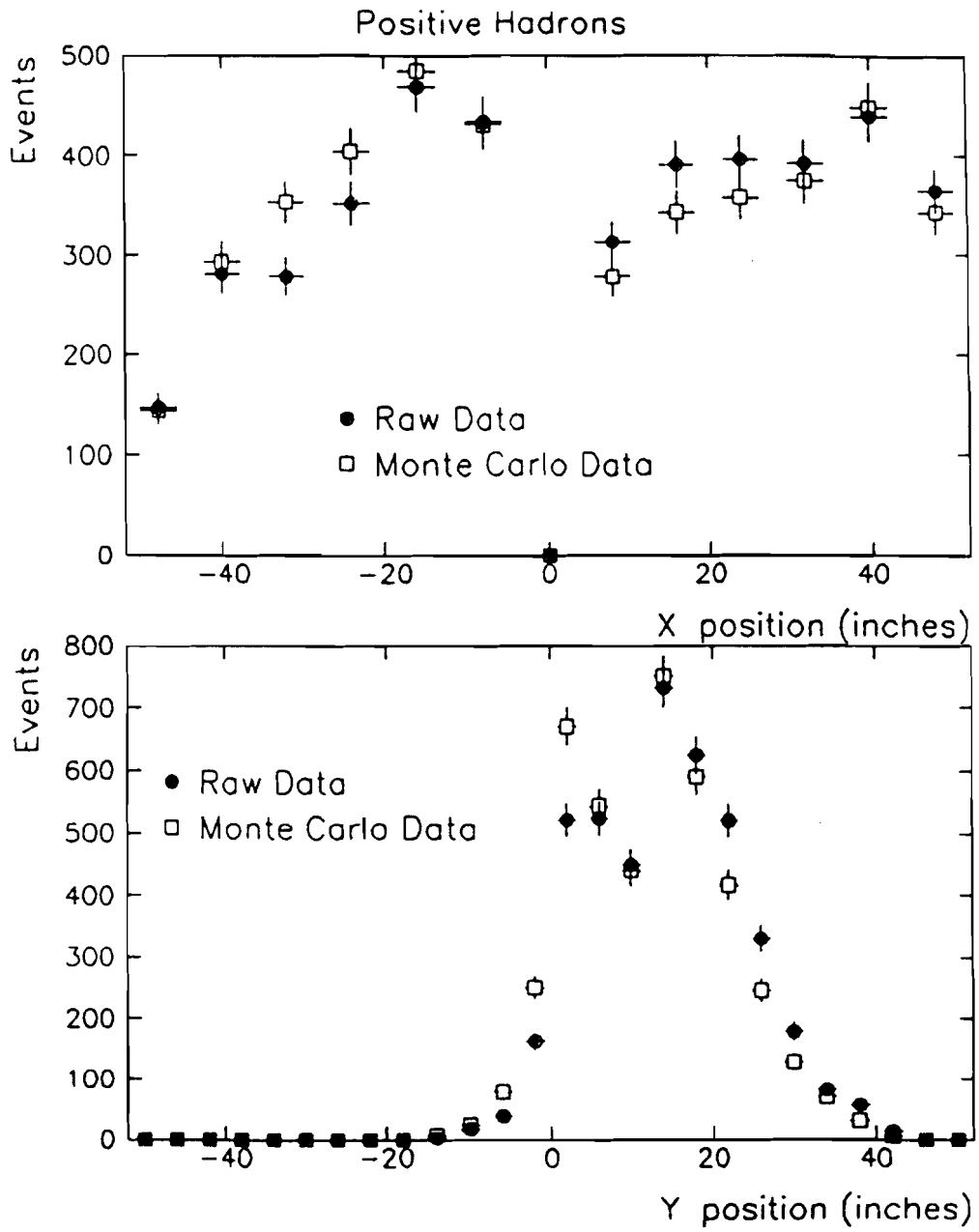
Positive Hadrons
Events
500
400
300
200
100
0
-40
-20
0
20
40
X position (inches)
Raw Data
Monte Carlo Data
Events
800
700
600
500
400
300
200
100
0
-40
-20
0
20
40
Y position (inches)
Raw Data
Monte Carlo Data

Figure 23

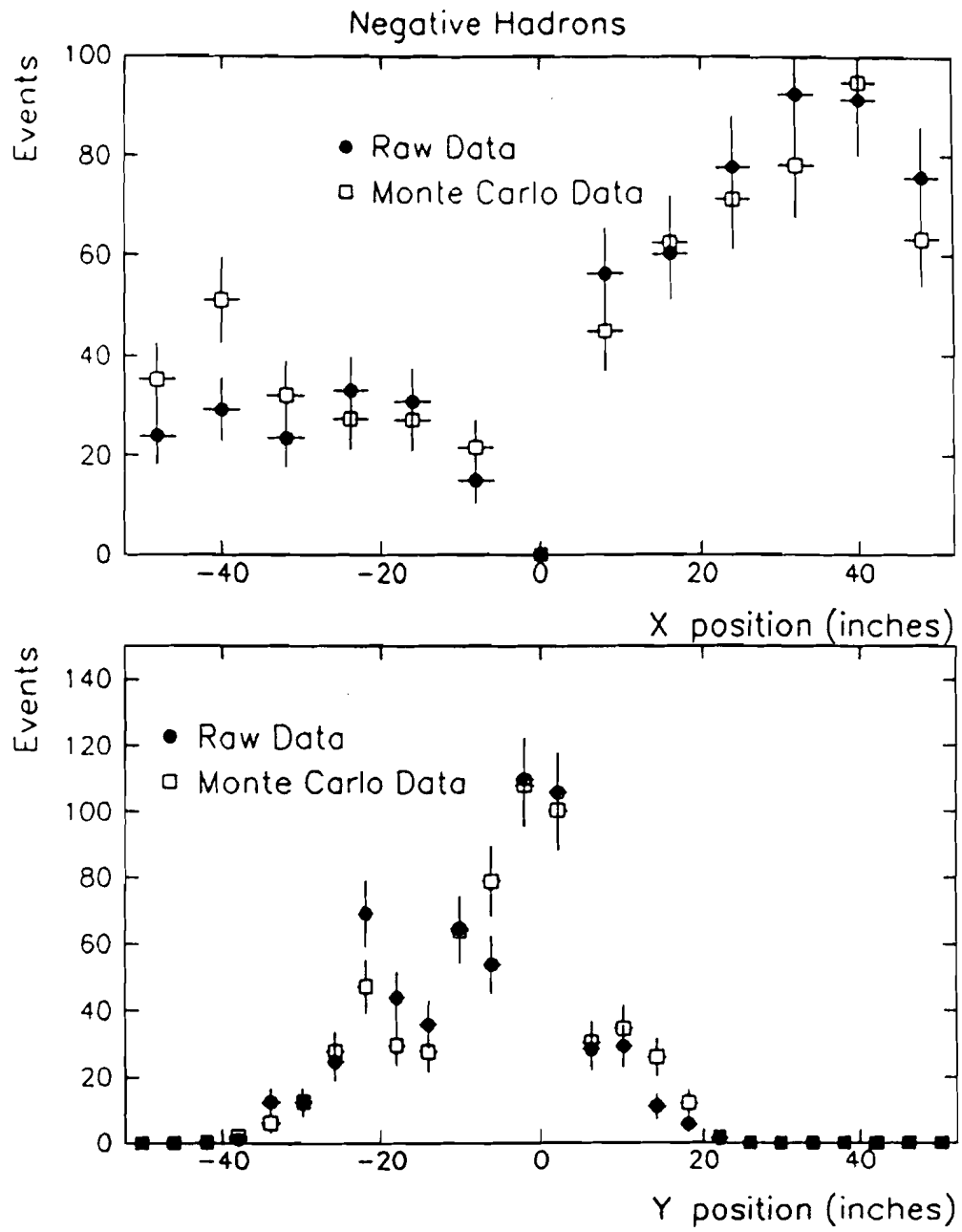
Negative Hadrons
Events
Raw Data
Monte Carlo Data
X position (inches)
Events
Raw Data
Monte Carlo Data
Y position (inches)

Figure 24

The Beryllium Correction Function for Positive Hadrons

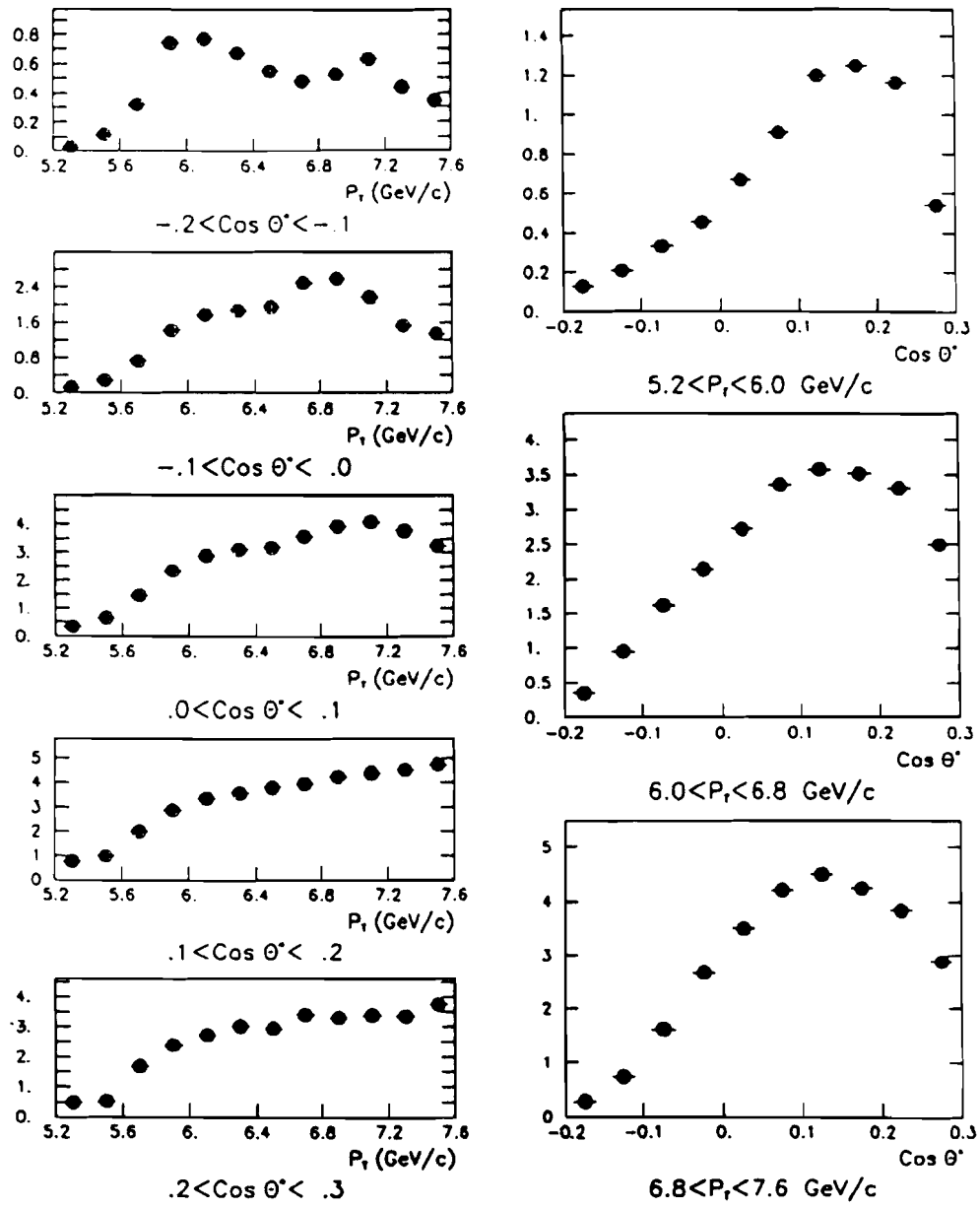

Figure 25

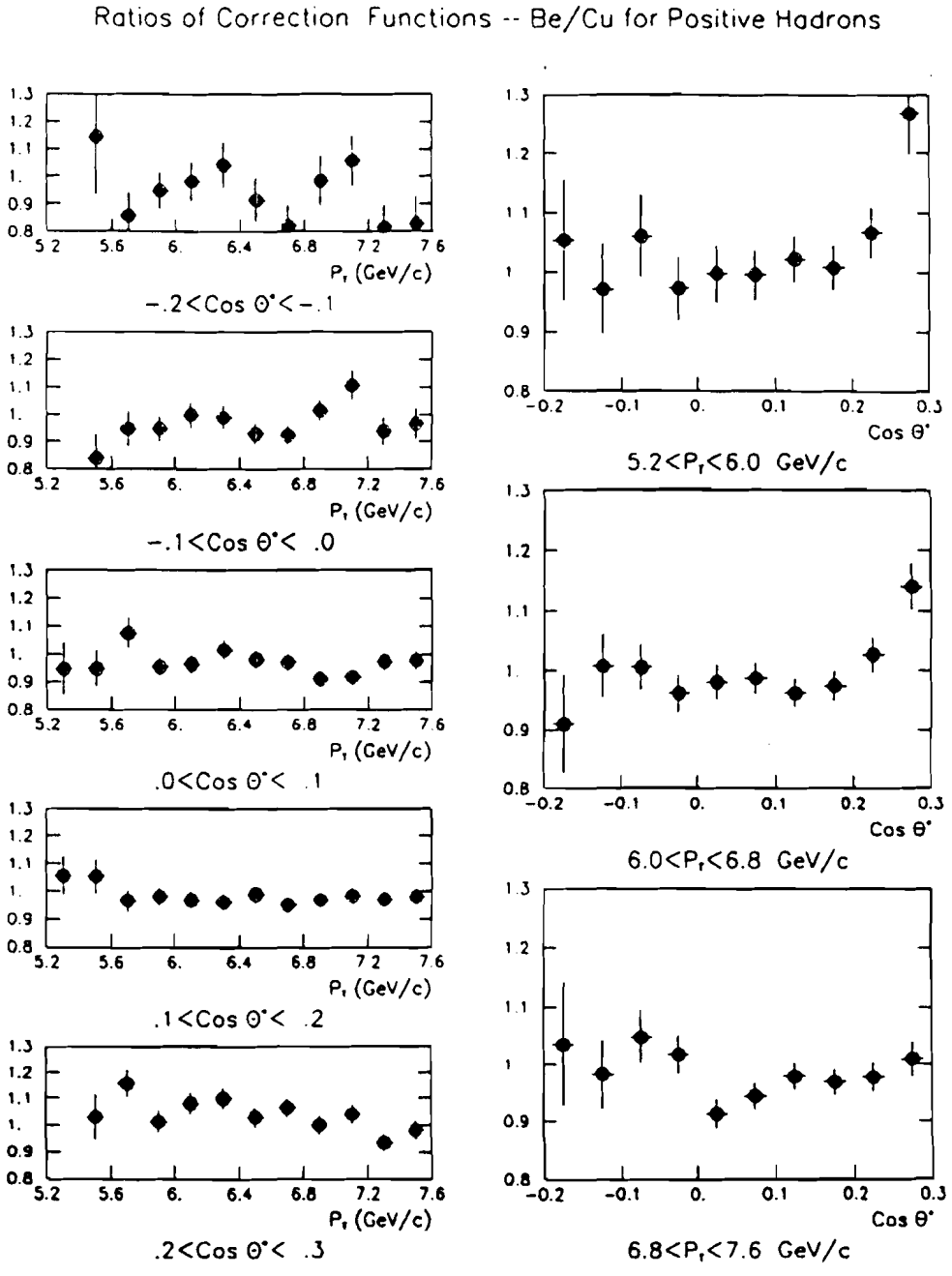
Ratios of Correction Functions -- Be/Cu for Positive Hadrons
P_T (GeV/c)
$-.2<\cos\Theta^*<-.1$
$-.1<\cos\Theta^*<.0$
$.0<\cos\Theta^*<.1$
$.1<\cos\Theta^*<.2$
$.2<\cos\Theta^*<.3$
Cos Θ^*
$5.2<P_T<6.0$ GeV/c
$6.0<P_T<6.8$ GeV/c
$6.8<P_T<7.6$ GeV/c

Figure 26

Ratios of Correction Functions -- Be/W for Positive Hadrons

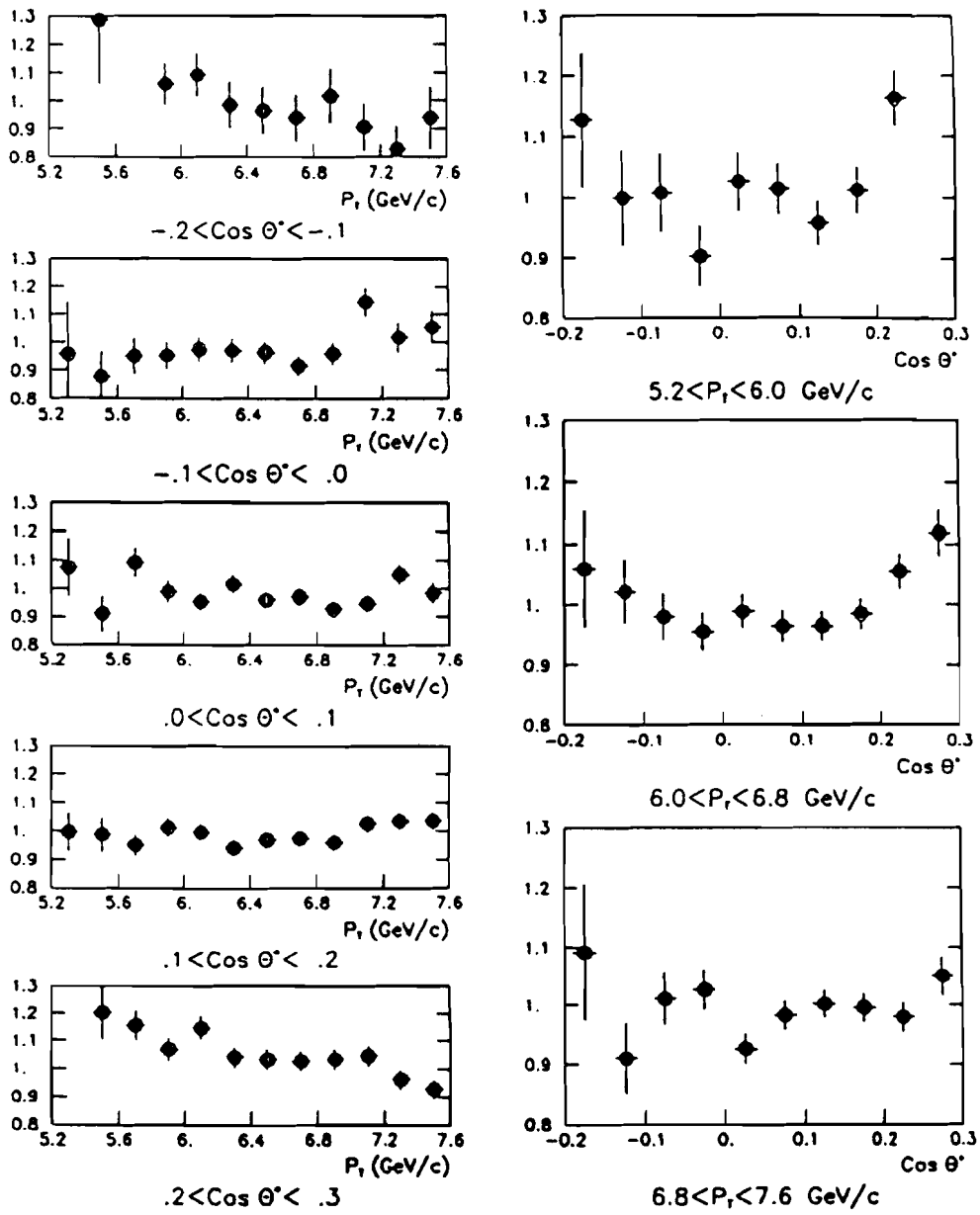

Figure 27

The Beryllium Correction Function for Negative Hadrons

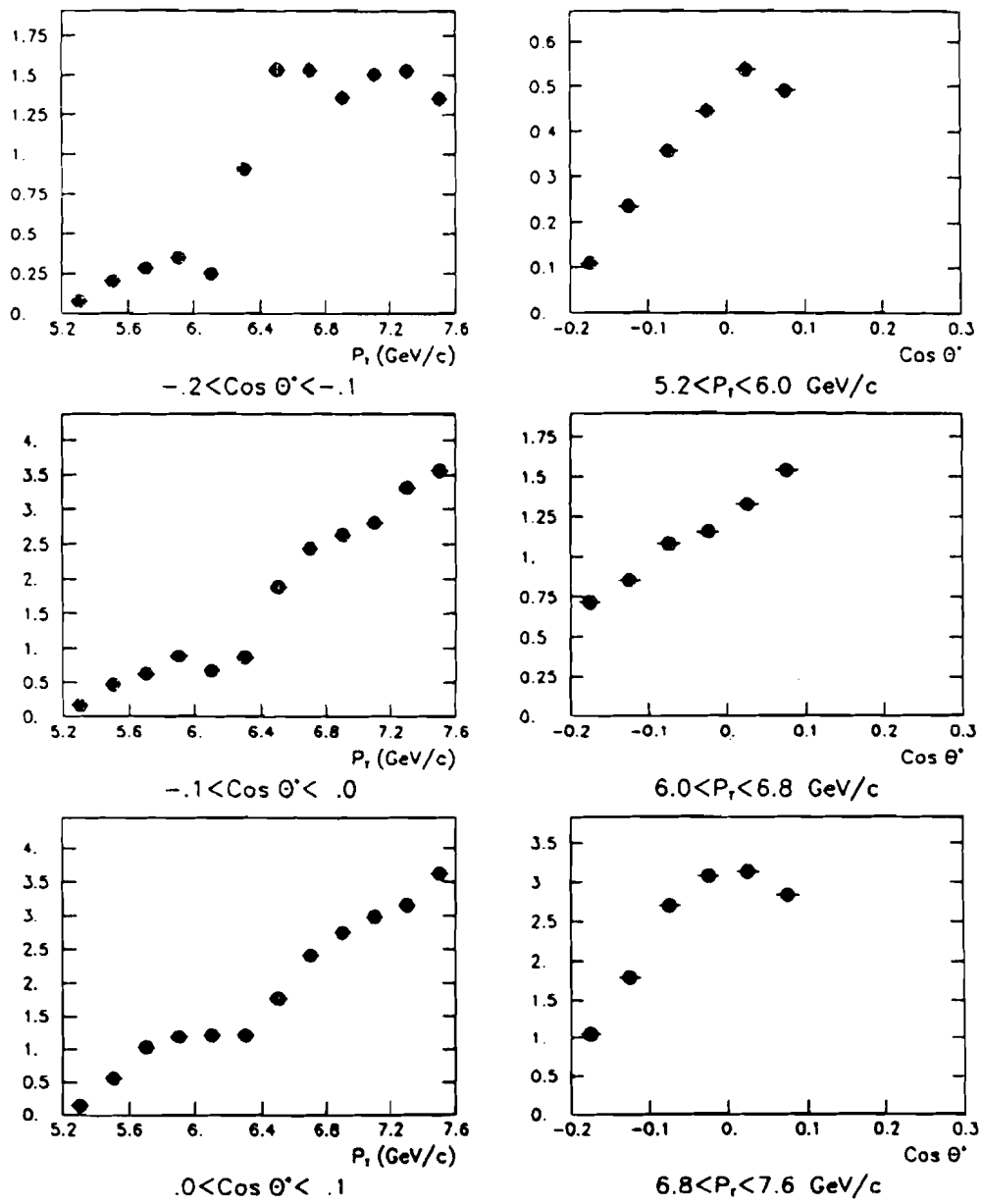

Figure 28

Ratios of Correction Functions -- Be/Cu for Negative Hadrons

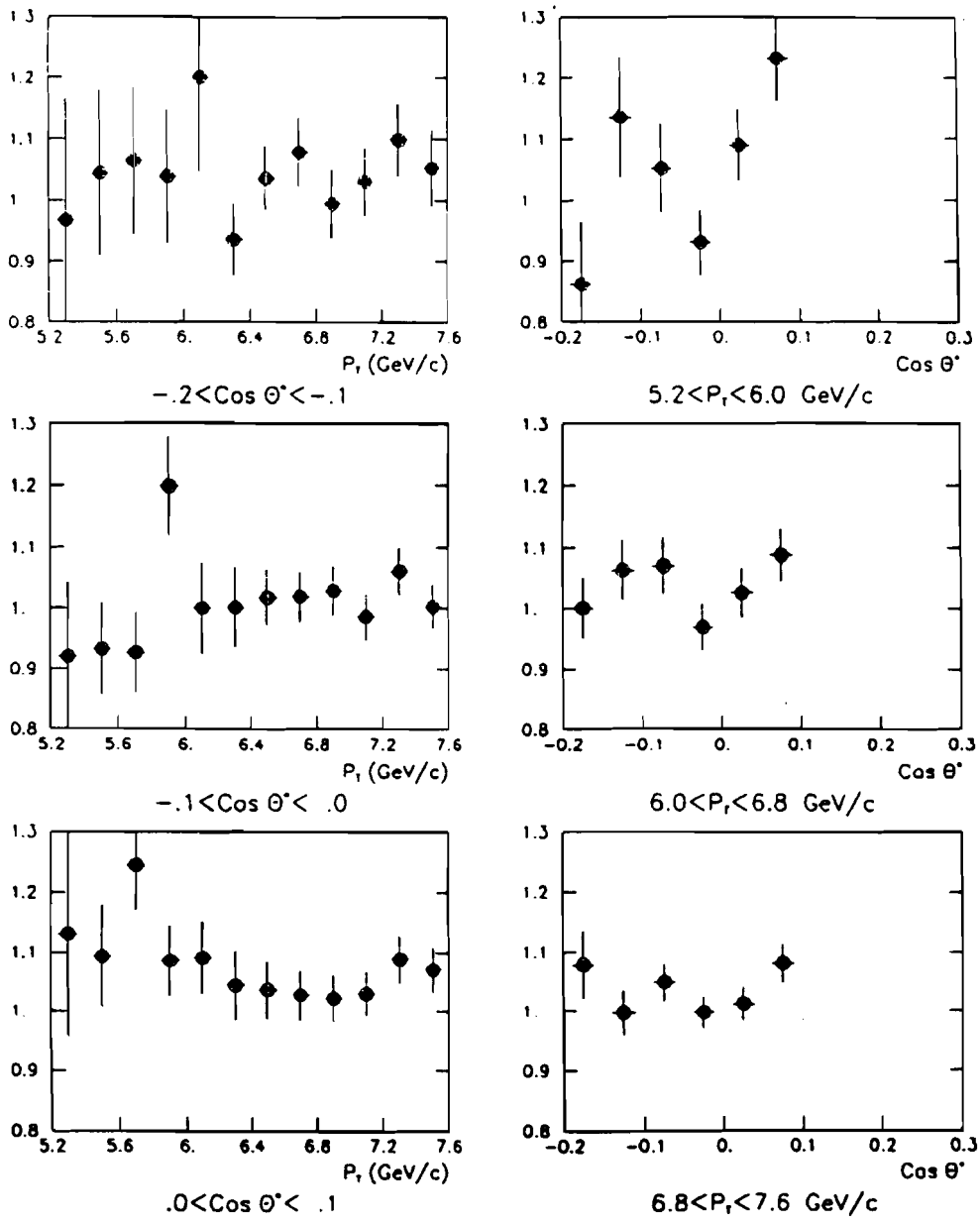

Figure 29

Ratios of Correction Functions -- Be/W for Negative Hadrons

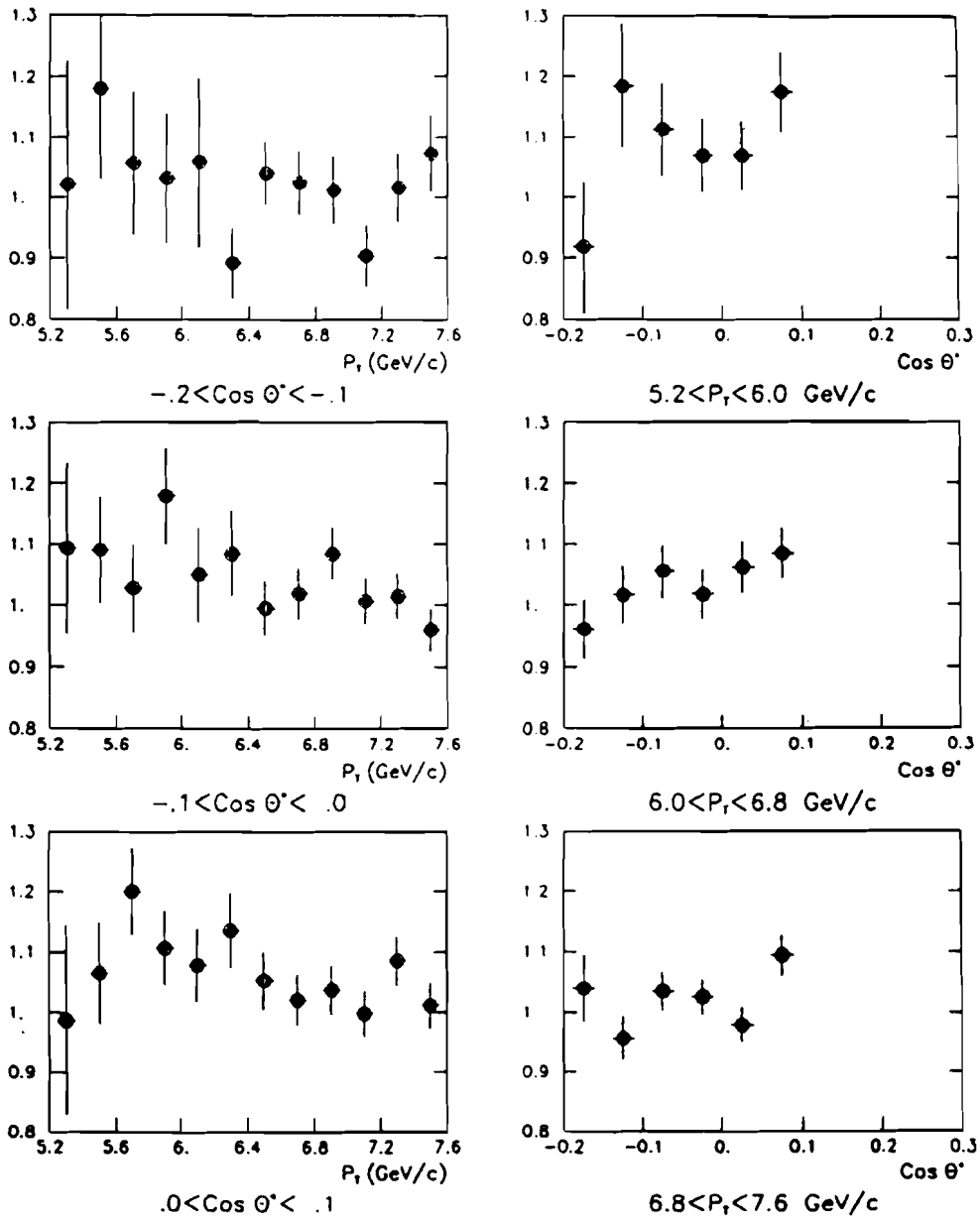

Figure 30

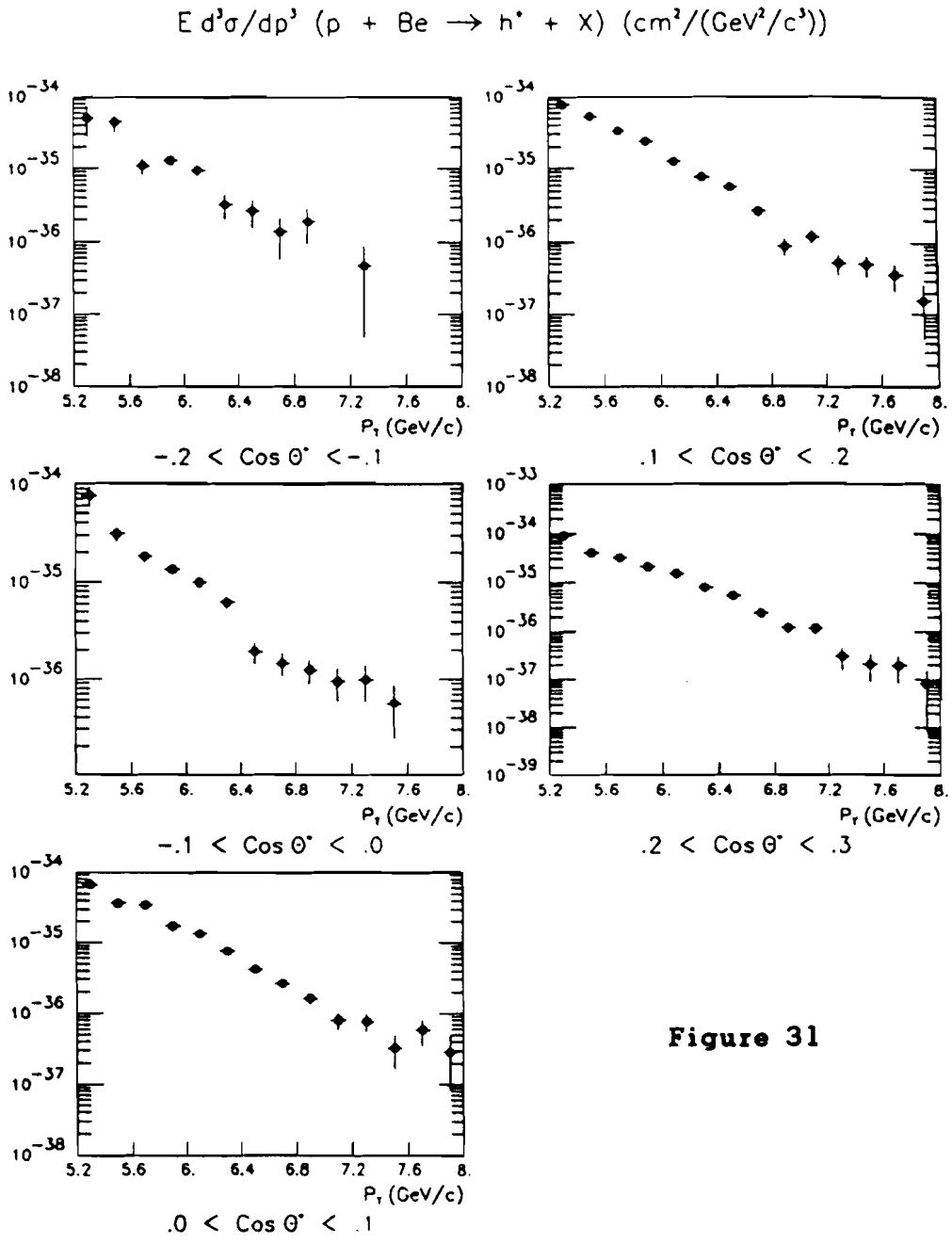
E d³σ/dp³ (p + Be → h⁺ + X) (cm²/(GeV²/c³))
P_T (GeV/c)
−.2 < Cos Θ* < −.1
.1 < Cos Θ* < .2
−.1 < Cos Θ* < .0
.2 < Cos Θ* < .3
.0 < Cos Θ* < .1

Figure 31

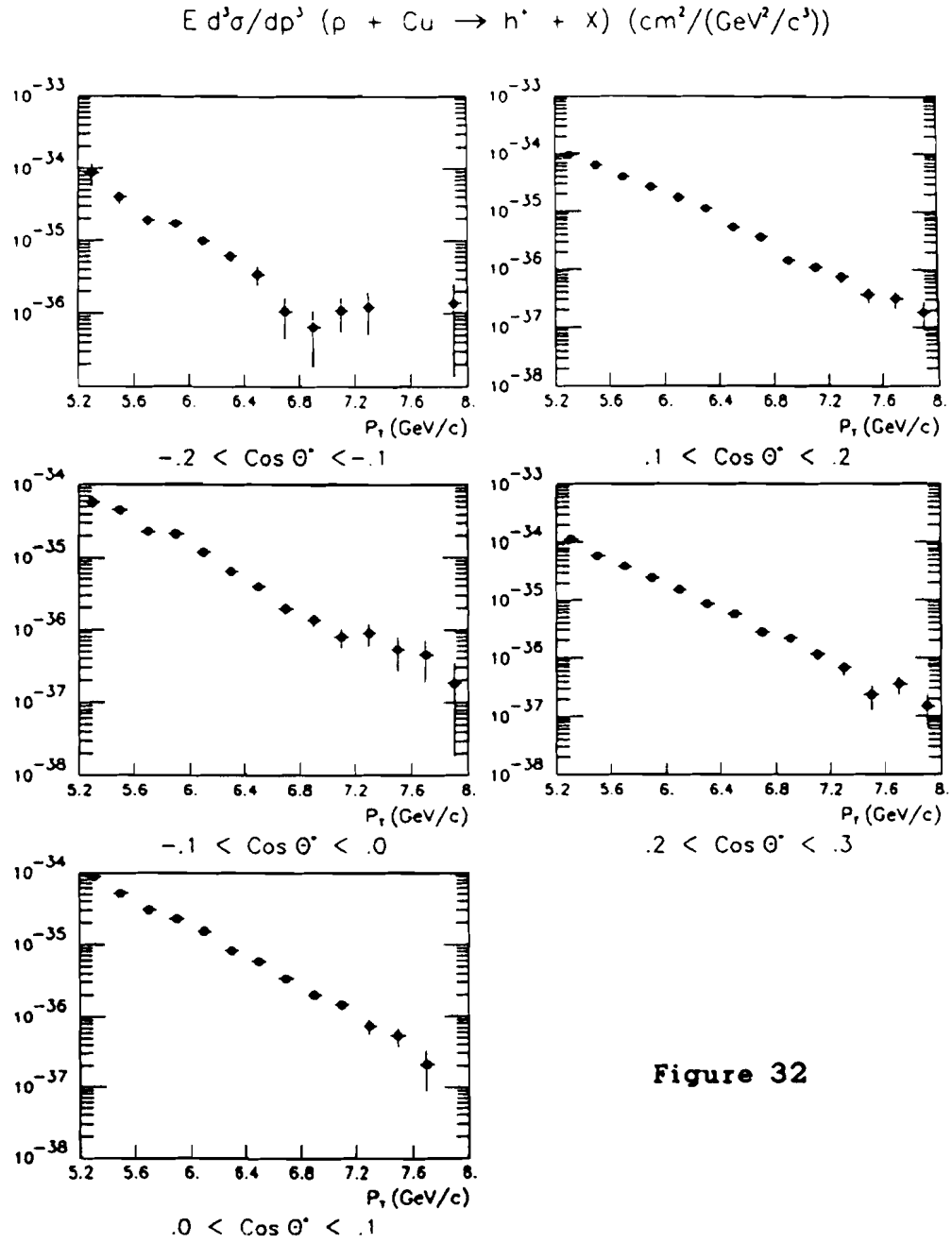
E d³σ/dp³ (p + Cu → h⁺ + X) (cm²/(GeV²/c³))
P_T (GeV/c)
−.2 < Cos Θ* < −.1
.1 < Cos Θ* < .2
−.1 < Cos Θ* < .0
.2 < Cos Θ* < .3
.0 < Cos Θ* < .1

Figure 32

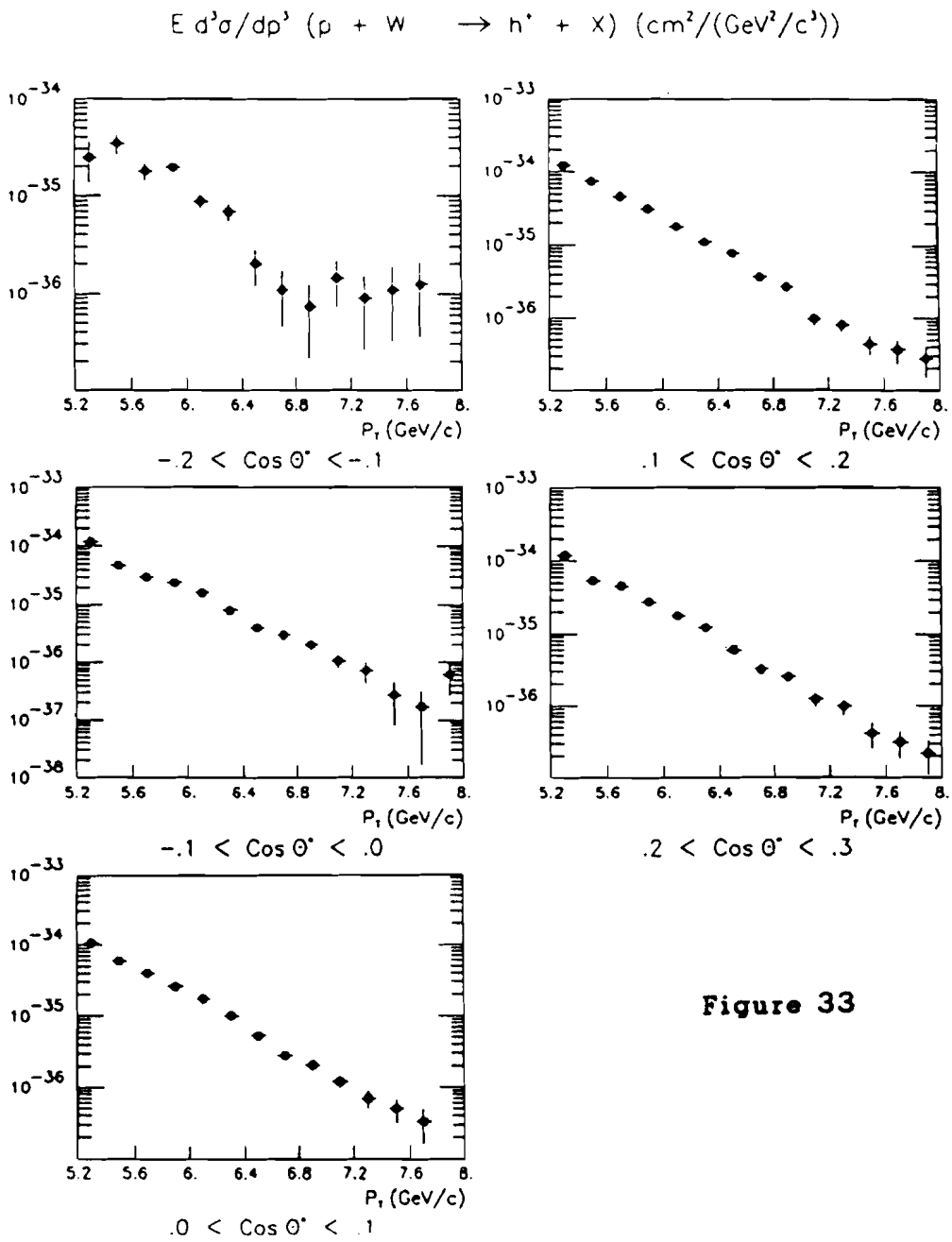
E d³σ/dp³ (p + W → h⁺ + X) (cm²/(GeV²/c³))
P_T (GeV/c)
-.2 < Cos Θ* < -.1
.1 < Cos Θ* < .2
-.1 < Cos Θ* < .0
.2 < Cos Θ* < .3
.0 < Cos Θ* < .1

Figure 33

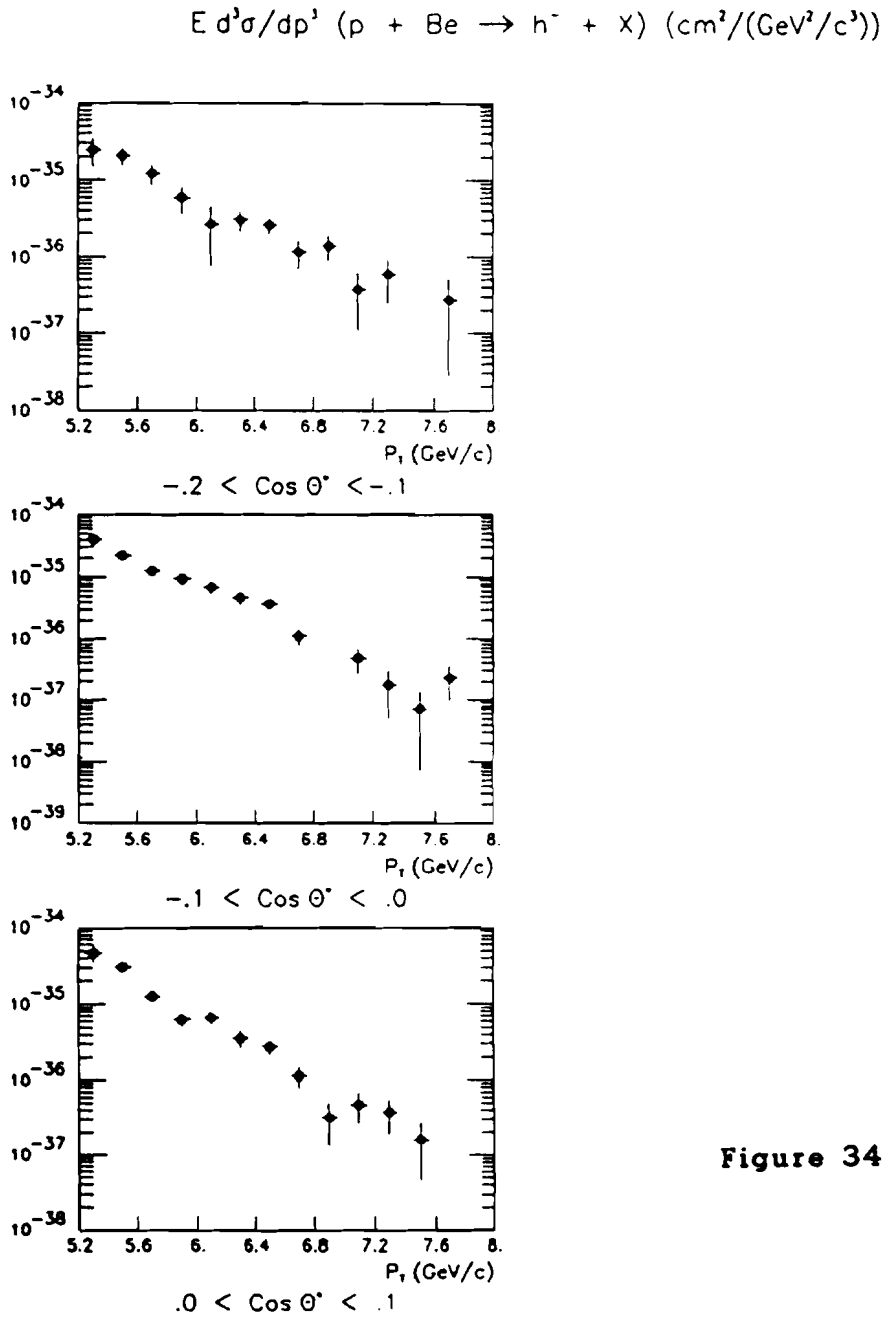
E d³σ/dp³ (p + Be → h⁻ + X) (cm²/(GeV²/c³))
10⁻³⁴
10⁻³⁵
10⁻³⁶
10⁻³⁷
10⁻³⁸
5.2 5.6 6. 6.4 6.8 7.2 7.6 8
P_T (GeV/c)
−.2 < Cos Θ* < −.1
10⁻³⁹
−.1 < Cos Θ* < .0
.0 < Cos Θ* < .1

Figure 34

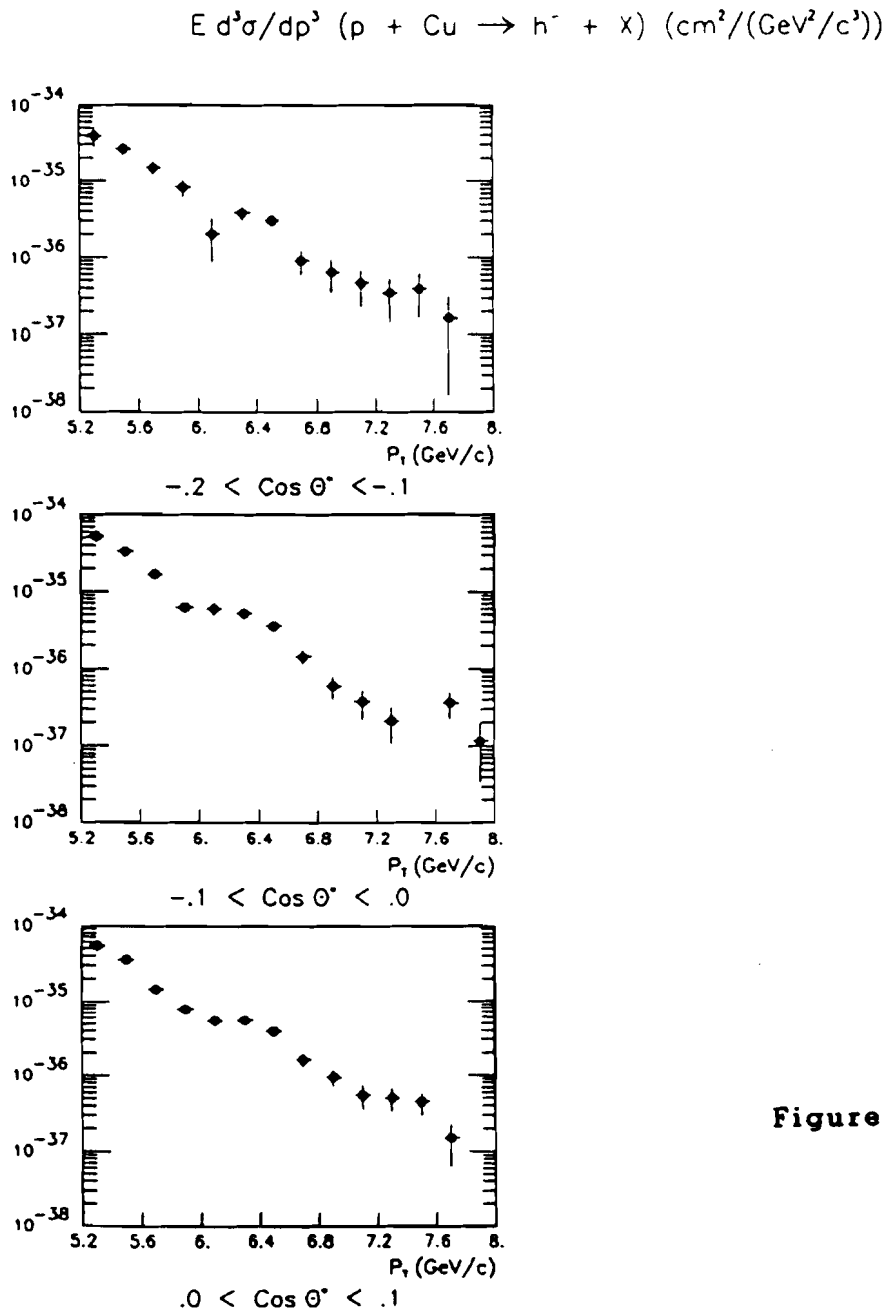
E d³σ/dp³ (p + Cu → h⁻ + X) (cm²/(GeV²/c³))
10⁻³⁴
10⁻³⁵
10⁻³⁶
10⁻³⁷
10⁻³⁸
5.2 5.6 6. 6.4 6.8 7.2 7.6 8.
P_T (GeV/c)
−.2 < Cos Θ* <−.1
−.1 < Cos Θ* < .0
.0 < Cos Θ* < .1

Figure 35

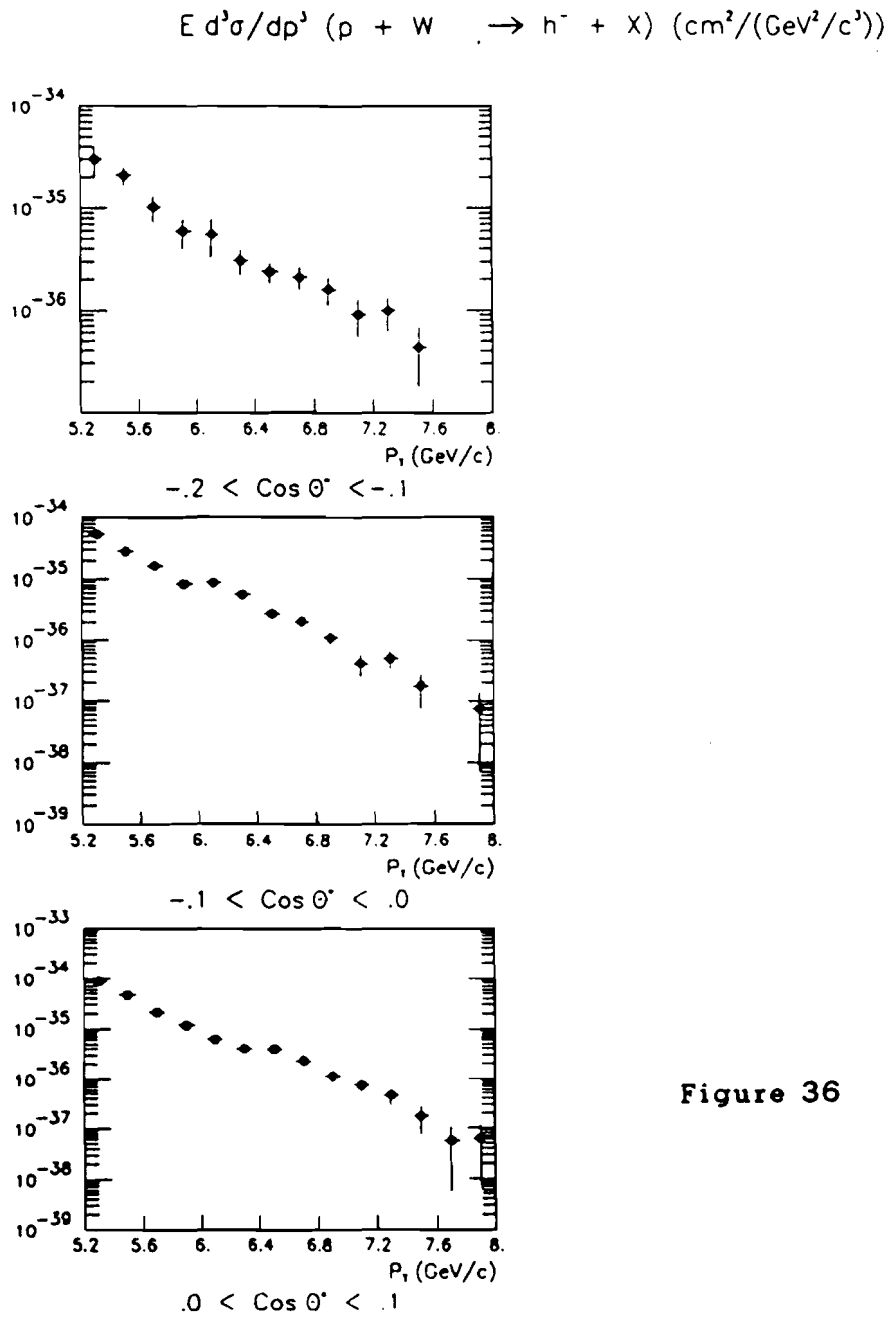
E d³σ/dp³ (p + W → h⁻ + X) (cm²/(GeV²/c³))
10⁻³⁴
10⁻³⁵
10⁻³⁶
5.2 5.6 6. 6.4 6.8 7.2 7.6 8.
P_T (GeV/c)
−.2 < Cos Θ* < −.1
10⁻³⁴
10⁻³⁵
10⁻³⁶
10⁻³⁷
10⁻³⁸
10⁻³⁹
5.2 5.6 6. 6.4 6.8 7.2 7.6 8.
P_T (GeV/c)
−.1 < Cos Θ* < .0
10⁻³³
10⁻³⁴
10⁻³⁵
10⁻³⁶
10⁻³⁷
10⁻³⁸
10⁻³⁹
5.2 5.6 6. 6.4 6.8 7.2 7.6 8.
P_T (GeV/c)
.0 < Cos Θ* < .1

Figure 36

The Atomic Weight Dependence Parameter α for Positive Hadrons

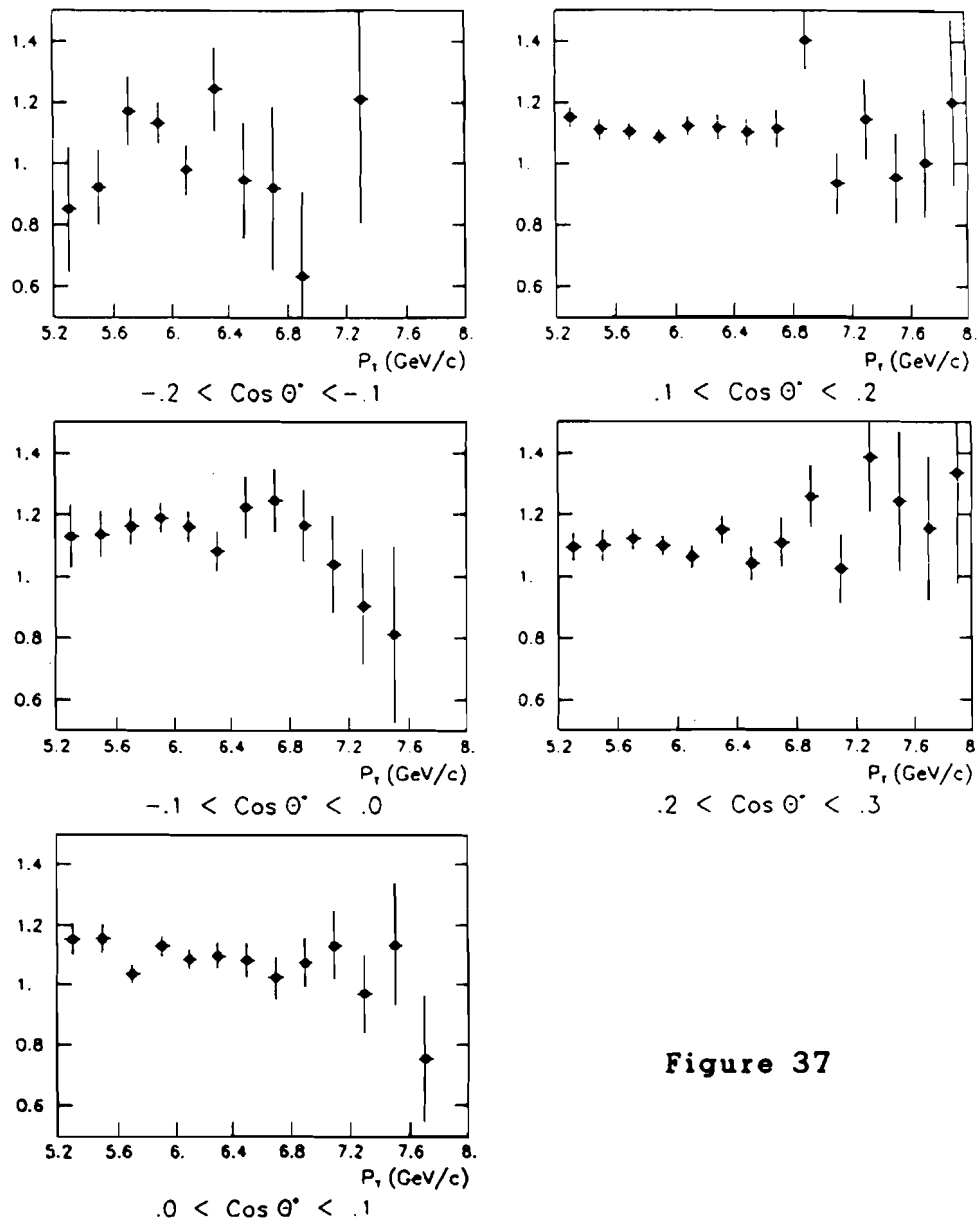

Figure 37

Atomic Weight Dependence for Negative Hadrons

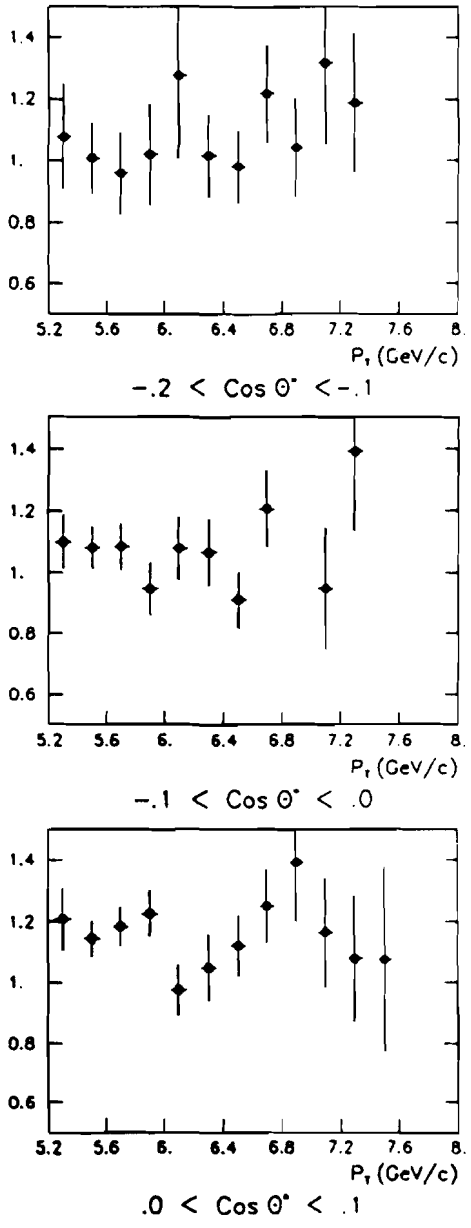

Figure 38

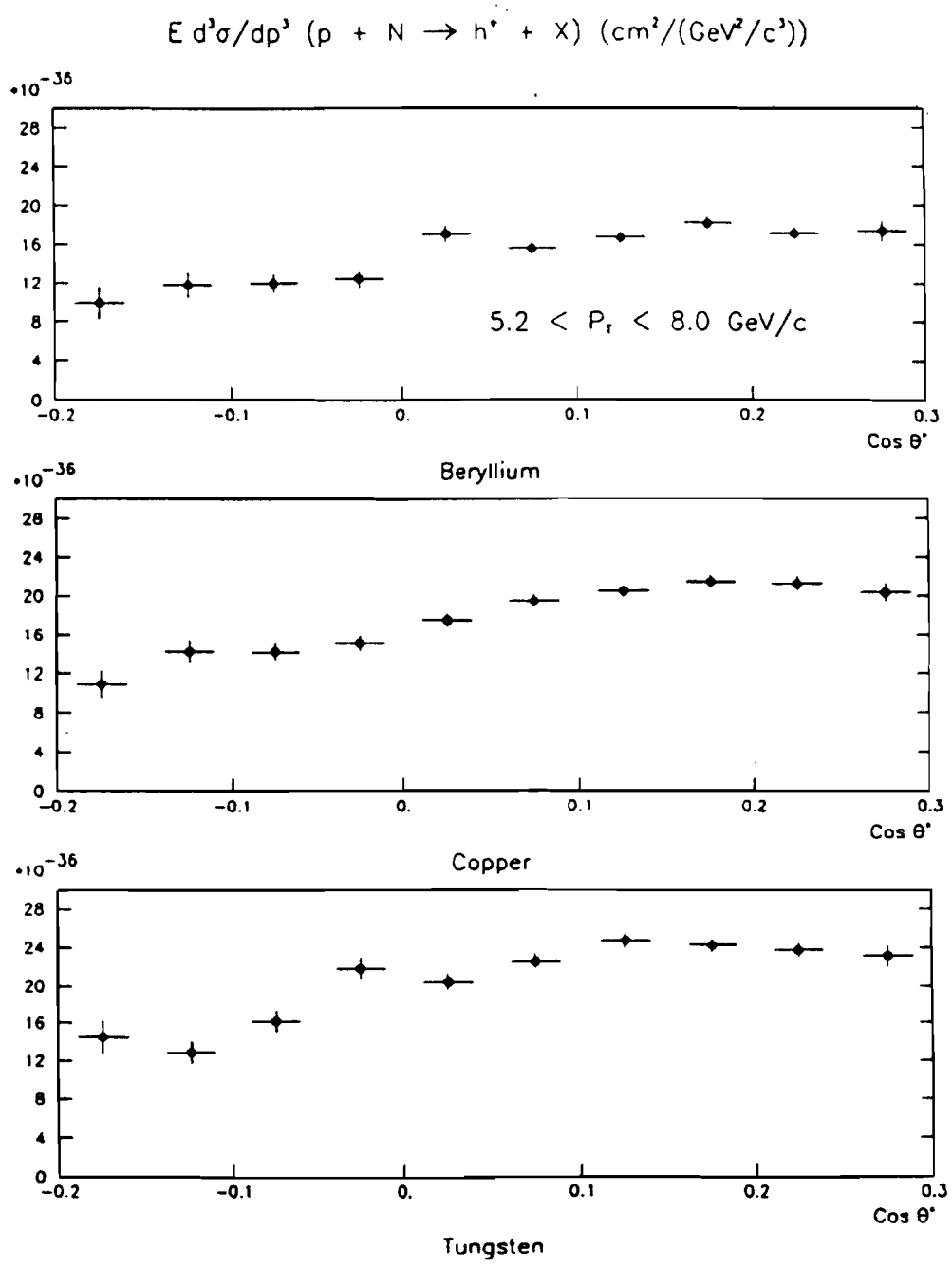
E d³σ/dp³ (p + N → h⁺ + X) (cm²/(GeV²/c³))
•10⁻³⁶
5.2 < P_T < 8.0 GeV/c
Cos θ*
Beryllium
Copper
Tungsten

Figure 39

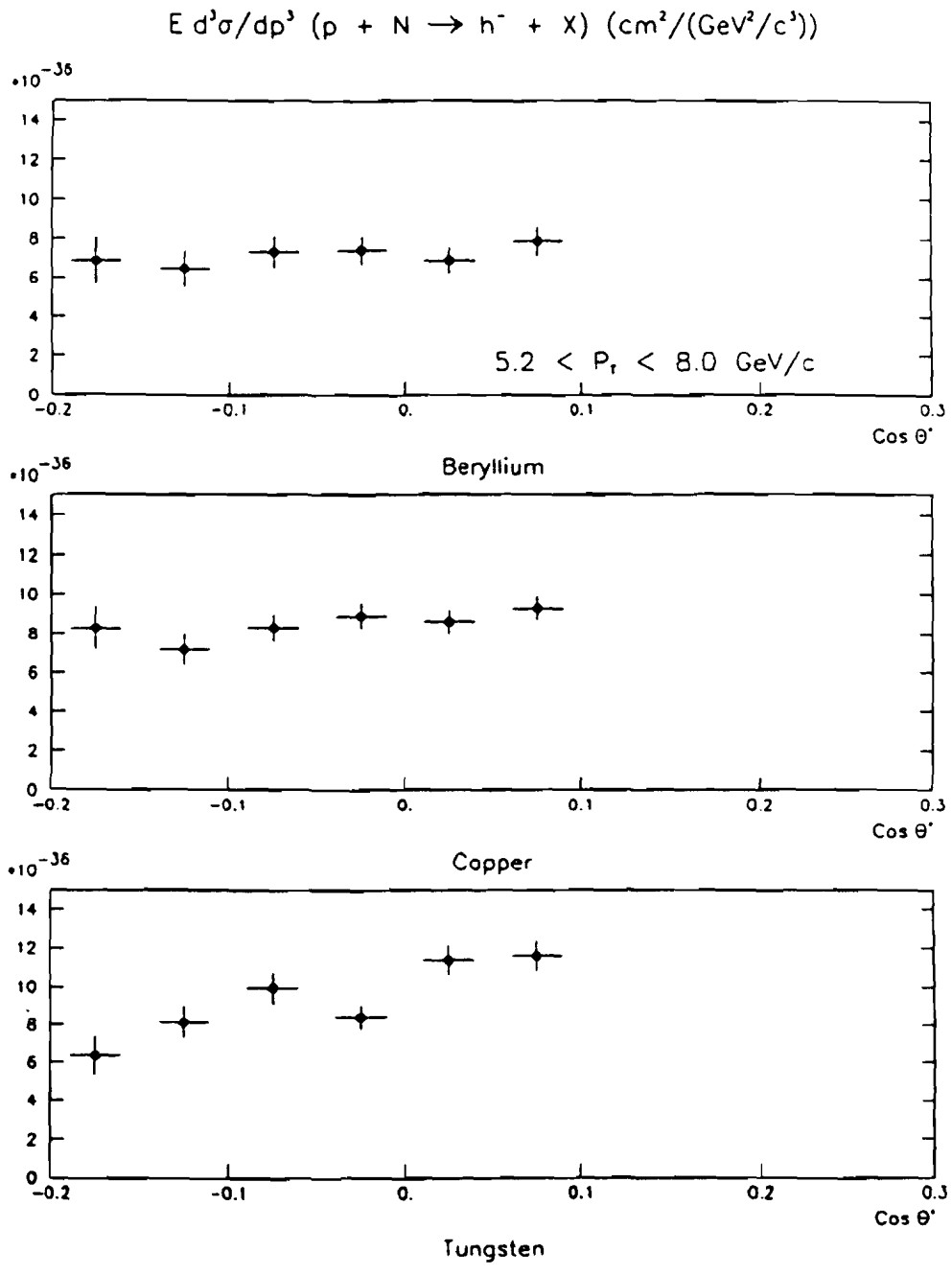
E d³σ/dp³ (p + N → h⁻ + X) (cm²/(GeV²/c³))
•10⁻³⁶
5.2 < P_T < 8.0 GeV/c
Cos θ*
Beryllium
Copper
Tungsten

Figure 40

The Atomic Weight Dependence Parameter α versus Angle

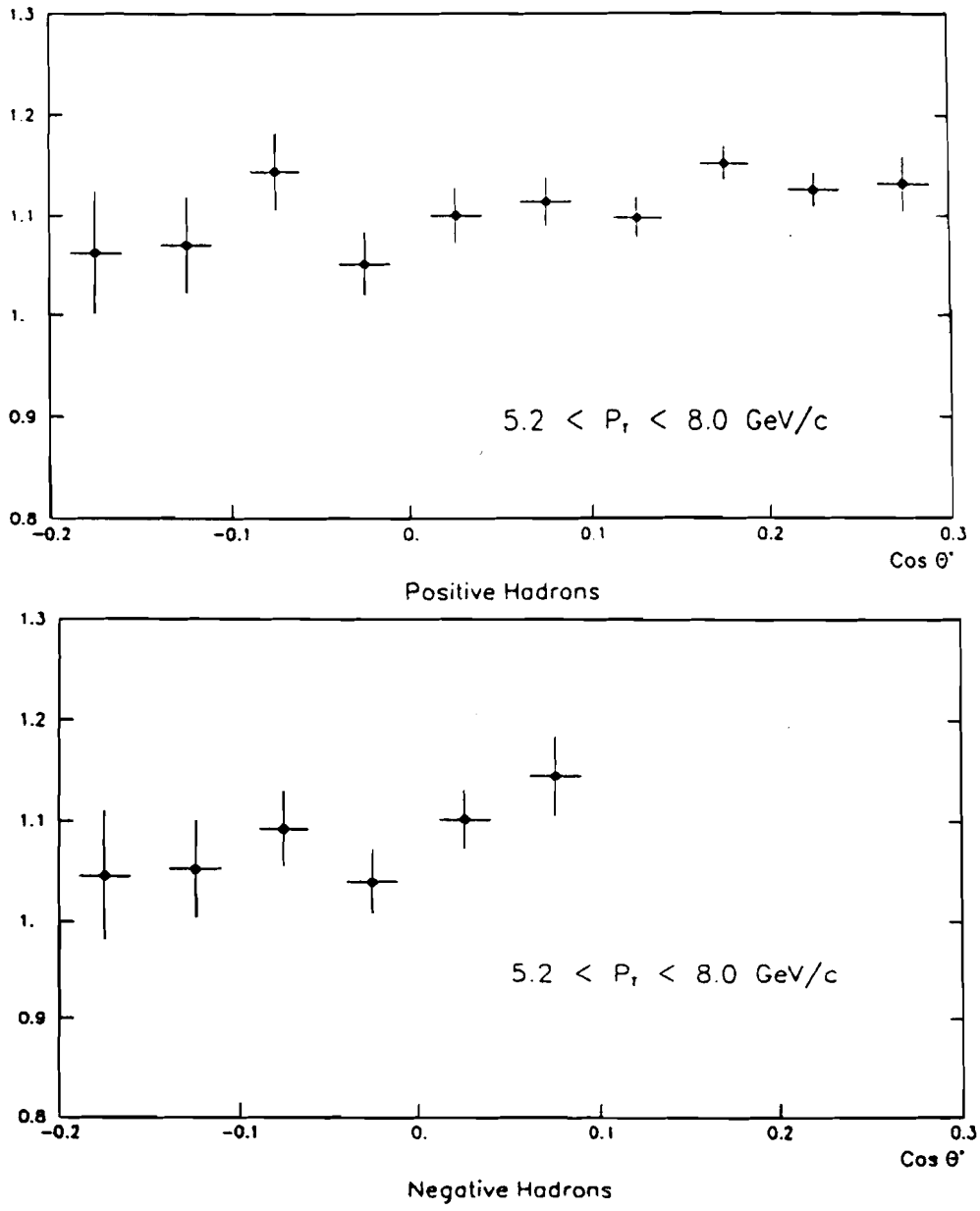

Figure 41

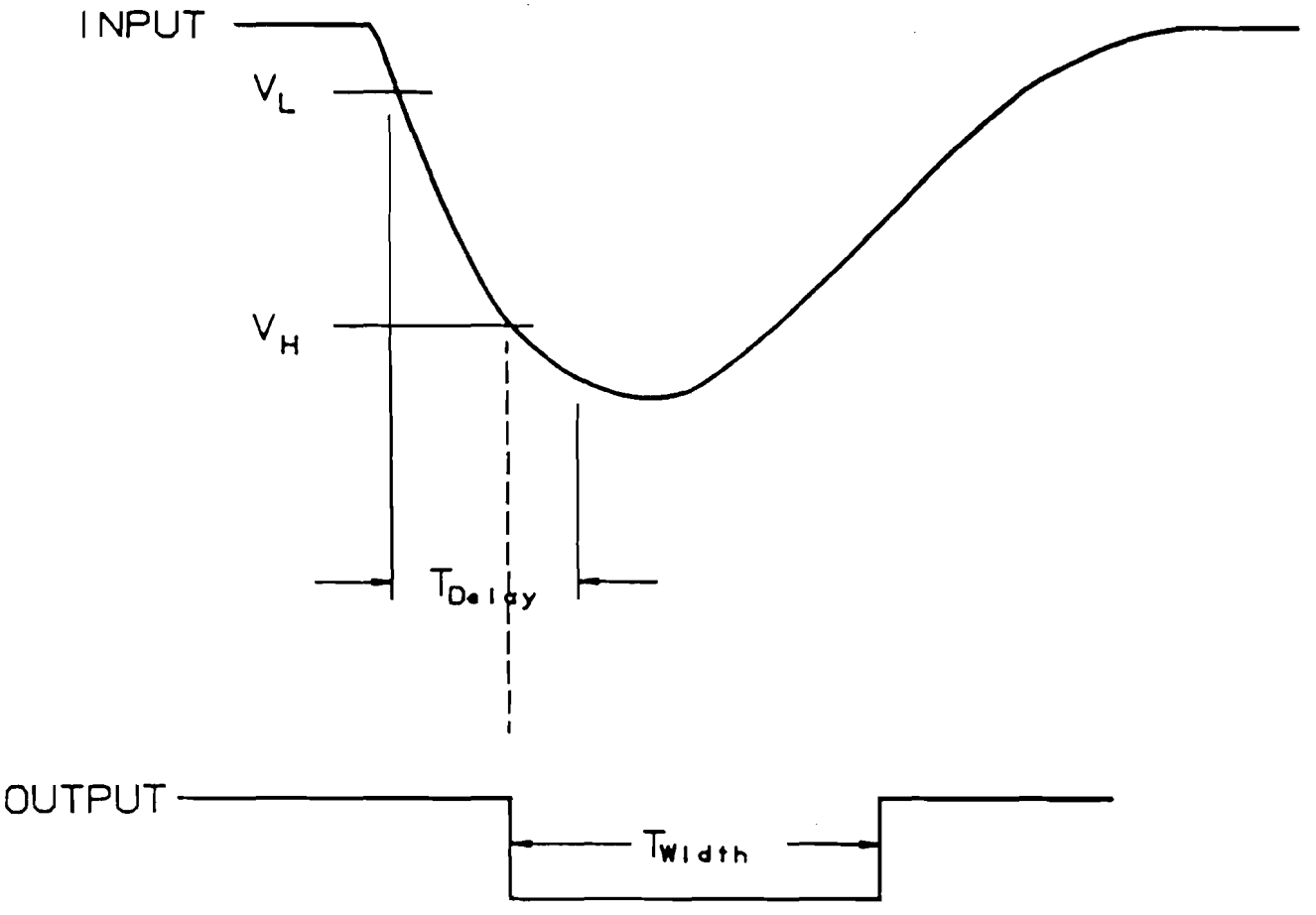

Figure 42

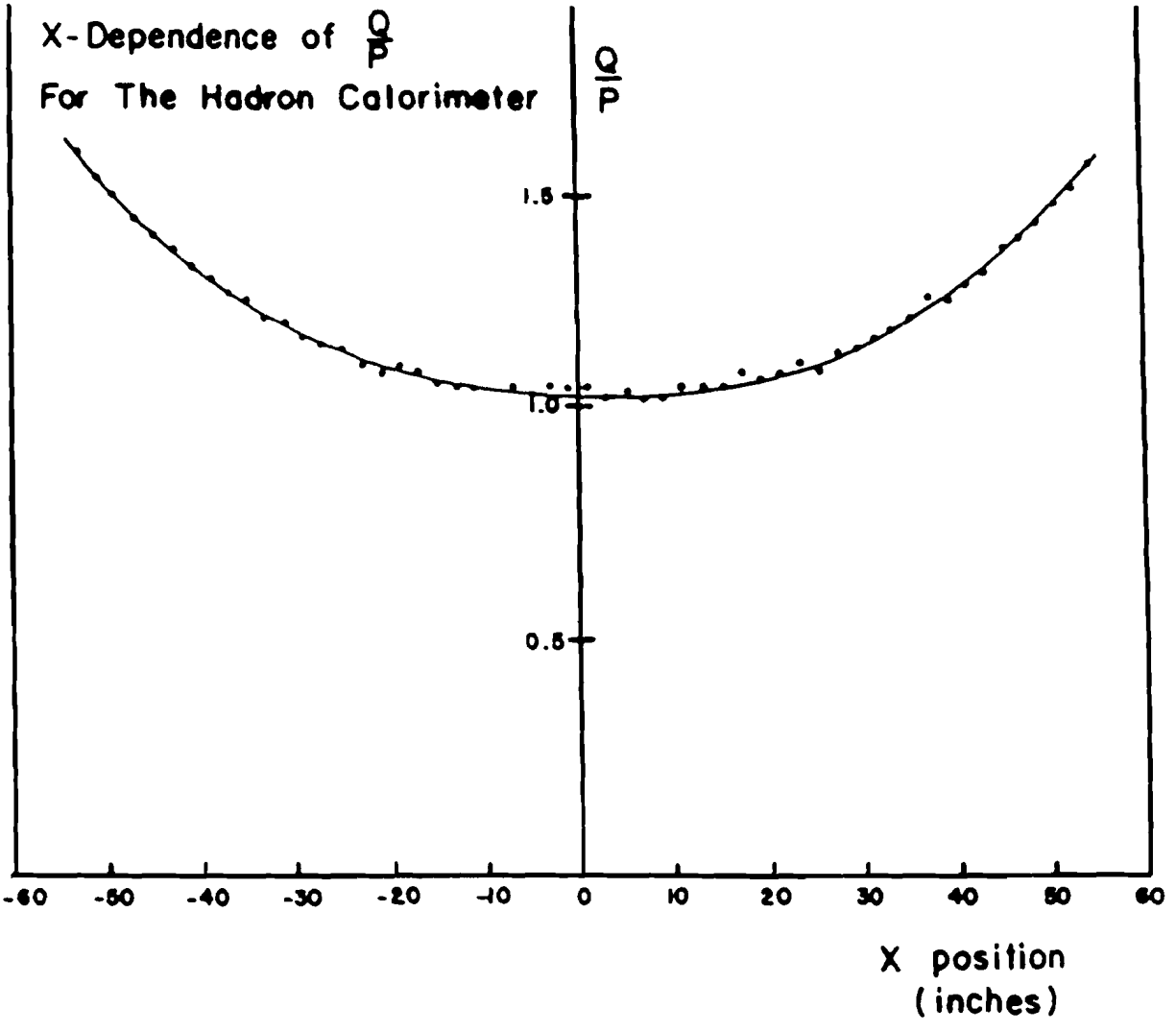
X-Dependence of Q/P
For The Hadron Calorimeter
Q/P
1.5
1.0
0.5
-60
-50
-40
-30
-20
-10
0
10
20
30
40
50
60
X position
(inches)

Figure 43

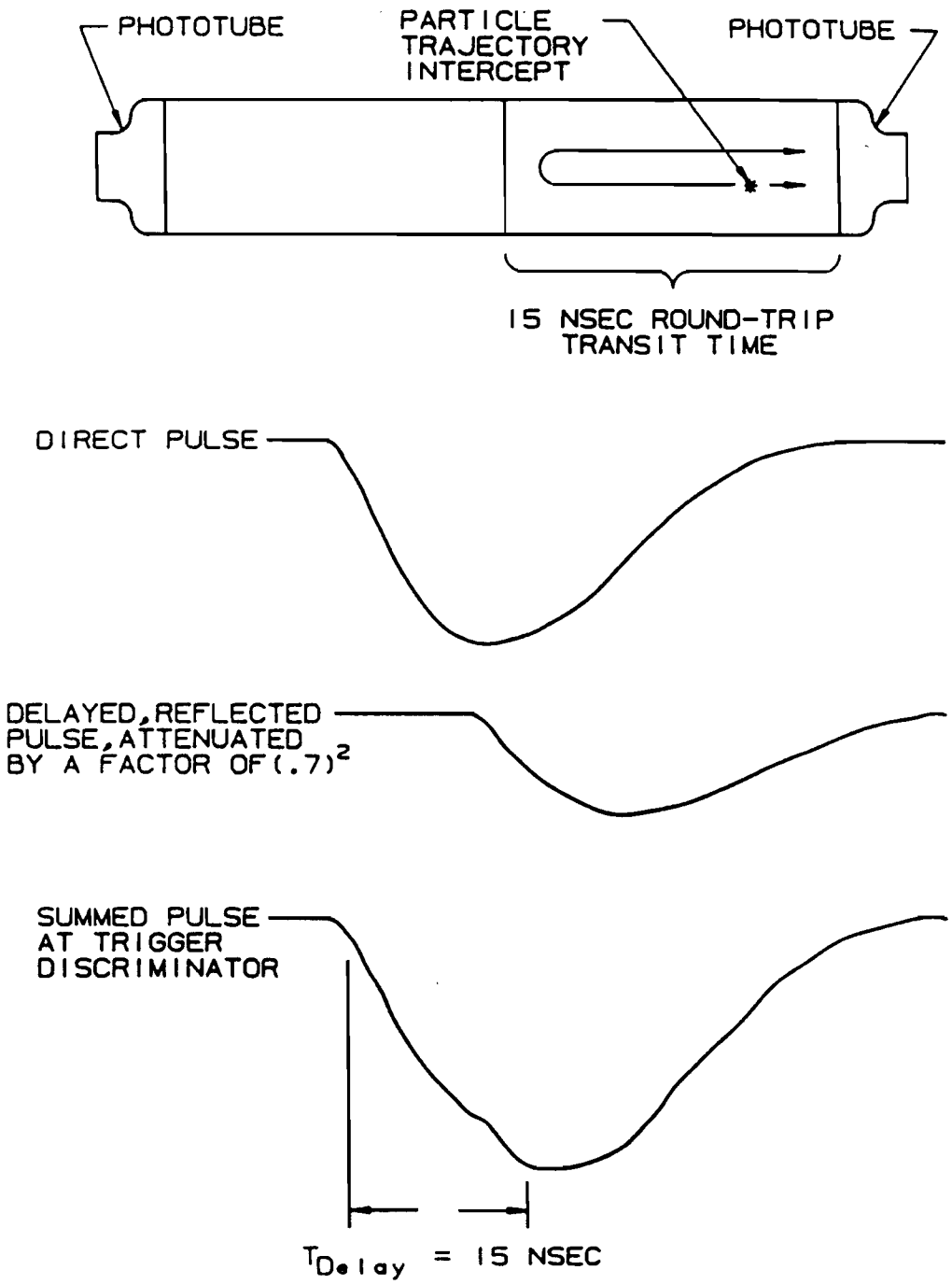
PHOTOTUBE
PARTICLE TRAJECTORY INTERCEPT
PHOTOTUBE
15 NSEC ROUND-TRIP TRANSIT TIME
DIRECT PULSE
DELAYED, REFLECTED PULSE, ATTENUATED BY A FACTOR OF (.7)²
SUMMED PULSE AT TRIGGER DISCRIMINATOR
T Delay = 15 NSEC

Figure 44

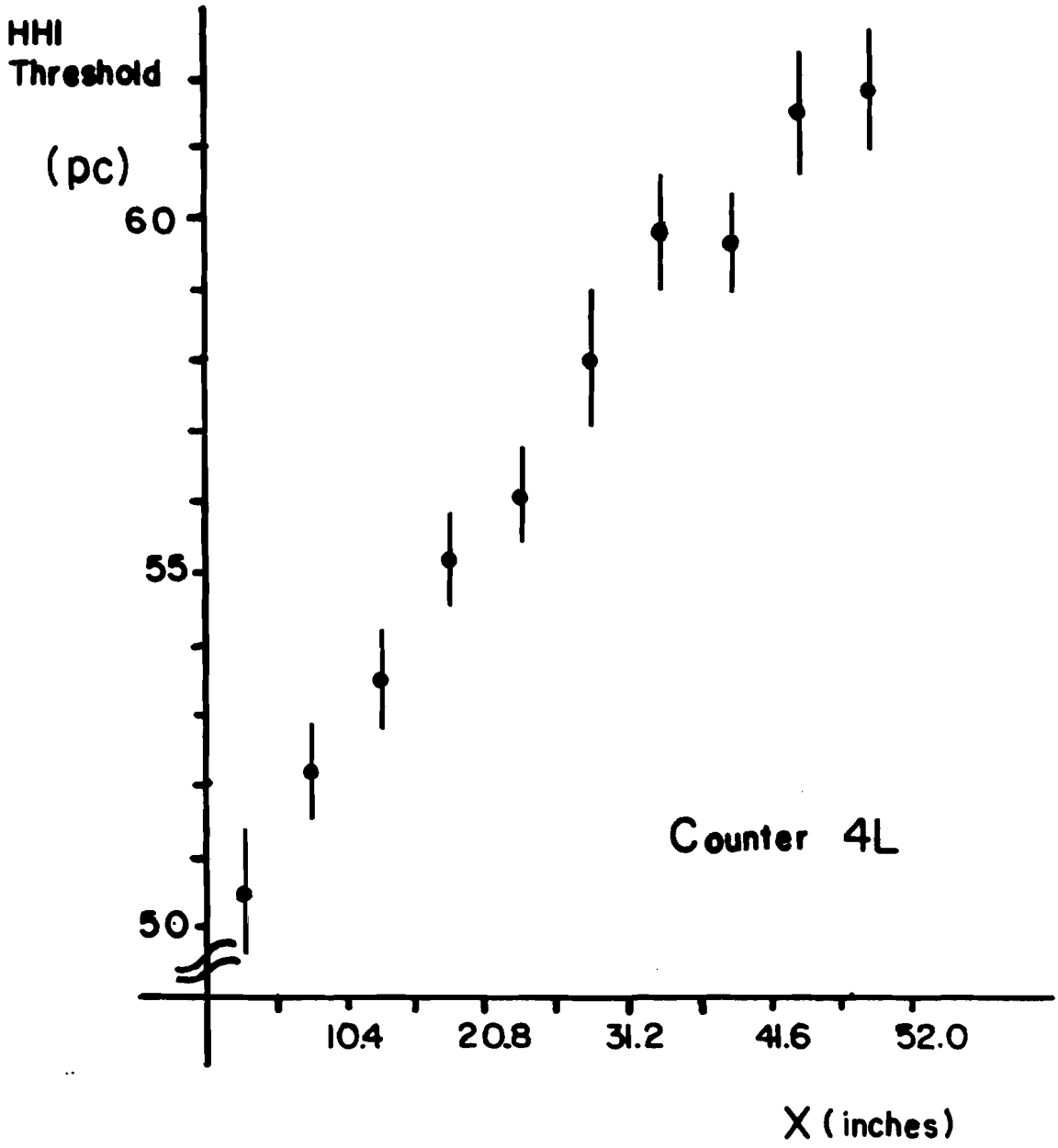
HHI
Threshold
(pc)
60
55
50
Counter 4L
10.4
20.8
31.2
41.6
52.0
X (inches)

Figure 45

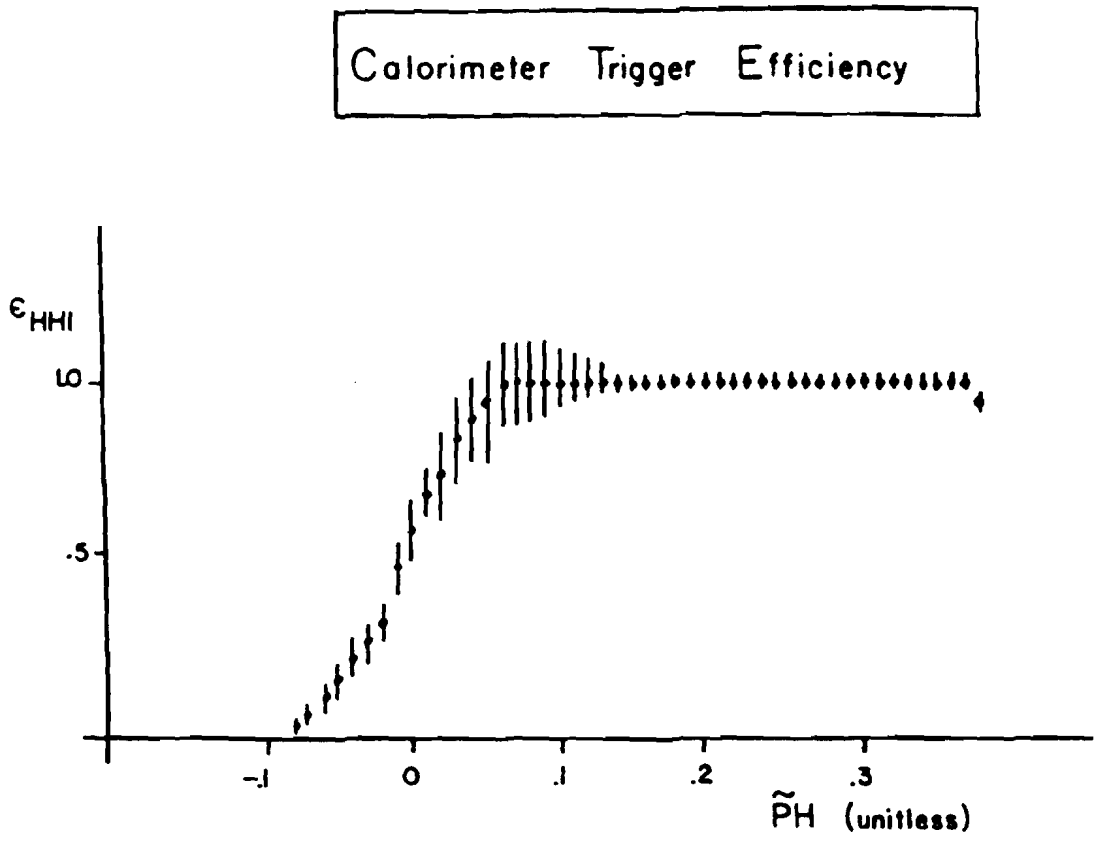

$$\epsilon_{HHI} = \mathrm{erf}\ (\widetilde{PH}, 4\%)$$

Where $\widetilde{PH} = \sum_{i=1}^{N} \frac{Q_i}{K_i(x)} - 1$

and $K_i\ (x) = K_i^{\circ} + \alpha x$

Figure 46